Maria Principe

Noise Modeling and Reduction in Gravitational Wave Detection Experiments

Department of Engineering

University of Sannio, Benevento

July 2010

©Maria Principe

To my Spouse

Sommario

Questa tesi affronta, seguendo un approccio ingegneristico, due problemi di fondamentale importanza nell'ambito dell'esperimento LIGO-Virgo per la rivelazione di onde gravitazionali attraverso antenne interferometriche a grande base. I problemi affrontati riguardano le due principali sorgenti di rumore, che limitano attualmente la sensibilitá degli interferometri ai segnali gravitazionali.

La prima sorgente di rumore considerata fa riferimento alla presenza nei dati di uscita di frequenti segnali transitori spuri, *glitch*, di origine ambientale o strumentale. I glitch riducono enormemente l'efficienza di rivelazione, specialmente nella ricerca di onde gravitazionali impulsive non modellate, *burst*. Al fine di affrontare il problema dei glitch mediante gli strumenti della teoria classica della rivelazione e della stima, ho sviluppato un modello analitico per il rumore in uscita agli interferometri, e, in accordo a tale modello, ho progettato due strategie (localmente) ottime, insieme alle corrispondenti versioni robuste rispetto a incertezze e/o fluttuazioni delle caratteristiche del rumore, per la rivelazione di *bursts* gravitazionali non modellati mediante i tre interferometri che costituiscono l'osservatorio LIGO-Virgo. Tali strategie sono state testate sia in rumore simulato che nel rumore effettivamente presente nel canale dati degli interferometri LIGO, risultando migliori in prestazioni rispetto a quelle basate sull'ipotesi di rumore Gaussiano, che adottano procedure euristiche ad hoc (data quality flagging) per individuare ed eventualmente escludere (vetoing) i dati corrotti da glitch.

La seconda sorgente di rumore considerata ha origine nel *coating* dielettrico delle masse di prova dei due bracci degli interferometri. Il rumore termico del coating é la componente di rumore dominante nella banda di maggiore sensibilitá delle antenne interferometriche. Utilizzando gli strumenti classici per lo studio di scattering elettromagnetico da strutture planari stratificate, ho formulato una procedura di ottimizzazione per progettare *coating* a minimo rumore termico, che soddisfino le specifiche di riflettivitá a una (disegno *monocroico*) o due (disegno *dicroico*) lunghezze d'onda. Utilizzando tale procedura, ho in particolare progettato due prototipi di *coating*: il primo prototipo, *monocroico*, é stato realizzato dai Laboratoires des Materiaux Avances del CNRS (Lyon, FR), ed il relativo rumore termico é stato misurato nei laboratori LIGO del California Institute of Technology (Pasadena, USA). I risultati ottenuti sono in eccellente accordo con i valori teorici attesi; il secondo prototipo, *dicroico*, é stato ugualmente realizzato e le misure sperimentali sono in corso.

Parole chiave: rivelazione interferometrica di onde gravitazionali, rumore impulsivo, rivelazione in rete di sensori, rumore termico, coating dielettrici ottimizzati.

Resume

This thesis develops an engineering approach to two problems relevant to the LIGO-Virgo experiment for the detection of gravitational waves using large baseline optical interferometers. These problems are related to the two dominant noise sources, which limit the instruments' sensitivity, and whose modeling and reduction is the target of this study.

The first considered noise source is related to the presence at the output channel of frequent spurious transient signals, the *glitches*, of environmental or instrumental origin. Glitches seriously spoil the detection efficiency, especially in the search of unmodeled *bursts* of gravitational radiation. To attack this problem in the frame of classical theory of detection and estimation, I developed an analytical model for the interferometer noise, and designed two (locally) optimum strategies, together with their robust implementations which are tolerant against incomplete knowledge and/or fluctuations of the noise features, for the detection of gravitational wave *bursts* in the presence of glitches, using the LIGO-Virgo network of three interferometers. These strategies have been tested both in simulated and in real LIGO noise, and featured better performance compared to those based on the Gaussian noise assumption, currently adopted in the LIGO-Virgo data analysis pipelines, which rely on additional heuristic ad hoc procedures of data quality flagging and/or vetoing.

The second considered noise source arises in the reflective dielectric coatings laid on top of the test masses, placed at the two ends of both interferometers' arms. Coating thermal noise is the dominant noise component in the most sensitive frequency band of interferometric antennas. Capitalizing on the canonical approach to the study of the EM wave scattering from plane layered media, I formulated an optimization strategy to design coatings, featuring a minimum amount of thermal noise, while exhibiting the required reflectivity level, for the case of single (*monochroic* design) and double (*dichroic* design) wavelength operation. Using the formulated strategy, I designed two coating prototypes: the first monochroic design was manifactured by the CNRS Laboratoires des Materiaux Avances (Lyon, FR), a member of the LIGO-Virgo cooperation, and its thermal noise was measured at California Instuitute of Technology (Pasadena, USA), yielding results in excellent agreement with theoretical predicitions; a second dichroic design was also prototyped, and is currently under test at

Caltech.

Keywords: interferometric gravitational wave detectors, impulsive noise, multiple-sensor detection, thermal noise, dielectric coatings optimization.

List of publications

Pubblications of Maria Principe during her PhD years

[1] Villar A, Principe M, et al. (2010) “Measurements of Thermal Noise in Multilayer Coatings with Optimized Layer Thickness”, *Phys Rev D*, 81:122001.

[2] Principe M and Pinto IM (2010) “Locally Optimum Network Detection of Unmodeled GW Bursts in Glitch Noise”, *Phys Rev D*, under review.

[3] Principe M and Pinto IM (2009) “Detecting Unmodeled GW Bursts in non-Gaussian (Glitchy) Noise: two Locally Optimum Network Detectors”, *Class Quantum Grav*, 26:204001.

[4] Principe M and Pinto IM (2009) “Locally Optimum Network Detection of Unmodeled Gravitational Wave Bursts in an Impulsive Noise Background”, *Class Quantum Grav*, 26:045003.

[5] Principe M and Pinto IM (2008) “Modeling the Impulsive Noise Component and its Effect on the Operation of a Simple Coherent Network Algorithm for Unmodeled Gravitational Wave Burst Detection”, *Class Quantum Grav*, 25:075013.

[6] Principe M and the LSC (2010) “First Search for Gravitational Waves from the Youngest Known Neutron Star”, *sumbitted for pubblication.*

[7] Principe M and the LSC (2010) “Search for Gravitational Waves from Compact Binary Coalescence in LIGO and Virgo Data from S5 and VSR1”, *sumbitted for pubblication.*

[8] Principe M and the LSC (2010) “Predictions for the Rates of Compact Binary Coalescences Observable by Ground-based Gravitational-wave Detectors”, *Class Quantum Grav*, 27:173001.

[9] Principe M and the LSC (2010) “Search for gravitational-wave inspiral signals associated with short Gamma-Ray Bursts during LIGO’s fifth and Virgo’s first science run”, *Astrophys J*, 715:1453.

[10] Principe M and the LSC (2010) “All-sky search for gravitational-wave bursts in the first joint LIGO-GEO-Virgo run”, *Phys Rev D*, 81:102001.

[11] Principe M and the LSC (2010) “Search for gravitational-wave bursts associated with gamma-ray bursts using data from LIGO Science Run 5 and Virgo Science Run 1”, *Astrophys J*, 715:138.

[12] Principe M and the LSC (2010) “Searches for gravitational waves from known pulsars with S5 LIGO data”, *Astrophys J*, 713:671.

[13] Principe M and the LSC (2010) “An upper limit on the stochastic gravitational-wave background of cosmological origin”, *Nature*, 460:990.

[14] Principe M and the LSC (2009) “Search for gravitational wave ringdowns from perturbed black holes in LIGO S4 data”, *Phys Rev D*, 80:062001.

[15] Principe M and the LSC (2009) “Search for High Frequency Gravitational Wave Bursts in the First Calendar Year of LIGO’s Fifth Science Run”, *Phys Rev D*, 80:102002.

[16] Principe M and the LSC (2009) “Stacked Search for Gravitational Waves from the 2006 SGR 1900+14 Storm”, *Astrophys J*, 701:L68.

[17] Principe M and the LSC (2009) “Search for gravitational-wave bursts in the first year of the fifth LIGO science run”, *Phys Rev D*, 80:102001.

[18] Principe M and the LSC (2009) “Einstein@Home search for periodic gravitational waves in early S5 LIGO data”, *Phys Rev D*, 80:042003.

[19] Principe M and the LSC (2009) “Search for Gravitational Waves from Low Mass Compact Binary Coalescence in 186 Days of LIGO’s fifth Science Run”, *Phys Rev D*, 80:047101.

[20] Principe M and the LSC (2009) “First LIGO search for gravitational wave bursts from cosmic (super)strings”, *Phys Rev D*, 80:062002.

[21] Principe M and the LSC (2009) “Search for Gravitational Waves from Low Mass Binary Coalescences in the First Year of LIGO’s S5 Data”, *Phys Rev D*, 79:122001.

[22] Principe M and the LSC (2009) "All-sky LIGO Search for Periodic Gravitational Waves in the Early S5 Data", *Phys Rev Lett*, 102:111102.

[23] Principe M and the LSC (2009) "The Einstein@Home search for periodic gravitational waves in LIGO S4 data", *Phys Rev D*, 79:022001.

[24] Principe M and the LSC (2009) "LIGO: The Laser Interferometer Gravitational-Wave Observatory", *Rep Progr Phys*, 72:076901.

[25] Principe M and the LSC (2008) "Search for Gravitational Wave Bursts from Soft Gamma Repeaters", *Phys Rev Lett*, 101:211102

[26] Principe M and the LSC (2008) "First joint search for gravitational-wave bursts in LIGO and GEO600 data", *Class Quantum Grav*, 25:245008.

[27] Principe M and the LSC (2008) "Beating the spin-down limit on gravitational wave emission from the Crab pulsar", *Astrophys J*, 683:45.

[28] Principe M, Galdi V, Pierro V and Pinto IM (2008) "Minimum Brownian Noise Dichroic Dielectric Mirror Coatings for AdLIGO", *LIGO Technical Report*, LIGO-T080336-00-D.

[29] Principe M e Pinto IM (2008) "Locally Optimum Network Detection of Unmodeled Gravitational Wave Burst in an Impulsive Noise Background", *LIGO Technical Report*, LIGO-P080066-00-Z.

[30] Principe M and Pinto IM (2007) "Glitch Rejection Properties of a Simple Network Algorithm for Detecting Unmodeled Gravitational Wave Bursts", *LIGO Technical Report*, LIGO-P070143-00-Z.

[31] Pinto IM, Galdi V and Principe M (2007) "A general Formula for Thermorefractive Noise Coefficient of Stacked-Doublet Mirror Coatings", *LIGO Technical Report*, LIGO-T070159-00-Z.

[32] Principe M et al. (2007) "Coherent Methods for Detecting GW Bursts in a Worldwide Network", *Legnaro National Laboratory Annual Report*, Jan 2007.

[33] Principe M (2005) "Modeling the performance of the Network of Gravitational Wave Detectors", *LIGO Technical Report*, T050224-00-R.

Presentations at national and international conferences

[34] Principe M et al. “Thermorefractive Noise In Stacked Doublet Dielectric Mirror Coatings”, to be presented at XVIII Riunione Nazionale di Elettromagnetismo, Benevento (Italy) September 2010.

[35] Principe M et al. “Minimum Noise Dichroic Mirror Coatings For AdvLIGO”, to be presented at XVIII Riunione Nazionale di Elettromagnetismo, Benevento (Italy) September 2010.

[36] Principe M et al “Direct Measurement Of Brownian Noise In Prototype Optimized Mirror Coatings For Ligo”, to be presented at XVIII Riunione Nazionale di Elettromagnetismo, Benevento (Italy) September 2010.

[37] Pinto IM, Pierro V, Principe M, DeSalvo R “Mixture Theory Approach for Coating Materials Optimizatio”, GWADW, 16-21 May 2010, Kyoto, Japan.

[38] Pierro V, Principe M, Rampone S, Troiano L, Pinto IM, “A Neural Net for Glitch-Burst Discrimination and Glitch Classification”, 14-GWDAW, 26-29 January 2010, Roma, Italy.

[39] Croce RP, Pierro V, Postiglione F, Principe M, Pinto IM, “One More Technique for Burst Source Position Identification: X-Wigner Spectr”, 14-GWDAW, 26-29 January 2010, Roma, Italy.

[40] Altheimer A, Principe M et al. “Atomic Representation of Glitches - Preliminary Results”, *LIGO Technical Report* LIGO-G0900045, 13-GWDAW, San Juan (USA), January 2009.

[41] Principe M and Pinto IM “A Whole Network Detection Statistic for Unmodeled GW Bursts In Non-Gaussian Noise: Locally Optimum and Robust Detectors”, 13-GWDAW, San Juan (USA), January 2009.

[42] Principe M et al. “Electromagnetic Reverberation Enclosures: a Chaos Based Approach”, XVII Riunione Nazionale di Elettromagnetismo, Lecce (Italy) September 2008.

[43] Principe M and Pinto IM “Rivelazione in rete di sensori di burst di onde gravitazionali non modellati in rumore impulsivo: un algoritmo localmente ottimo”, XCIV Congresso Nazionale Societ Italiana di Fisica, Genova (Italy), September 2008.

[44] Principe M and Pinto IM “Robust (Triggered) Network Detection of Unmodeled Gravitational Wave Bursts in Modeled Glitch Noise”, *LIGO conference document* LIGO-G080338-00-Z, LIGO-Virgo Meeting, 9-12 June 2008, Orsay, France.

[45] Conte R, Longo M, Marano S, Matta V, Pinto IM, Principe M (2007) “Workable Model of Non-Gaussian Noise”, *LIGO conference document*, LIGO-G070726-00-Z.

[46] Conte R, Longo M, Marano S, Matta V, Pinto IM, Postiglione F, Principe M, “A spherically Invariant Random Process Model for Interferometers Noise Floor”, *LIGO conference document*, LIGO-G070304-00-Z LIGO-Virgo Meeting, 21-25 May 2007, Cascina (PI), Italy.

[47] Principe M and Pinto IM “Network Detection of Unmodeled Bursts in a Glitch Background: Toward an Analytical Model”, LIGO-Virgo Meeting, 22-25 October 2007, Hannover, Germany.

[48] Pinto IM, Castaldi G, Pierro V, Principe M, “Coating Research at Sannio - Status”, *LIGO conference document*, LIGO-G070727-00-Z, LIGO-Virgo Meeting, 22-25 October 2007, Hannover, Germany.

[49] Principe M and Pinto IM “Glitch Rejection Properties of a Simple Network Detection Algorithm for Detecting Unmodeled GW Bursts”, *LIGO conference document*, LIGO-G070834-00-Z, 12-GWDAW, Boston (MA), USA, December 2007.

[50] Principe M and Sutton P “Modeling the performance of Networks of Gravitational Wave Detectors”, 10-GWDAW, Brownsville, (TX) USA, December 2005.

[51] Croce RP, Demma T, Fusco A, Pierro V, Pinto IM, Principe M “Binary Chirps banks: Tanaka Tagoshi Parameterization for LIGO”, 10-GWDAW, Brownsville (TX) USA, 14-17 Dicember 2005.

Awards

[52] Honorable mention, “Top three junior presentations”, XCIV Congresso Nazionale Societ Italiana di Fisica, Genova (Italy), September 2008.

[53] *Fulbright* Visiting Student Researcher Fellowship 2009/2010.

Preface

At the beginning of my PhD program, I became a memebr of the american-european LIGO-Virgo experiment, aimed at the detection of Gravitational Waves (GWs) through large-baseline interferometric antennas. In the LIGO-Virgo context, I studied two engineering issues of crucial importance for the experiment. These are in fact connected to the two dominant sources of noise, limiting the sensitivity of the instruments, i.e. the presence of spurious *glitches* at the output channel, and the thermal noise due to the dielectric coating, laid on top of the mirror test masses terminating the interferometer arms.

- The detection efficiency is seriously spoiled by the frequent occurrence of *glitches*, i.e. spurious transient signals due to environmental or instrumental disturbances of different origin. Glitches can mimic the effect of GWs, especially those belonging to the class of GW *Bursts*, i.e. bursts of gravitational radiation for which no model for the expected waveform is available yet. Currently implemented detection algorithms are designed ignoring such a disturbance, but equipping the data with *quality flags*, and applying *a posteriori* vetoes on detected events.

  I proposed a new way to tackle this problem, based on the developement of an analytical physically-driven model for the glitch noise component, which allows to derive a more accurate statistical description of the *total* noise corrupting the output of the interferometric antennas. Starting from the developed noise model, I designed two *locally* (in the weak signal limit) optimal detection strategies for GW *Bursts*, together with robust implementations which are tolerant against incomplete knowledge or fluctuations of the noise features. These strategies have been tested on simulated noise, first, and, then, on real LIGO noise. Furthermore, an existing pipeline, designed for the detection of GW *Bursts*, has been modified according to the proposed approach and tested. All experimental results agree with the expectations, proving the effectiveness of the developed theory in improving the detection efficiency in the presence of glitches, whose effect turns out to be sensibly reduced.

  The experimental part of this activity has been conducted in collaboration with prof.

S. Mohanty and S. Mukherjee from the University of Texas at Brownsville, where I spent six month supported by a 2009/2010 *Fulbright* fellowship for Visiting Student Researchers.

- Thermal noise due to dielectric coatings laid on top of the test masses is the dominant noise contribution in the most sensitive frequency band of the interferometric antennas. Therefore its reduction is crucial in increasing their sensitivity. Thermal noise is caused by a fluctuational redistribution of thermal energy inside each test masses. This energy redistribution produces a fluctuational change of the test masses' shape and thence a change of the position of their mirrored face, which mimics a GW-induced motion.
  In order to reduce such noise constribution, I formulated a systematic procedure to design *optimized* coatings, featuring minimal thermal noise, at the prescribed reflectivity level at one (*monochroic* design) or at two (*dichroic* design) operation wavelengths. Indeed the initial coating designs, based on the standard Bragg (quarter-wavelength) multilayer structure, although being optimal as far as concerns the optical requirements, were found to not achieve the minimum of the thermal noise.
  According to the formulated optimization strategy, two prototypes have been realized by the *Laboratoires des Materiaux Avances* in Lyon (France), designed for the single and double wavelength operation, respectively. Experimental measurements on the *monochroic* prototype have been done at Caltech, Pasadena (USA), resulting in perfect agreement with theoretical expectations. Measurements on the dichroic prototype are currently under work at Caltech. The proposed optimization procedure will be likely adopted to design coatings for the advanced configuration of LIGO interferometers.

The results obtained during theses activites have been published in 5 papers on international scientific journals, in 6 LIGO technical reports, and presented at 6 international and 5 national conferences. Furthermore, I published 20 papers on internation scientific journal with the LIGO-Virgo collaboration.
In 2008 I obtained the honorable mention "Top three Junior Presentations" at XCIV national meeting of Societa Italiana di Fisica.
In 2009/2010 I obtained the *Fulbright* fellowship for Visiting Student Researchers.
I have been members of examination committes for Electromagnetic Fields classes.

I would like to thank my tutor, prof. Innocenzo M. Pinto, who always believed in my capabilities, for his support during my PhD activities.

I am also very thankful to all the people of the *Waves group* at University of Sannio, especially to ing. A. De Vita, prof. A. Borzí, ing. G. Castaldi, prof. V. Galdi and dr. M. Wogrin, for their friendship and wise suggestions.
I acknowledge the *Fulbright* program and the tutors during my visit at University of Texas, prof. S. Mohanty, prof. S. Mukherjee and prof. M. Diaz.
I heartly thank Marco, and my great family.
Last but not least, I thank God, Who made all this possible.

The present dissertation is organized as follows:

- chapter 1 deals with the basic properties of Gravitational Waves, and the main classes of astrophysical sources. The principles at the base of GW antennas are introduced, as well as the dominant sources of noise corrupting their output channel;
- chapter 2 deals with the main features of the noise occurring at the output of the interferometric antennas. The developed model for the glitch component is described in detail, as well as it statistical properties;
- chapter 3 treats the detection of unmodeled gravitational wave *bursts* in a multiple-antenna context. Two *locally optimum* detection strategies are discussed;
- in chapter 4 numerical results about the performance of detection strategies proposed in chapter 3 are shown, evaluated both in simulated and in real LIGO noise;
- chapter 5 deals with the theory of the thermal noise in LIGO test masses, starting from the basic principles;
- in chapter 6 the optimization strategies to design minimal thermal noise coatings for LIGO test masses are formulated in both single and double wavelength operation;
- chapter 7 holds the conclusions and a discussion about the obtained results.

Contents

Sommario **1**

Resume **3**

List of publications **5**

Preface **11**

1 Gravitational Waves **19**

1.1 Historical Outline 20
1.2 GW Astronomy 21
1.3 GW Basics 21
1.4 GW Antennas 24
1.5 GW Sources 26
1.5.1 Binary Systems 27
1.5.2 Spinning Neutron Stars 27
1.5.3 Stellar Collapses and Supernovae Explosions 27
1.5.4 Gamma-Ray Bursters 28
1.5.5 Stochastic GW Background 28
1.6 Noise Budget in IFOs 29
1.6.1 Seismic Noise 29
1.6.2 Thermal Noise 30
1.6.3 Shot Noise and Radiation Pressure Noise 30

2 Interferometer Noise: Toward a Physically Driven Model **33**

2.1 Gaussian or non-Gaussian Noise Model? 34
2.2 A Statistical Description of IFO noise 35
2.3 A Physical Model for Glitch Noise 39

2.4 Simulating Glitch Noise . . . 42

3 Locally Optimum Network Detection of GW Bursts in Glitchy Noise 45

3.1 Locally Optimum Detection of Known GW Signals with Multiple Sensors . . 46

3.2 Locally Optimum Detection of Unmodeled GW Bursts with Multiple Sensors 50

3.2.1 GWBs as Unknown Deterministic Signals . . . 51

3.2.2 GWB as a Random Signal . . . 57

3.3 Locally Optimum Network Detection for Correlated Noise . . . 58

3.3.1 The Known Signal Case . . . 59

3.3.2 GWBs as Unknown Deterministic Signals . . . 61

3.3.3 The Random Signal Case . . . 63

3.4 Robust and Nonparametric Implementation . . . 64

4 Numerical Results 67

4.1 Simulated Noise . . . 68

4.2 Real LIGO S5 data . . . 73

4.3 The modified RIDGE pipeline . . . 75

5 Thermal Noise in Interferometers 85

5.1 Basics of Thermal Noise Theory . . . 86

5.1.1 Internal Friction . . . 88

5.1.2 Thermo-Elastic Noise . . . 91

5.1.3 Thermo-Refractive Noise . . . 92

5.2 Thermo-Optic versus Brownian Noise . . . 93

6 Coating Optimization for minimal Thermal Noise 95

6.1 AdLIGO Coating Requirements . . . 96

6.2 Multilayer Coating Reflectivity . . . 98

6.3 Monochroic Optimization . . . 100

6.3.1 The Reference Design . . . 100

6.3.2 The Optimized Design . . . 100

6.3.3 Direct Measurements . . . 103

6.4 Dichroic Optimization . . . 104

6.4.1 The Reference Design . . . 104

6.4.2 The Optimized Design . . . 106

7 Conclusions 117

References **119**

A Derivation of the GCC detection statistic **131**

B Thermo-Refractive Noise in non-QWL Coatings **135**

List of figures **139**

List of tables **145**

Chapter 1

Gravitational Waves

In this Chapter, I attempt a minimal outline of General Relativity theory, according to which Gravitational Waves (GWs) exist. The main properties of the gravitational radiation are then described, as well as the astrophysical systems which are supposed to emit GWs. Interferometric GW antenna and the main sources of noise corrupting their output are introduced.

1.1 Historical Outline

The existence of Gravitational Waves (GWs) is one of the most interesting prediction of the theory of General Relativity (GR) [126], formulated at the beginning of the XX century by Albert Einstein.

Before Einstein's theory, Newton's theory of gravity stated that, when a mass changes position, the entire gravitational field throughout the universe changes instantaneously, and the resultant gravitational forces are instantly changed accordingly.

On the contrary, Einstein's Theory of General Relativity asserts that no information can travel faster than the speed of light, including information on the positions of mass in the universe, which is communicated through the gravitational field. GR theory predicts that a change in gravitational field will travel through the universe at the speed of light as a gravitational wave.

In GR, gravity is described as curvature of the space-time, and in the presence of such curvature objects move along geodetics which are no more straight lines. The dual role of mass, as a measure of the inertia and as source of gravitation, which stays unexplained by the Newton's theory, is the key concept in the GR.

The existence of gravitational radiation has not been directly proved nor disproved up to now. Einstein himself was doubtful about the possibility to detect a GW, due to its *extreme* weakness. This challenge was accepted by Joseph Weber from University of Maryland, who built the first antenna for detecting GWs, based on measuring their effect on the fundamental mode of an alluminium cylinder [105]. Over 10 years he built different resonant antennas placed in laboratories far apart, and tried to indentify coincident events, that could be correlated with events of cosmic origin. Although his claims of detecting some events were then disproved, he opened a way to new experiments. The italian research has played a significant role in this context, first with the group of Edoardo Amaldi, and now with the Virgo experiment.

Until now, the only valid, though indirect, evidence of the existence of GWs has been obtained through the observation over a period of several years of the binary pulsar PSR1913+16 by Hulse and Tylor, who won for this study the Nobel prize in 1993 [94]. They measured the orbital parameters of the binary system and the observed orbital period decrement turned out to be consistent with GW energy loss within a fraction of 1%.

1.2 GW Astronomy

Whenever a new observational window to the physical Universe has been opened, as e.g. with the birth of radio-astronomy, and the observation of the nonvisible part of the EM spectrum, our knowledge of it has substantially evolved. However the actual knowledge about the Universe is almost entirely based on the observation of the electromagnetic radiation. The direct observation of GWs of cosmic origin is expected to provide the next (r)evolution. Indeed, differently from the electromagnetic radiation, gravitational radiation can travel in space with only minimal absorbtion by the matter, carrying information about cosmic systems, which would be otherwise concealed by the opacity of matter to the EM radiation.

Among the added or new insights brought by GW astronomy, I quote:

- Detailed information on the properties of neutron stars (henceforth NS), including the equation of state of hadronic matter;
- Direct probing of the physics of collapsed objects (black holes) (henceforth BH);
- Tests of general relativity under extreme strong-field conditions;
- Measurement of the propagation speed and polarization properties of gravitational radiation;
- Insights into the evolution of the early universe, from measurement of relic primordial gravitational waves;
- Study of galactic evolution driven by the massive black holes forming at their centers;

In addition, there is quite a potential for discovering new and unanticipated phenomena.

1.3 GW Basics

A fundamental concept of the Special Theory of Relativity [14] is that the interval ds, defined in eq. (1.1), between two points in the space-time structure is invariant for all inertial reference frames,

$$ds^2 = dr^2 - c^2 dt^2 = \eta_{\alpha\beta} dx^\alpha dx^\beta, \tag{1.1}$$

where dr is the space distance and dt the time interval between the two events, c is the speed of light, $\eta_{\alpha\beta} = diag\{1,1,1,-1\}$ is the Minkownsky tensor, $x = \{r_x, r_y, r_z, ct\}$, and Einstein's rule of summation over repeated suffixes/superfixes $\alpha, \beta = 0,1,2,3$ is implied.

The invariance of ds is tantamount to state the invariance of the speed of light among all inertial reference observers.

Due to the Galilei's equivalence principle, gravity is locally canceled in a freely falling reference frame (and in any frame obtained thereof by an inertial tranformation), since all bodies fall in the same way under the same gravitational field. Hence, in such a frame eq. (1.1) is valid. Applying a coordinate transformation, from the freely-falling reference x^α to the laboratory one ξ^α, where gravity is not canceled, ds reads

$$ds^2 = g_{\mu\nu} d\xi^\mu d\xi^\nu, \tag{1.2}$$

where $g_{\mu\nu} = \eta_{\alpha\beta} \frac{\partial x^\alpha}{\partial \xi^\mu} \frac{\partial x^\beta}{\partial \xi^\nu}$. In the presence of gravity, spacetime (the events continuum) is thus described as a 4-dimensional Riemannian manifold, with metric tensor $g_{\mu\nu}$. The presence of gravity implies the lack of a global (i.e. non local) transformation reducing the tensor $g_{\mu\nu}$ to $\eta_{\alpha\beta}$, and this happens only if the space-time structure presents a *curvature*.

Einstein's equations connect $g_{\mu\nu}$ to the mass and energy distributions of sources of gravity, and they are highly complex and non linear. The interested Reader may refer to [109] for a complete discussion. However, in a perturbative approach, it is possible to write

$$g_{\mu\nu} = \eta_{\mu\nu} + h_{\mu\nu}, \tag{1.3}$$

where $h_{\mu\nu}$ represents a deviation from the Minkowsky metric, due to the presence of gravity.

In the weak field regime, Einstein's equation can be linearized, and, as he proved first, they admit as solutions transverse plane waves, propagating without dispersion at speed c.

A gauge freedom is connected to the choice of the laboratory reference frame. A particular gauge makes very clear the representation of these waves, viz. the *transverse traceless (TT) gauge*. With this choice of coordinates, in the weak field regime, Einstein's equation becomes an ordinary wave equation [109]

$$\left(\nabla^2 - \frac{1}{c^2}\frac{\partial^2}{\partial t^2}\right) h_{\mu\nu} = 0. \tag{1.4}$$

The metric deviation of a plane gravitational wave propagating in the z-direction can be cast in the form

$$h_{\mu\nu} = \begin{pmatrix} 0 & 0 & 0 & 0 \\ 0 & h_+ & h_\times & 0 \\ 0 & h_\times & -h_+ & 0 \\ 0 & 0 & 0 & 0 \end{pmatrix}. \tag{1.5}$$

Gravitational waves are accordingly transverse, and are superpositions of two fundamental linear polarization states, uniquely determined by the functions $h_+(z-ct)$ and $h_\times(z-ct)$ in (1.5). These latter, also called the TT components of $h_{\mu\nu}$, are given by

$$h^{(TT)}(\mathbf{r},t)=\frac{2G}{c^4 r}Q^{(TT)}\left(t-\frac{r}{c}\right), \tag{1.6}$$

where Q is the reduced quadrupole moment of the source, viz.

$$Q_{ij}(t)=\int d^3x\left(x_i x_j-\frac{1}{3}x^2\delta_{ij}\right)\rho(\mathbf{r},t), \tag{1.7}$$

ρ being the source mass density.

The analogies between (weak-field) gravitational waves and electromagnetic (EM) waves are evident. There are, however, several differences. The GW field is proportional to the retarded quadrupole source moment (instead of the dipole, as in EM field). In addition, the source motion is built in the (full, nonlinear) wave equations (Bianchi identities, [109]). Finally, absorption and dispersion of GW by ordinary matter is extremely weak (as a direct consequence of the equivalence principle [109]).

The following back of an envelope order of magnitude estimates of GW amplitude, frequency and decay time as a function of the gross source parameters may be derived from the above formulas, under extreme condition (compact, ultrarelativistic sources) [109]:

$$\begin{gathered} h\sim 10^{-21}\left(\tfrac{15Mpc}{r}\right)\left(\tfrac{M}{2.8M_S}\right)^2\left(\tfrac{90Km}{r}\right), \\ f\sim 10^{2}\left(\tfrac{M}{2.8M_S}\right)^{1/2}\left(\tfrac{90Km}{r}\right)^{3/2}Hz, \\ \tau\sim 0.5\left(\tfrac{90Km}{r}\right)^{-4}\left(\tfrac{M}{2.8M_S}\right)^{-3}s, \end{gathered} \tag{1.8}$$

where M_S is the solar mass and r is the source-antenna distance.

Monochromatic weak GWs exert transverse tidal forces, which distort a ring of freely-falling test particles in a plane orthogonal to the wave vector as shown in Figure 1.1. This can be properly regarded as a wiggling of the test-particles geodesics.

If L is the diameter of the particles ring, the change ΔL due to the impinging GW, with amplitude h, is

$$\Delta L=hL. \tag{1.9}$$

A similar wiggling also affects the electromagnetic lines of force, and can be described as a GW induced modulation of the dielectric properties of vacuum [109].

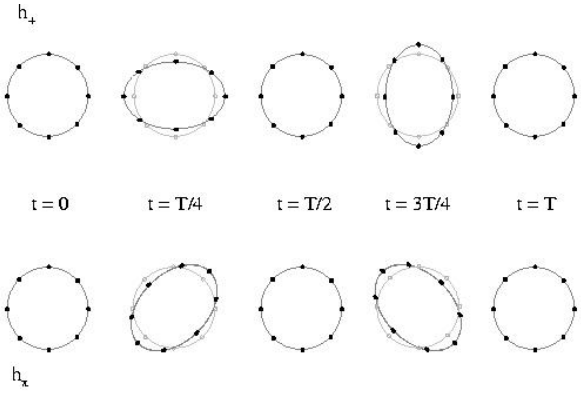

Figure 1.1: A plane circular ring of test particles under the action of a plane monochromatic GW with angular frequency $\omega = 2\pi/T$

From eqs. (1.8) it is possible to compute roughly the amplitude of GWs produced by typical astrophisical events, where very massive objects are involved. This turns out to be in the range $10^{-26} - 10^{-21}$, requiring a very sensitive detection instrument.

1.4 GW Antennas

As already mentioned, GWs interact with matter by compressing objects in one direction while stretching them in the perpendicular direction, with a frequency and an amplitude connected to the properties of the wave. GW detectors are based on this interaction.

The first experimental apparatus for detecting GWs were acoustic detectors built by J. Weber [105]. A few acoustic detectors are still in operation [1]. Acoustic detectors are high-Q (cryogenic) mechanical resonators set into ringing by the action of a GW. Typical resonance frequencies range from 800 Hz to 1 KHz, with bandwidths $\sim$ 10 Hz. Plans for wideband 2nd generation acoustic detectors are presently in the R&D stage [62].

A second class of GW antennas, which are the most sensitive detectors presently in operation, are based on Michelson interferometers [130], and their operation scheme is schetched in Figure 1.2. Interferometers (IFOs) have both higher sensitivity and larger bandwidhth than acoustic resonators.

An interferometer performs a (differential) measure of the stretching-and- squeezing induced by a GW in the distances between two couples of mirrors (test masses), which form two optical cavities with orthogonal axes, coupling optimally to the quadrupole GW field. A coherent monochromatic light beam is used to read off the differential displacement: it is split in two beams traversing the two optical cavities and then recombining at the pho-

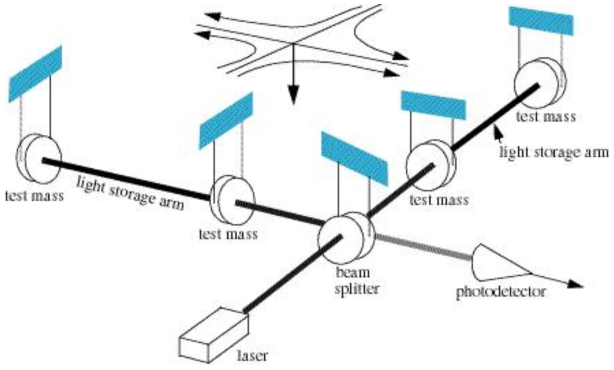

Figure 1.2: The bare-bones of an interferometric GW antenna.

todetector. What is measured in practice is the intensity of the dark fringe, related to the phase-difference acquired by the recombining beams. If the interferometer arms are of equal length, the two beams interfere distructively at the photodetector, which sees ideally no light at all, while they interfere constructively heading back to the laser source. If a GW impinges the interferometer, it stretches and squeezes alternatively the two arms, producing difference in the arms length and light intensity modulation at the photodetector, which is the signature of the GW. In this case the phase difference of the recombined beams is

$$\Delta\phi = 2\pi \frac{2\Delta L}{\lambda}, \tag{1.10}$$

where ΔL is the difference in length of the two arms and λ is the wavelength of the light. The differential arm length variation, according to eq. (1.9), is given by

$$\Delta L = L(F^{+}h^{+} + F^{\times}h^{\times}), \tag{1.11}$$

where L is the nominal cavity length, and the factors $F^{+,\times}$ (which bear some analogy with the effective height of EM antennas) describe the directional response of the interferometer, depending on the orientation of the GW polarizations with respect to the IFO arms. To increase the accuracy in measuring ΔL, actual instruments use Fabry-Perot cavity arms, where the light beam folds many times, to increase the effective optical path by a factor equal to the finesse of the cavities [130].

The following interferometric GW detectors are presently operational:

- LIGO - The US Laser Interferometer Gravitational-Wave Observatory built and operated by Caltech and MIT, leading an international Scientific Collaboration [2], consists of three instruments: a 4Km interferometer in Livingston, LA (nicknamed LLO), and another two (4Km and 2Km long) in Hanford, WA (nicknamed LHO). The two sites are about 3000Km apart, and the instruments are engineered so as to support coherent/coincidence analysis of events. In 2007 the two big LIGOs entered an extended upgrade phase, toward their advanced configuration (AdvLIGO, [145]), which is planned to be in operation in both observatories by 2014;

- Virgo - The three kilometer French-Italian detector is located in Cascina (Pisa, IT) [3]. The main difference in Virgo interferometer with respect to LIGO ones is that it uses a different, very sophisticated seismic isolation system, allowing higher sensitivity at low frequencies;

- GEO600 - A six hundred meter interferometer constructed by a German-English collaboration near Hannover, Germany [4]. Despite its smaller size it incorporates several advanced features from the beginning, and is being used as a technology testbed for the next generation instruments;

- TAMA300 - The small (three hundred meter) interferometer operating at the National Astronomical Observatory in Tokyo was the first to come into operation, in 1999 [5]. The Japanese TAMA Collaboration is presently designing a full scale cryogenic interferometer [6], of which a 100m prototype has been already demonstrated [81].

An additional large facility, the Einstein telescope [7] is under development.

1.5 GW Sources

Gravitational waves of cosmic origin occupy an extremely wide spectral range, spanning 22 decades, from 10^{-18} to 10^4 Hz. In this Section I shall briefly review the main classes of sources, emitting gravitational radiation in the spectral range accessible to Earthbased detectors, viz. $10^1 - 10^4$ Hz, to which the present study strictly applies[1]. The interested Reader may address [109] for a complete coverage. GW sources of astrophysical nature in the IFO observational band may radiate a variety of signals, including bursts, chirps, long-coherency (quasi-monochromatic) waveforms, and stochastic backgrounds, as briefly reviewed hereafter.

---

[1] Planned space-borne gravitational wave detection experiments, like LISA [8] and DECIGO [137] will be able to explore the frequency range from 10^{-4} to 100 Hz.

1.5.1 Binary Systems

Binary systems consist of two bodies orbiting around each other, through three successive phases: 1) inspiral, where the orbit shrinks and circularizes adiabatically under the emission of gravitational radiation; 2) merger, where the binary companion stars eventually collide and coalesce; and 3) ringdown, where the final object settles into an equilibrium state. During the inspiral phase, both the amplitude and frequency of the emitted GW rise in a characteristic way, producing a chirp that sweeps across the detector's band (from 10 Hz to $\sim$ 1 KHz during the final 15 min for a NS-NS inspiral). A NS-NS inspiral may be observed by the LIGO detector (at the current nominal sensitivity) up to a distance of $\sim$ 20 Mpc (350 Mpc for advanced-LIGO)[2]. For BH-BH inspirals, the visibility distance for LIGO may be 100 to 1000 Mpc, depending on the companion masses. The estimated event rate for NS-NS coalescences of 10^{-2} per year in the visibility sphere of the initial LIGO detectors; the BH-BH rate being $\sim$ 10 times larger [19]. Advanced detectors will boost the visibility volume (and event rates) by an expected factor of $\sim 10^3$.

1.5.2 Spinning Neutron Stars

Non-axisymmetric spinning neutron stars will radiate nearly monochromatic GWs at twice their spinning frequency. NS spinning frequencies span the whole observational window of Earth based detectors [77]. The fastest spinning known pulsar has a rotation frequency of $\sim$ 1114 Hz [74]. Upper limits on the GW amplitude (set by observing the spindown of known pulsars, assuming the only mechanism for energy loss to be GW emission) are in the range 10^{-25} to 10^{-27}, whereby coherent detection would require observations lasting several months or years [129]. The nearly monochromatic GW signal of a pulsar undergoes a complicated Doppler modulation at the detector, due to Earths rotational and orbital motion, in a way which depends on the (unknown, in general) source position in the sky [129]. A worldwide computer-farm has been recently set up to implement the numerically formidable task of blind all-sky search of GWs from spinning NS [9].

1.5.3 Stellar Collapses and Supernovae Explosions

The collapse of a massive star, occurring after gravitation implosion overwhelms the pressure sustained through nuclear burning, results in a supernova explosion, leaving a compact remnant (NS or BH). The process, if sufficiently asymmetric, will produce bursts of GWs.

---

[2] One parsec (pc) is the distance traveled by the light in one second, in vacuum

Extensive numerical simulations of supernova explosions based on general-relativistic hydrodynamics exist [44]. However, no such thing as a parametric GW template family is available. Detection of unmodeled bursts from supernova explosions is complicated by the presence of impulsive noise (*glitches*) of instrumental origin, and thus can be effectively implemented only exploiting coherency among several detectors. Luckily, supernova explosions produce strong optical and neutrino emissions, which can be used to trigger GW detection [73]. Out to a distance of 10 Mpc, a supernova event occurs about once per year.

1.5.4 Gamma-Ray Bursters

Gamma-ray bursts (GRB) are the most luminous known astrophysical sources, releasing about 10^{51} to 10^{54} erg in each flash, lasting from 1 to 10^2 s. Several competing source models have been proposed [68], sharing consensus that BHs should be involved. The strength of GWs radiated by GRB is yet uncertain. Estimates range from $h \sim 10^{-22}$ to $h \sim 10^{-25}$, depending on the model. Burst of GW associated to GRB are being actively sought [48].

1.5.5 Stochastic GW Background

Similar to the (stochastic) cosmic microwave background, the GW stochastic background originates from fundamental phenomena in the early Universe (phase transitions, inflation, higher dimensions, topological defects etc. [116]). It would show up as an additional Gaussian noise component in the detectors outputs, which correlates in a peculiar direction dependent way [116]. Its strength is measured as a fraction Ω_{GW} of the energy density ρ_c needed to make the Universe gravitationally closed. Depending on the cosmological model [116] Ω_{GW} may range between 10^{-14} and 10^{-5}. For the presently most credited model, the GW background should be observable in the frequency range 0.1 to 1 Hz, which falls beyond the reach of Earth-based detectors. Upper limit on the GW stochastic background are nonetheless sought, putting limits to alternative cosmological theories.

In order to detect GW signals buried in noise, accurate knowledge of the signal waveforms is desirable. Calculating GW radiated waveforms is a difficult task[3]. Noteworthy successful paradigms, directly related to the sought sources discussed above, include the analytic post-

---

[3] Solving the Einstein equations involves 10 coupled, nonlinear partial differential equations, subject to dynamically evolving boundary conditions. The calculations are also complicated by the possible occurrence of singularities [S.W. Hawking and G.F.R. Ellis, *The large Scale Structure of Spacetime*, Cambridge UK, Cambridge Un. Press (1973).]. The coordinate system and gauge conditions may be freely chosen, but in most cases the appropriate choice is not obvious, and may be physically questionable.

Newtonian modeling of the compact 2- body systems [110], and the numerical studies of BH mergers [51] and supernova explosions [66]. Gravitational radiation from spinning NS [103], and the stochastic background of relic GW from the early Universe [116] are also credited as being reasonably well understood. It should be noted that waveforms may be known except for the actual values of a number of source parameters. In these cases, a bank of matched filters is needed to implement the detection and the estimation of parameter [96], which may be extremely large and computationally expensive. This is the case, e.g., of elliptical binaries with spinning companions [89], and of spinning NS with unknown location in the sky, [129], and consequently unknown Doppler modulation of the signal due to the Earths motion.

1.6 Noise Budget in IFOs

Earth-bound IFOs are affected by several sources of noise at the photodetector port in the absence of a real GW signal. If $S_n(f)$ is the Power Spectral Density of the output noise, this latter mimics a GW signal whose amplitude spectral density is

$$h_n(f) = \sqrt{S_n(f)}\frac{1}{\sqrt{Hz}}. \tag{1.12}$$

This means that a GW to be detected must be at least one order of magnitude above the noise level, or, equivalently, the Signal to Noise ratio, defined as

$$SNR = \sqrt{2}\int_{-\infty}^{+\infty}\left[\frac{|h_{GW}(f)|^2}{S_n(f)}\right]df \tag{1.13}$$

must be ≥ 10.

I describe briefly in this Chapter the main sources of noise, limiting the IFO sensitivity and summing up in the total IFO noise curve, whose typical trend is shown in Figure 1.3.

1.6.1 Seismic Noise

Ground vibrations, due to both human activities and to phenomena of geophysical and atmospherical nature, is the main disturbance at frequencies below 50 Hz. At a quite site on Earth, seismic noise follows a spectrum in all three dimensions close to $10^{-7}f^{-2}m/\sqrt{Hz}$. A good suppression of this noise source is obtained by suspending the test masses at the ends of the IFO arms through special pendulum system, whose transfer function falls off as f^{-2} above the resonance frequency. Due to seismic noise, the detection of low frequency GWs is not possible with ground based IFO; it could be feasible with space-borne version IFOs [8].

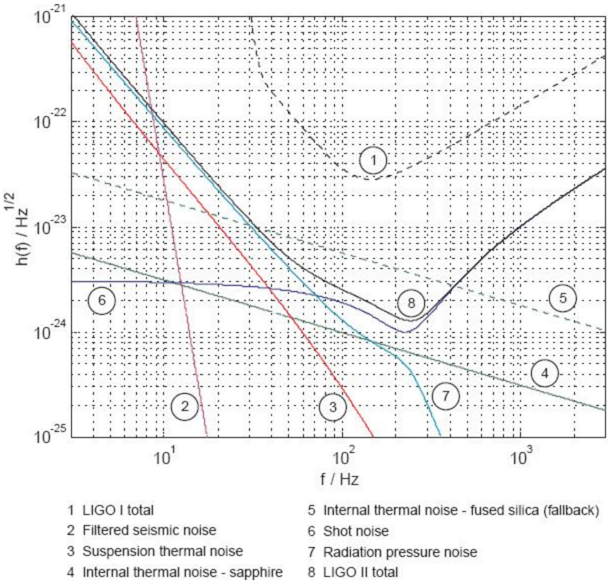

Figure 1.3: Main contributions to a typical noise curve of an IFO

1.6.2 Thermal Noise

Internal thermal noise is the dominant noise source in a interferometric GW detector in the frequency range bewteen 10 Hz and 200 Hz. It is caused by a fluctuational redistribution of thermal energy inside each of the IFO test masses. This energy redistribution produces a fluctuational change of the measured test mass (differential) displacement, which in turn mimics a GW-induced motion [130]. The fluctuation-dissipation theorem [25] describes a relationship between thermal noise and the energy dissipation (entropy increase) that occurs inside the test mass, when the front of the test mass is subjected to an oscillatory driving force. There are various types of internal thermal noise, each one associated with a specific dissipation mechanism, Brownian thermal noise, Thermo-Elastic noise, and Thermo-Refractive noise. Beside the test masses, including the dielectric coating, their suspensions are sources of thermal noise as well. Thermal noise will be treated in great detail in Chapter 5.

1.6.3 Shot Noise and Radiation Pressure Noise

Both shot noise and radiation pressure noise are due to the quantum nature of light. Shot noise is the limiting factor at frequencies above 10^2 Hz and it is due to random fluctuations in the number of detected photons. These fluctuations give rise to noise in the measured phase shift, which can be reduced by increasing the input laser power.

The radiation pressure noise is due to the pressure exerted upon the mirrors by the light beam. It is larger at low frequencies, and increases with the input laser power. Hence an optimal input power must be chosen, in order to minimize the shot noise and to prevent the radiation pressure noise to limit sensitivity at low frequencies. A proposed way to reduce this noise constribution is by using squeezed light (see e.g. [13]).

Other less relevant sources of noise affect the IFO output, e.g. laser frequency and power fluctuations, random fluctuations of molecular gas density along the optical path of laser beam resulting in refractive index fluctuations, etc.

Chapter 2

Interferometer Noise: Toward a Physically Driven Model

In this Chapter I describe the main features of the noise corrupting the data gathered at the interferometer's output. Its statistical properties are markedly different from those of a pure Gaussian noise. Nonetheless, currently implemented detection pipelines are based on the Gaussian model, mainly because of the lack of a rigorous statistical model for the non-Gaussian noise component. I introduce a physically-driven model for such a non-Gaussian component, in the perspective of deriving, in the next Chapter, *optimal* detection strategies. The statistical characterization of the proposed noise model is presented, and its main features are discussed.

2.1 Gaussian or non-Gaussian Noise Model?

Most, if not all, currently implemented pipelines for the detection of GW signals are based on detection statistics derived in the assumption that the corrupting noise is a pure Gaussian random process (see e.g. [63, 72, 138]). Although this assumption entails a significant simplification in the detection statistic structure, it is definitely unrealistic, since several non-Gaussian features occur at the data channel of all interferometric GW antennas.

Looking at this noise, two main kinds of non-Gaussianities can be identified: *narrowband spectral lines*, and transient spurious signals, known as *glitches*.

Many spectral *lines* are visible in the power spectrum, some due to deterministic known sources, and others due to environmental and/or instrumental disturbances, occurring at varying frequencies.

Among deterministic lines, it is possible to distinguish those due to coupling to power supply conduits, occurring at integer multiples of the standard frequency (50/60 Hz) of the power mains, from those originating from the high-Q mechanical resonances of the wire slings hanging the terminal mirrors. The former may cause *substantial* deviations of the noise distribution from the Gaussian assumption. The latter, known as *violin-modes*, are linear responses to stochastic excitations, and as such, they may or may not produce a (narrowband) Gaussian noise component, depending on whether the underlying stochastic excitation of the wires is itself Gaussian (Brownian noise) or not (creep noise in the wires, due to material dislocation [61]). This latter turns out to be negligble in fused silica suspensions [11]. Efficient algorithms have been developed for tracking and subtracting from the data the narrowband features due to both power lines [23, 45, 123], and violin-modes [93, 141]. Figure 2.1 shows a typical PSD trend corrupted by spectral lines.

An additional important source of non-Gaussianity is the occurrence of *glitches*, i.e. short high-energy signals caused by events of different nature: man-made, environmental, or instrumental. We can distinguish *loud* glitches, which are easily detectable against the noise floor, from *weak* glitches, which are embedded in the noise background and cannot be easily identified as such. Loud and weak glitches can be caused, e.g., by micro seismic due both to natural and human activities, by coupling to magnetic fields, to acoustic signals, or to RF fields, or by the presence of dust in the cavity. In order to distinguish spurious glitches from real GW signals, hundreds of interferometer control (various servos for interferometer and laser locking, suspension, cavity alignment, etc.) and auxiliary channels monitoring the local environment (seismomters, acceleterometers, microphones, magnetometers, radio receivers etc.) have been activated.

The control and auxiliary channels are analyzed in order to track the correlation of

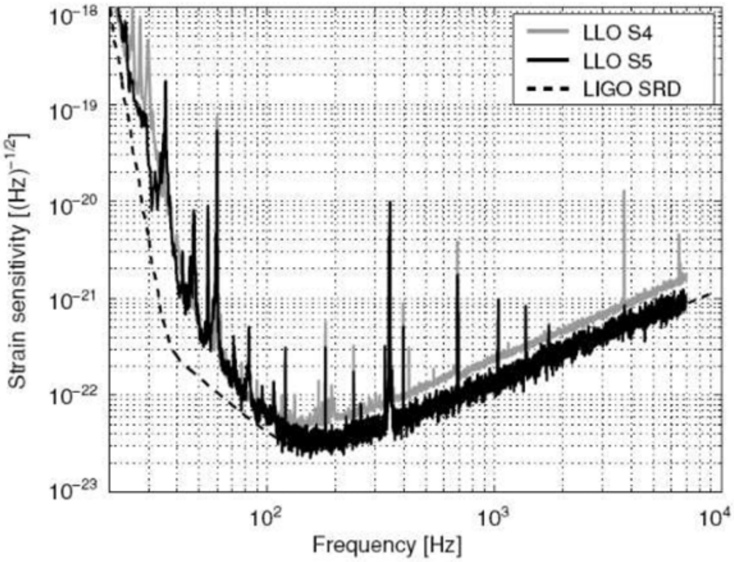

Figure 2.1: PSD corrupted by spectral lines.

specific noise sources with the data channel and to identify spourios events in this latter which could be misidentified as GWs [60]. This analysis allows to implement two kinds of data laundering procedures. The first one consists in identifying time stretches (from 1 to many seconds) where the instrument is not working properly for different reasons, and exclude the corresponding chunks from the search. This procedure is called *Data Quality Flagging* (DQ), and DQ flags are organized in few categories depending on the severity of the associated problems and on our capability to understand their origin [60]. The second procedure consists in identifying events exhibiting high correlation with the output of one of the auxiliary channels, and vetoing out an interval (typically 100ms to 1s long) of data around the corresponding trigger (*Event-by-Event* vetoes). However, there are still many glitches appearing at the output channel, whose sources cannot be identified, and which do not correlate with any of the auxiliary channels. Figures 2.2 and 2.3 show an example of weak and loud glitches, respectively, which have been detected at the output GW channel at LLO.

2.2 A Statistical Description of IFO noise

Glitches represent nowadays the main source of noise impairing the efficiency of the detection algorithms. Their effect is particularly detrimental in the search for GWBs, for which no model for the expected waveform exists. As already mentioned, the rejection of spurious

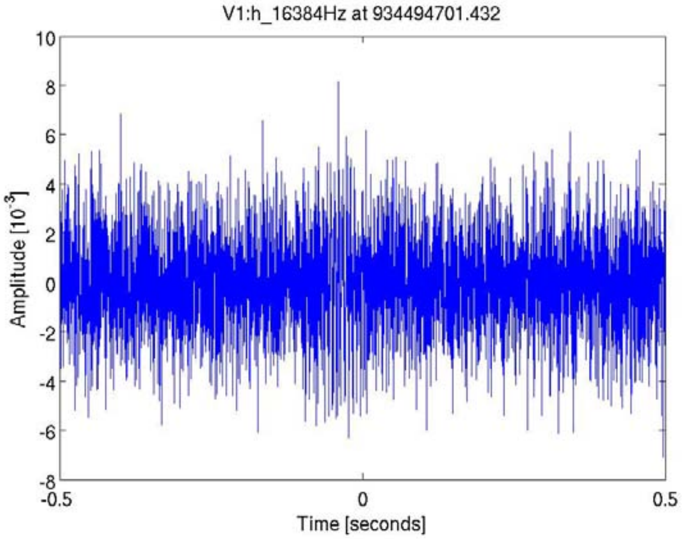

Figure 2.2: Example of weak glitch occurring at LLO.

glitches is currently performed by vetoing out those events in the GW channel, which exhibit high correlations with the output of some auxiliary channels.

However, the procedure for this selection is purely heuristic, and in view of the non-stationarity of the data, it must be updated frequently.

The lack of a rigorous way to handle glitches poses the problem of developing a plausible model for them. This would result into a model for the total IFO noise, which would take into account the typical features, which are observed in *all* such instruments presently in operation, and make the statistical properties of noise *markedly* different from those of an ideal Gaussian process. Several research groups have engaged in the study of glitches, most of which focused on identifying generic glitch features and classifying glitch waveforms (see e.g. [140]). However, setting up a *statistical model* for the glitch component of the noise is essential in deriving *optimal* detection strategies, which by construction embed glitch rejection capabilities and therefore do *not* need ad-hoc checks or event vetoes. This is a strong motivation for introducing a plausible statistical model for the glitch noise component, and in this thesis I moved the very first steps toward this.

Glitch noise will be therefore modeled as an *impulsive* random process, represented as a *generalized shot-noise* [40], viz.:

$$\nu_g(t) = \sum_{k=1}^{K[T]} \psi(t - t_k; \vec{a}_k), \tag{2.1}$$

where $K[T]$ is a random variable, representing the total number of glitches occurring in the

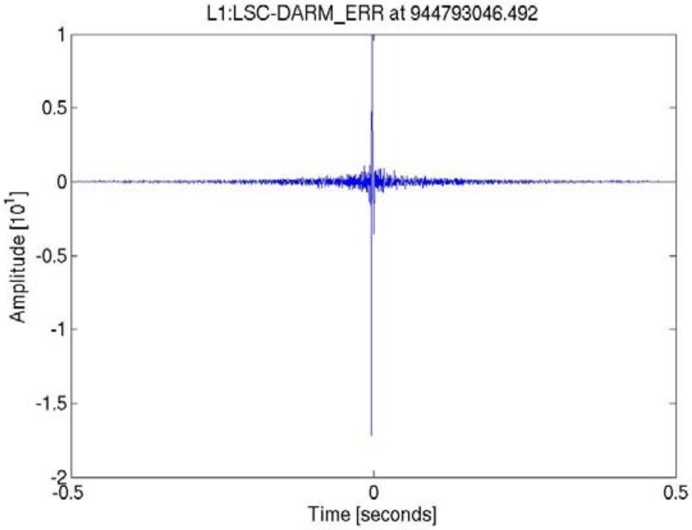

Figure 2.3: Example of loud glitch occurring at LLO.

analysis window, whose duration is denoted by T; the t_k form a set of (random) firing times, while $\psi(t;\vec{a})$ is a function with compact time-support (a transient), representing individual glitches, whose form is set by a (random) vector $\vec{a}$ of shape parameters, e.g. amplitude, center frequency, time duration, etc.

Different glitches in eq. (2.1) are likely to be due to *indepedent* disturbances and it is thus reasonable to assume the random firing times as being independent and identically distributed. We shall denote by $\lambda(t)$ the time-varying glitch rate, i.e. expected number of glitches per unit time. Under the made assumptions, a theorem by Hurwitz and Kač [92] entails that the total number of glitches in (2.1) will be ruled by a (non-homogeneous) Poisson process [132], with

$$\text{prob}[K(T)=Q]=\frac{(\bar{\lambda}_T T)^Q\exp(-\bar{\lambda}_T T)}{Q!},\ \text{where}\ \bar{\lambda}_T=T^{-1}\int_T dt\lambda(t), \tag{2.2}$$

$\bar{\lambda}_T$ being the average (local) glitch-rate in the data analysis window. We shall assume the fluctuations of $\lambda(t)$ and/or other parameters in eq. (2.1) to occur on time scales $\gg T$, so that fo analysis windows we consider they can be taken as constants. Middleton in [40] noted that a key parameter is $\gamma=\lambda\overline{\tau}$, i.e. the product bewteen the glitch rate and the expected glitch duration, which corresponds to the expected number of "glitchy" samples per unit time: if $\gamma \gg 1$ there are many glitches overlapping in a single time sample, the distribution of (2.1) becomes Gaussian, by virtue of the Central Limit Theorem, irrespective of the glitch shape; if, on the contrary, $\gamma \approx 1$ the distribution presents heavy non-Gaussian tails whose behaviour depends on the glitch shape.

Strong glitches, defined as those which are clearly *detectable* against the noise floor (using, e.g., a change-detection algorithm [42,95,114]), are found to occur at typical rates up to ~ 1 s^{-1}, such that $\gamma \leq 1$, producing non-Gaussian heavy tails in the final distribution.

As a matter of fact, pruning real data from narrowband components and *strong* glitches, leaves a *residual* noise floor which is found to be Gaussian (in the operational sense of passing successfully some statistical test of Gaussianity) on sufficiently *short* timescales (typically $\sim 1 sec$). On longer timescales, the residual noise floor displays variance fluctuations [1] , and has been accordingly described pictorially as an (adiabatically) *breathing* Gaussian noise [139].
This could be explained as due to *weak* undetectable glitches occurring at relatively *high* rates, such that $\gamma \gg 1$, originating a non-stationary Gaussian noise component, whose variance fluctuates adiabatically with the fluctuating glitch rate [40]. It is otherwise reasonable to figure out that external disturbances will produce glitches with all amplitudes.

Summing up, the noise corrupting the data streams of large baseline interferometric detectors of gravitational waves presently in operation is a stochastic process consisting of three additive terms:

$$n(t) = n_{NB}(t) + n_g(t) + n_{floor}(t), \tag{2.3}$$

representing a narrowband component $n_{NB}(t)$, a *strong* (detectable) glitch component $n_g(t)$, and a residual, compound Gaussian component $n_{floor}(t)$, respectively. Remarkably, *none* of these terms is described by a Gaussian stationary distribution, although the first and last term may in fact include such components, accounting respectively, for the Brownian excitation of the violin modes, and for the pure thermal stationary (Johnson) noise in the instrument.
While the first term is usually disposed of *prior* to data analysis, the *non-Gaussianity* of the remaining two terms should be properly gauged, and duly taken into account when designing and evaluating GW detection algorithms.

---

[1] Partial evidence suggests (R. Conte, "A SIRP model for LIGO Noise," (2008) PhD dissertation, University of Salerno, Italy) that such residual noise floor may be modeled as a compound-Gaussian spherically-invariant random process (see T. J. Barnard and D. D. Weiner, "Non-Gaussian Clutter Modeling with Generalized Spherically Invariant Random Vectors," IEEE Trans SP-44 (1996) 2384 and references therein).

2.3 A Physical Model for Glitch Noise

Equation (2.1), as written, is a pure phenomenological model of glitch noise. It can be endowed with physical content by noting that, according to accumulating evidence [50], glitches arise from random transient excitations hitting specific noise-susceptible detector subsystems, and reaching the data channel through a finite number (henceforth denoted by L) of possible pathways. Any pathway is characterized by some specific canonical response (transfer function), here denoted as $w_l(t)$, $l = 1, \ldots, L$. This picture is corroborated by the experimental finding that most glitches fall into a *limited* set of *typical* waveforms [131]. In this respect, important direct measurements of the transfer functions of pathways from identified vulnerable areas of the IFO to the photodetector are under way, through the injection of impulsive noise of different nature.

In the simplest case, each environmental disturbance (assumed impulsive in time, and localized in space) will enter the instrument at some time θ_k, with amplitude A_k, through a *single* (dominant) entry point. Hence, individual glitches in eq. (2.1) will consist of a *single* canonical response, viz.

$$\psi(t - t_k; \vec{a}_k) = A_k w_k(t - \theta_k), \tag{2.4}$$

where $t_k = \theta_k + \tau_k$, τ_k being the time the impulses takes to travel the path from the solicited subsystem to the photodetector, and w_k is the transfer function of this path selected from the set $\{w_1, w_2, \ldots, w_L\}$. A_k and θ_k can be modeled as random variables, whose distribution can be estimated from real data, as well as the probability of occurrence of each canonical response w_i, $i = 1, 2, \ldots, L$.

More generally, a single (localized) impulsive environmental disturbance may enter the instrument through *several* noise-susceptible entry points, with *different* couplings and propagation delays. In this case an individual glitch in eq. (2.1) would be a *cluster* of canonical response, viz.

$$\psi(t - t_k; \vec{a}_k) = \sum_{i=1}^{M} A_i^{(k)} w_i(t - \theta_i^{(k)}), \text{ where } \theta_i^{(k)} = t_k - \tau_i^{(k)}, \tag{2.5}$$

where $A_i^{(k)}$ and $\tau_i^{(k)}$ are the strength and the delay whereby the wideband environmental disturbance couples to $M \leq L$ *different* instrument's entry points. A cluster of canonical responses would be characterized by the fact that the $A_i^{(k)}$ and $\theta_i^{(k)}$ in (2.5) $i = 1, \ldots, M$ are statisticallly correlated, in view of the common source, and all the $\theta_i^{(k)}$ in (2.5) lie in an interval which is comparable to the maximum difference between the travel times from possible entry points to the photodetector [2] Glitches consisting of clustered canonical responses in real data could not be recognized by mere visual inspection. Prony [113] algorithm (or robust variants thereof [106]) or Independent Component Analysis [128] may be used to identify them, and resolve them into their canonical components.

One way to build a realistic noise simulator would consist in estimating the probability of observing all possible clustered M-tuples of canonical responses, and the *joint* probability distributions of the related amplitudes, and delays. This will yield setting up a Markov model of glitchy real data [38].

Here, however, we shall adopt a different approach, which starts from physical and statistical considerations, yielding ultimately an analytical tractable approximation of the noise first order distribution, which turns out to be adequate for the purpose of the present work.

The characteristic functions (CFs) of the glitch noise model (2.1) can be computed exactly up to any order [40]. The first order one can be written

$$F_g(\xi, t) = \sum_{K=0}^{\infty} \text{prob}\left\{K[T] = K\right\} F_g(\xi, t|K), \tag{2.6}$$

where $F_g\left(\xi, t|K\right)$ is the conditional characteristic function, given K glitches in the analysis window, viz.:

$$F_g(\xi, t|K) = E\left\{\exp\left[\imath\xi \sum_{k=1}^{K} \psi\left(t - t_k; \vec{a}_k\right)\right]\right\}. \tag{2.7}$$

The expectation in (2.7) is taken with respect to both the firing times, t_k, and the shape parameters, $\vec{a}_k$. The pertinent distributions being assumed as time-invariant in the analysis window, and independent for each glitch occurrence, eq. (2.7) and (2.6) become, respectively

$$F_g(\xi, t|K) = \mathcal{B}(t, \xi)^K, \tag{2.8}$$

and

$$F_g\left(\xi, t\right) = e^{-\overline{N}} \sum_{K=0}^{\infty} \frac{\overline{N}^K}{K!} \mathcal{B}(t, \xi)^K = \exp\left[\overline{N}\left(\mathcal{B}(t, \xi) - 1\right)\right], \tag{2.9}$$

where $\mathcal{B}(t, \xi) = E\left[e^{j\xi\psi(t - t_0; \vec{a})}\right]$ and $\overline{N} = \lambda T$. Adding a stationary Gaussian component of zero mean and variance σ_G^2, the total CF is given by the product of the two CFs, viz.

---

[2] In principle, an extension to the non linear case is possible using the Volterra series representation of nonlinear responses (see, e.g. *The Volterra and Wiener Theory of Nonlinear Systems*, Wiley Interscience, New York, 2004).

$$F_n(\xi,t) = F_g\left(\xi,t\right)\exp\left[-\frac{1}{2}\xi^2\sigma_G^2\right]. \tag{2.10}$$

From the characteristic function $F_g\left(\xi,t\right)$ it is straightforward to compute the moments of the process $\nu_g(t)$ in eq. (2.1):

$$\mu_g^{(Q)} = (-\imath)^Q \left.\frac{\partial^Q F_g\left(\xi,t\right)}{\partial\xi^Q}\right|_{\xi=0}, \tag{2.11}$$

which, for some finite value of Q, might be used to approximate the PDF of $\nu_g(t)$ through the Edgeworth expansion [91]. The first four moments are explicitly given by

$$\begin{gathered}
\mu_g^{(1)} = E[g(t)] = \overline{N}E[\psi(t-t_0;\vec{a})],\\
\mu_g^{(2)} = E[g(t)^2] = \overline{N}^2E^2[\psi(t-t_0;\vec{a})] + \overline{N}E[\psi^2(t-t_0;\vec{a})],\\
\mu_g^{(3)} = E[g(t)^3] = \overline{N}^3E^3[\psi(t-t_0;\vec{a})] + 3\overline{N}^2E[\psi^2(t-t_0;\vec{a})]E[\psi(t-t_0;\vec{a})] + \overline{N}E[\psi^3(t-t_0;\vec{a})],\\
\mu_g^{(4)} = E[g(t)^4] = \overline{N}^4E^4[\psi(t-t_0;\vec{a})] + 6\overline{N}^3E^2[\psi(t-t_0;\vec{a})]E[\psi^2(t-t_0;\vec{a})] + 3\overline{N}^2E^2[\psi^2(t-t_0;\vec{a})]+\\
+4\overline{N}^2E[\psi(t-t_0;\vec{a})]E[\psi^3(t-t_0;\vec{a})] + \overline{N}E[\psi^4(t-t_0;\vec{a})],
\end{gathered} \tag{2.12}$$

where, the expectations are taken with respect to both t_0 and $\vec{a}$. The correlation function of $\nu_g(t)$ is instead given by:

$$E\left[\nu_g(t_1)\nu_g(t_2)\right] = \overline{N}E\left[\psi(t_1-t_0;\vec{a})\psi(t_2-t_0;\vec{a})\right] + \overline{N}^2E\left[\psi(t_1-t_0;\vec{a})\right]E\left[\psi(t_2-t_0;\vec{a})\right], \tag{2.13}$$

Under the made assumptions, the moments in eqs. (2.12) are also time-independent, while the correlation function (2.13) depends on $|t_1-t_2|$.

The first-order probability density function (PDF) of the process $\nu_g(t)$ is obtained by $F_g(\xi,t)$ through the inverse Fourier transform, which is analytically unaffordable. In this respect, many techniques have been proposed in the Literature to find an accurate approximation of the generalized shot noise PDF, e.g. the Edgeworth series expansion [127], the saddle point approximation [26] or by numerical evaluation [107] of the related integral equation. Here, I approximate the first-order PDF of the process in (2.1) using a weighted sum of Gaussian PDFs, viz.

$$\widehat{f}_n(x) = \sum_{p=1}^{P} w_p N(x; \mu_p, \sigma_p^2), \tag{2.14}$$

where the weights $w_p \geq 0$, $\sum_{p=1}^{P} w_p = 1$, the expected values μ_p and the variances σ_p^2 of the single components have been determined by fitting the empirical distribution. An alternative to such a fitting is to match the first terms of a suitable expansion of the exact and the approximated characteristic functions, as in [153].
The density mixture in eq. (2.14) converge uniformly to any density function by letting the number of terms P increase and each elemental covariance approach the zero matrix [98]. Middleton in [41] adopted the same kind of approximation for the impulsive noise arising in the urban environment.

The approximant PDFs are obtained by generating long sets of impulsive data with a priori assigned glitch rate, and glitch waveform parameters' distributions and estimating the parameters through the Expectation-Maximization algorithm (see e.g. [32]). The optimal number of Gaussian components was found as the smallest one allowing to pass successfull the Kolmogorov-Smirnoff test [147] between the empirical and the approximant distributions. In this case, from 2 to 4 Gaussian PDFs were found to be sufficient to approximate the actual non-Gaussian noise PDF.

Although the noise PDF is dependent on the glitch waveforms, we can identify two key parameters on which the gross features of the PDF depend, i.e. i) the rate of occurrence of glitches times their expected duration, viz. $\gamma = \lambda\overline{\tau}$, and ii) the glitch maximum SNR with respect to the Gaussian floor, $SNR_{max}^{(g)}$. These are the key parameters to determine the weight of the glitchy component in the mixture, and the slope of the tails. These parameters are all we need to adopt a robust approach in writing the detection statistics (see Chapter 3). The first order PDF is, of course, not enough to characterize the impulsive glitch noise, since also higher order statistics would be required. However, as we shall see later, it is enough to derive a *better* (close-to-optimal) detection strategy.

2.4 Simulating Glitch Noise

When it comes to generating glitch noise instances, the $\psi(\cdot)$ waveform in (2.1) should be suitably chosen. The most salient feature of glitches is that of being waveforms with almost compact time-frequency support, as seen from their time-frequency representations. Such waveforms are called time-frequency *atoms* in the technical Literature [37]. In [118–120] we used, to model spurious glitches, the simplest (un-chirped) minimum-spread Gabor atom [37]

$$\psi(t-t_0;\vec{a}) = \psi(t-t_0;A_0,f_0,\phi_0,\sigma_t) = A_0 \sin\left[2\pi f_0(t-t_0)+\phi_0\right] e^{-(t-t_0)^2/\sigma_t^2}, \qquad (2.15)$$

known in the GW literature as Sine-Gaussians (SG). The choice of the SG dictionary is suggested by the fact that a wide variety of observed glitches in the data channel are well modeled as SG atoms [131], and is further motivated by its structural simplicity and its minimum timefrequency spread, ($\sigma_t \sigma_f = (4\pi)^{-1}$). These properties should likely permit to represent the instrumental transients in a close-to-optimal (i.e., minimally redundant) way (see, e.g., [100, 149]).

The shape parameters in this case include the glitch amplitude A_0, duration σ_t, center frequency f_0 and initial phase ϕ_0. Figure 1 shows the PDFs of the random process in eq. (2.1), obtained by fitting with the model (2.14) the empirical distribution of a set of simulated data having different values of the glitch firing rate λ and of the maximum amplitude G_M. The amplitude of each glitch is assumed as uniformly distributed in $[-G_M, G_M]$, where G_M is derived by setting a maximum value for the glitch SNR with respect to the Gaussian floor, $SNR^{(g)}_{max}$, the initial phase ϕ_0 as uniformly distributed in $[0,\ 2\pi]$, the center frequency f_0 is uniformly distributed in $[0, 1000] Hz$, and the duration has uniform distribution between zero and the length of the analysis window T.

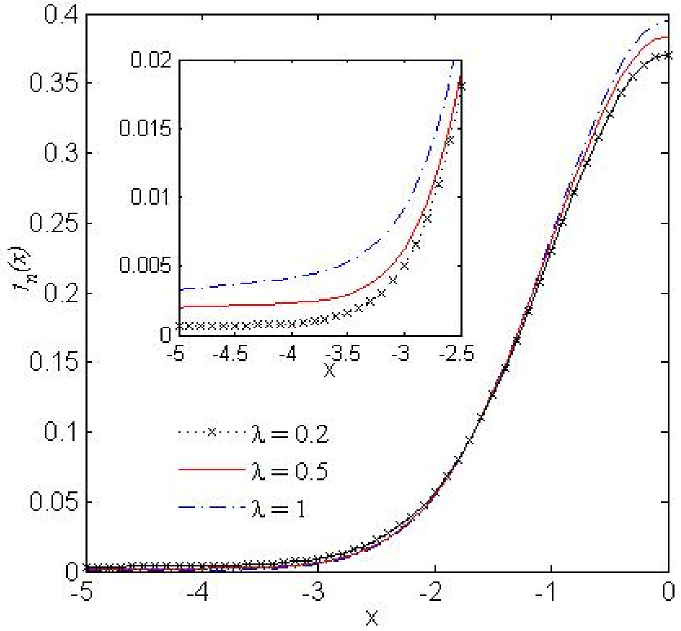

Figure 2.4: PDF of the glitch noise characterized by (2.10) using $\sigma_G = 1$ and SG glitches, fitted with the model in (2.14). Effect of the glitch rate λ on its shape.

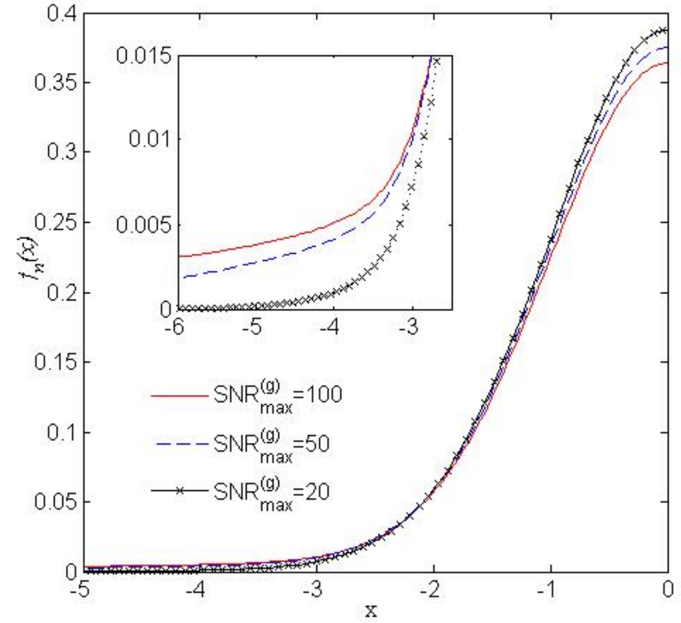

Figure 2.5: PDF of the glitch noise characterized by (2.10) using $\sigma_G = 1$ and SG glitches, fitted with the model in (2.14). Effect of the maximum glitch SNR, $SNR^{(g)}_{max}$ on its shape.

Chapter 3

Locally Optimum Network Detection of GW Bursts in Glitchy Noise

In this Chapter the detection of a special relevant class of GWs, GW Bursts, is discusses from first principles. GWBs are short transients of gravitational radiation emitted by violent astrophysical events, but limited or no information about the radiated waveform is available. Hence, multi-sensor detection based on different interferometers is in order, to achieve acceptable level of detection efficiency. As a step beyond the assumption that the corrupting noise is Gaussian, on which the currently implemented pipelines are based, I derive two detection statistics in non-Gaussian glitch noise, exploiting the *weak* GW amplitude assumption.

3.1 Locally Optimum Detection of Known GW Signals with Multiple Sensors

Detection of known signals with multiple sensors was originally developed in connection with radar surveillance, and is a well established topic in Signal Processing technical Literature. Two main muliple-sensor data analysis strategies can be envisaged, known as *distributed* and *centralized.* Several (e.g., tree or serial) *topologies* of distributed analysis exist (see [135] for a review), differing by the the extent to which local decisions at each sensor are taken and combined in order to construct a final decision rule. Conversely, in the centralized approach the data gathered from each sensor are sent to a central unit which merges them to form a *single* statistic, which is used to reach a global decision.

Incoherent GWB detection methods (see e.g. [55,64,80,104]) for detecting GWBs belong to this class. *Coherent* methods as proposed in [43,63,72,75,76,104,111,122,138,150] follow the centralized approach, which may be expected to attain better performance compared to the distributed one [56].

The possibility of operating the large-baseline optical interferometers presently in operation as a single GW observatory is of great importance in the perspective of GW astronomy, and is almost mandatory when it comes to the detection of unmodeled GW bursts in an impulsive (glitchy) noise background. The detection of a GW signal, using a network of D interferometers, can be formulated as a binary decision problem as follows,

$$\begin{cases} H_0: \ \mathbf{V}_d = \mathbf{n}_d \\ H_1: \ \mathbf{V}_d = \mathbf{S}_d + \mathbf{n}_d \end{cases}, \ d = 1, \ldots, D \tag{3.1}$$

where boldface denotes vectors of N_s time-samples taken from the corresponding continuos waveforms, e.g. $\mathbf{V}_d = \{V_{d1}, V_{d2}, \ldots, V_{dN_s}\}$, having defined $V_{dk} = V_d(t_k), \ k = 1, \ldots, N_s$. In (3.1) $\mathbf{n}_d$ is the additive noise corrupting the data at the output of detector-d and $\mathbf{S}_d$ is the GW signal received by the same detector.

For a plane gravitational wave with linearly polarized components $h_+(\vec{r}, t)$ and $h_\times(\vec{r}, t)$ impinging on Earth,

$$\mathbf{S}_d = F_d^+(\Omega_s)\mathbf{h}_d^+ + F_d^\times(\Omega_s)\mathbf{h}_d^\times, \ d = 1, \ldots, D \tag{3.2}$$

where $F_d^+(\Omega_s)$ and $F_d^\times(\Omega_s)$ are the *pattern functions* describing the directional response of detector-d (see e.g. [150]), Ω_s is the location of the emitting source on the celestial sphere, and $\mathbf{h}_d^{+,\times}$ are the time-sampled linearly polarized TT wave components at detector-d, whose position is denoted by $\vec{r}_d$.

The GW signals $\mathbf{h}_d^{+,\times}$, impinging on the interferometers, differ only by a time shift, depending on $\vec{r}_d$ and $\Omega_s = (\vartheta_d, \varphi_s)$[1]. In the following we restrict to the case of triggered detection, where the direction of arrival is fiducially known from different (e.g. radio) observations [2]. For this reason, for data analysis purposes the output of detector-d must be time-shifted by the (direction of arrival dependent) delay between the wavefront arrival times at $\vec{r}_d$ and $\vec{r} = 0$ (taken coincident with the Earth center), viz.,

$$\tau_d(\Omega_s) = c^{-1}\hat{n} \cdot \vec{r}_d, \tag{3.3}$$

where $\hat{n}$ is the unit wave vector and c the speed of light in vacuum. The noise process $\mathbf{n}_d$ affecting the output of detector d, is described by a generic multivariate distribution $f_{\mathbf{n}_d}(\cdot)$, representing the joint probability density function (PDF) of N_s noise time-samples. It is reasonable to assume the noise processes in the outputs of different detectors as independent, in view of the large separation among them. We further assume througout this Section that the noise process in any interferometer is stationary for the typical analysis windows we consider.

It is expedient to introduce a parameter $\theta \geq 0$ which measures the GW strength, by letting $\mathbf{S}_d = \theta\hat{\mathbf{S}}_d$ in (3.1), where $\hat{\mathbf{S}}_d$ denotes the unit norm *template* of the sought signal, which in this Section is supposed to be known in advance.

The optimum (in the Neyman-Pearson sense) decision rule for the problem in (3.1), if $\theta = \theta_0 > 0$ is given, is based on the Likelihood Ratio (henceforth LR) test statistic [96], viz.

$$\Lambda = \frac{\displaystyle\prod_{d=1}^{D} f_{\mathbf{n}}^{(d)}(\mathbf{V}_d - \theta_0\hat{\mathbf{S}}_d)}{\displaystyle\prod_{d=1}^{D} f_{\mathbf{n}}^{(d)}(\mathbf{V}_d)}. \tag{3.4}$$

In this Section it is further assumed that the noise time-samples at the output of any detector d are i.i.d.[3], so that $f_{\mathbf{n}}^{(d)}(\mathbf{V}_d) = \prod_{k=1}^{N_s} f_n^{(d)}(V_{dk})$, where $f_n^{(d)}(\cdot)$ denotes the PDF of a single noise sample in the detector d. Thus, taking the logarithm of the LR above, we get

---

[1] The angular coordinates (ϑ,φ) represent the polar and azimuthal angles in an Earth-centered coordinate system, where the polar axis points to the North Pole and $\varphi = 0$ identifies the Prime Meridian.

[2] In principle, if the DOA is unknown, (ϑ_d, φ_s) can be regarded as unknown parameters, to be estimated according to the maximum likelihood principle, by picking up the largest statistic among those corresponding to a suitable lattice of points in the (ϑ_d, φ_s) space. Setting up in an optimal manner such a lattice requires knowledge of the related ambiguity function, which is left for a a future paper.

[3] This assumption is removed in the next Section.

$$\lg \Lambda_{LR} = \sum_{d=1}^{D} \sum_{k=1}^{N_s} \left\{ \lg f_n^{(d)} \left[V_{dk} - \theta_0 S_{dk} \right] - \lg f_n^{(d)} \left[V_{dk} \right] \right\}. \tag{3.5}$$

It is well known that for the special case of Gaussian noise, a *uniformly most powerful* (UMP) hypotheses test, i.e. a test yielding the highest detection probability at a fixed false alarm probability, exists, for which the choice of the threshold is *independent* of the actual value of θ_0, provided $\theta_0 > 0$, and is given by the matched-filter statistic [96], viz.

$$\sum_{d=1}^{D} \frac{\mathbf{V}_d \cdot \hat{\mathbf{S}}_d^T}{\sigma_d^2} :: \eta \tag{3.6}$$

where σ_d^2 is the noise variance at interferometer d and the value of the threshold η depends only on the prescribed false-alarm probability.

On the other hand, for an arbitrary non-Gaussian noise, a UMP test does *not* exist in general. One possibility to overcome this difficulty, in the light of the least favorable case philosophy (see [96]), consistent with our expectations of dealing with weak GW signals, is to seek *local optimality* in a neighborhood of $\theta = 0$, by maximizing the *slope* of the test power at $\theta = 0$, for a given false alarm rate.

This results in the *locally* most powerful or *locally optimum* (LO) detection test [17]. As an additional benefit the LO detector features, usually, a reduced computational and implementation burden.

The locally optimum detector (henceforth LOD) for the problem (3.1) is given by [17]

$$\Lambda^{(LO)} = \sum_{k=1}^{N_s} \sum_{d=1}^{D} \frac{d}{d\theta} \lg f_n^{(d)}(V_{dk} - \theta S_{dk}) \bigg|_{\theta=0} = \sum_{k=1}^{N_s} \sum_{d=1}^{D} S_{dk} g_{LO}^{(d)}(V_{dk}), \tag{3.7}$$

where

$$g_{LO}^{(d)}(x) = -\frac{\partial}{\partial\theta} \lg f_n^{(d)}(\theta) \bigg|_{\theta=x} = -\frac{f_n'^{(d)}(x)}{f_n^{(d)}(x)} \tag{3.8}$$

is a nonlinear memoryless function dependent on the noise distribution. The LOD test turns out to be asymptotically optimal, when $N_s \to \infty$ and $\theta \to 0$ [17].

The statistic in (3.7) can be recognized as the first term in the Taylor expansion of the LR in (3.5) around the point $\theta = 0$, viz.

$$\lg \Lambda = \sum_{d=1}^{D} \sum_{q=1}^{\infty} \theta^q \frac{(-1)^q}{q!} \left[\sum_{k=1}^{N_s} S_{dk}^q \frac{d^q}{dx^q} \log f_n^{(d)}(x) \bigg|_{x=V_{dk}} \right], \tag{3.9}$$

admitting a simple interpretation of $\lg \Lambda$ as a linear superposition of an infinite number of linear correlators acting on suitable non-linear transformations of the data. In general, according to the LO approach one should use as a detection statistic the lowest-order non-vanishing term in the expansion above.

Accordingly, the LO statistic can be cast in the following simple form

$$\Lambda^{(LO)} = \sum_{d=1}^{D} \mathbf{g}_d[\mathbf{V}_d] \cdot \hat{\mathbf{S}}_d^T \tag{3.10}$$

where a superfix T denotes the transpose, and we used the shorthand

$$\mathbf{g}_d[\mathbf{V}_d] = \left\{ g_{LO}^{(d)}(V_{d1}), g_{LO}^{(d)}(V_{d2}), \ldots, g_{LO}^{(d)}(V_{dN_s}) \right\}. \tag{3.11}$$

The LOD in eq. (3.10) is the sum of the LODs corresponding to single-detector problems. In the case of Gaussian noise $g_{LO}^{(d)}(x) = x/\sigma_d^2$ and the LOD reduces to the statistic in eq. (3.6), which is obtained from the exact LR in eq. (3.5) by ignoring the second order term[4], i.e. the energy of the signal. Hence, in Gaussian noise case, if the sought signal has *a priori* known waveform (and energy), the LOD coincides with the exact LR statistic[5].

The LOD concept was introduced in the GW data analysis Literature, to the best of our knowledge, by Creighton [36]. It was subsequently suggested by Anderson et al [54] in connection with excess-power based detection statistics, and eventually discussed in considerable depth by Allen et al. in [52, 53], where it was notably stressed that the same LOD structure is obtained within both a frequentist and a Bayesian framework.

Equation (3.10) is clearly reminiscent of the linear correlator (3.6) (which is the optimal detection statistic in Gaussian noise), except that in (3.10) the data are preliminarily filtered by the static nonlinearity (3.8). Loosely speaking, this latter acts by trimming off large data samples likely due to strong glitches, which make the noise PDF heavy tailed. In Figures 3.1-3.2 the functions $g_{LO}(x)$ obtained via (3.8) from the PDFs in Figure 2.4-2.5 are shown. It is seen that $g_{LO}(x)$ is linear in a neighbourhood of $x = 0$, outside of which it deviates significantly from the linear behaviour. The more the noise distribution departs from the Gaussian, i.e., the larger the glitch rate and/or the maximum glitch signal-to-noise ratio, the narrower this neighbourhood becomes.

---

[4] Higher order terms are zero for the Gaussian noise case.

[5] In this case the constant energy can be ignored and this is equivalent to a trivial shift in the threshold to which the statistic is compared for the detection.

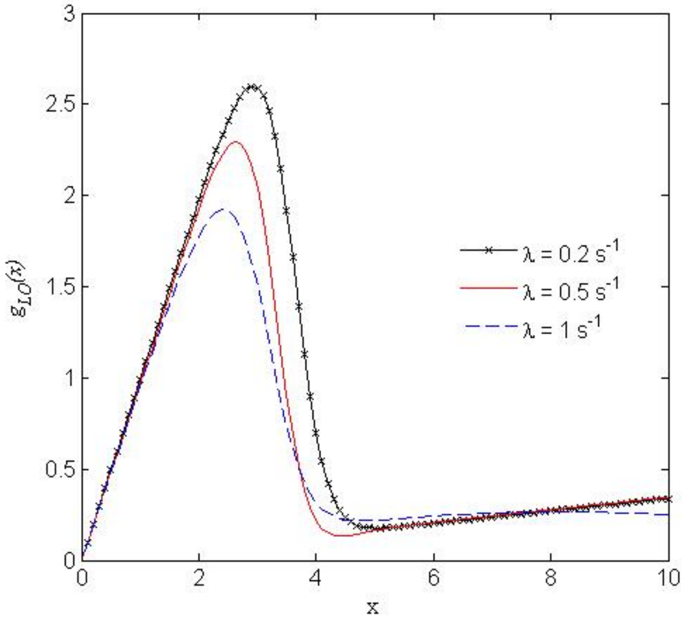

Figure 3.1: g_{LO} function obtained through eq. (3.8) for the PDFs in Figure 2.4. Effect of the glitch rate λ on its shape.

3.2 Locally Optimum Detection of Unmodeled GW Bursts with Multiple Sensors

I focuse on the detection of a special class of GW signals, i.e. GW Bursts (GWBs), characterized by short time duration ($\leq 1s$) and relativey high energy ($\approx 10^{-21}$). GWBs are a paradigm of signals for which the knowledge about the generating astrophysical events and the expected waveforms is very poor. As we anticipated in Section 1.5, GWBs are emitted from relatively frequent violent astrophysical events, including supernova explosions, mergers of binary systems, gamma ray bursters etc.

In principle we could capitalize on *a priori* available information about the sought GWB waveforms coming from general-relativistic numerical simulations of collapsing/exploding systems [44, 83, 136, 144], to construct signal templates to be used in (3.10). However the available numerically computed waveforms are difficult to parameterize in a physically meaningful fashion, and apply only to a few *specific* classes of sources, so that their use as templates would yield poor detection efficiency. Therefore, it might make more sense to assume that *no information at all* concerning the sought waveforms is available, and to seek detection schemes which may work well irrespective of the shape of the sought signal. Under this perspective, two basic approaches seem possible: a) estimating from the data themselves a

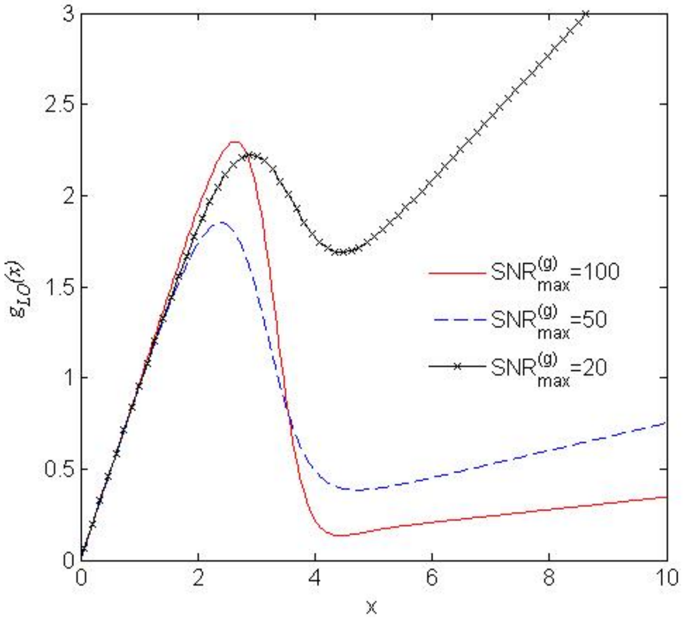

Figure 3.2: g_{LO} function obtained through eq. (3.8) for the PDFs in Figure 2.4. Effect of the maximum glitch SNR, $SNR^{(g)}_{max}$, on its shape.

suitable set of parameters, describing uniquely the signal; b) using a *random* model for the signal.

In the next two Subsections both approaches will be explored.

3.2.1 GWBs as Unknown Deterministic Signals

Under the assumption of no available a priori information, a possible set of parameters describing uniquely the GWB signal are the very time samples of its polarization components, i.e. $\left\{h_k^+, h_k^\times\right\}$, $\forall k = 1, \ldots, N_s$. This choice became known as the standard likelihood approach in the GW data analysis Literature [75], and can be traced back to Flanagan and Hughes [46]. For an observational window including N_s time samples from D detectors, there are accordingly $2 \cdot N_s$ unknowns to be estimated from $D \cdot N_s$ time samples. Under the accepted assumptions, it is readily seen that the estimation problem *breaks* up into N_s (structurally identical) uncoupled problems, each yielding 2 unknowns (h_k^+ and $h_k^\times$) from D data ($V_{dk},\ d = 1, 2, \ldots, D$). The following remark is in order here. The *Maximum Likelihood* estimator is *asymptotically* optimal (in the Cramer-Rao sense [96]) when the number of data goes to infinity. In our case the number of data is D, which is only a few units. We may thus expect a poor performance of the standard likelihood estimator. Note that this applies

both the Gaussian and the non-Gaussian noise case.
On the other hand, if we had a model (even a phenomenological one) for the sought GWBs using only a *finite* number P of parameters (e.g., the principal components, as in [136]), we would face the problem of retrieving P unknowns from $D \cdot N_s$ time samples[6]. The estimate would be accordingly accurate for N_s large enough, being asymptotically optimal for $N_s \to \infty$, at the expense of being most likely workable only numerically.

Letting $\mathbf{H} = \{\mathbf{h}^+, \mathbf{h}^\times\}$ the vector of unknown GW time samples (at $\vec{r} = 0$), the ML estimator maximizes the conditional PDF of the data $f(\mathbf{x}|\mathbf{H})$ over the space where $\mathbf{H}$ is supposed to lie, $\mathbf{x}$ being the actual realization of the noisy data stream. The coordinates, $\widehat{\mathbf{H}}_{ML}$, of the supremum of the likelihood ratio in the parameter space provide our estimate of the signal parameters, and the supremum itself is used as a detection statistic. In the Signal processing literature this is known as a (*Generalized Likelihood Ratio Test* (GLRT) [96]). The ML estimator of $\mathbf{H}$, under the made assumption of i.i.d. noise samples, is accordingly given by

$$\begin{aligned} \widehat{\mathbf{H}}_{ML} = \overset{argmax}{\mathbf{H}} \prod_{d=1}^{D} \prod_{k=1}^{N_s} f_{\mathbf{n}}^{(d)} \left(V_{dk} - S_{dk}\right) = \\ \overset{argmin}{\mathbf{H}} \sum_{d=1}^{D} \sum_{k=1}^{N_s} - \lg f_n^{(d)} \left(V_{dk} - S_{dk}\right), \end{aligned} \tag{3.12}$$

where $S_{dk} = F_d^+ h_k^+ + F_d^\times h_k^\times$.

For Gaussian noise, $\widehat{\mathbf{H}}_{ML}$ is obtained by minimizing the following quantity

---

[6] A lower bound for P for GWB waveforms of a given class could be obtained from the related information (Shannon) dimension. This can be obtained from numerical simulations pertaining to specific source classes by using a well known property of quasi-bandlimited functions (D. Slepian, "On Bandwidth," Proc. IEEE **64** (1976) 292) Given the waveforms $\{S_p\}$, this amounts to computing

$$\sup_p \epsilon_p(B), \;\; \epsilon_p(B) = \left|\left| S_k(t) - S_k^{(B)}(t) \right|\right|$$

where

$$S_p^{(B)}(t) = \mathcal{F}^{-1}\left[\Pi_B(f) \mathcal{F} S_k(t)\right]$$

where $||\cdot||$ is the L^2 norm on the finite time-support T_S of the $\{S_p\}$ family, $\mathcal{F}$ is the Fourier transform operator, and $\Pi_B(f)$ is the unit spectral window with support $(-B, B)$. The function $\epsilon_p(B)$ typically exhibits a steplike behaviour, with knee point at $B = B_p^*$, and decays *exponentially* in $B - B_p^*$ afterwards. The information dimension of S_p can be accordingly estimated by

$$N_p \sim 2 B_p^* T_S,$$

and $N_S = \sup_p N_p$ gives the estimate of the information dimension of the whole family of functions $\{S_p\}$.

$$\mathcal{R} = \sum_{k=1}^{N_s} \sum_{d=1}^{D} \frac{(V_{dk} - S_{dk})^2}{\sigma_d^2} \tag{3.13}$$

which is the sum of the σ_d^2-weighted squared residuals of the linear systems

$$\mathbf{V}_{(k)} = \mathbf{F}\mathbf{h}_{(k)},\ \forall k = 1, \ldots, N_s, \tag{3.14}$$

where

$$\mathbf{V}_{(k)} = (V_{1k}, V_{2k} \ldots V_{Dk})^T\,, \tag{3.15}$$

$$\mathbf{h}_{(k)} = \left(h_k^+, h_k^\times\right)^T, \tag{3.16}$$

and $\mathbf{F}$ is the $D \times 2$ *network response matrix*, defined as follows

$$\mathbf{F} = \begin{pmatrix} F_1^+ & F_1^\times \\ F_2^+ & F_2^\times \\ \ldots & \\ F_D^+ & F_D^\times \end{pmatrix}. \tag{3.17}$$

In this case, the ML estimator is the weighted LS solution of (3.14), viz.

$$\widehat{\mathbf{h}}_{(k)} = \left(\mathbf{F}^T \mathbf{\Sigma} \mathbf{F}\right)^{-1} \mathbf{F}^T \mathbf{\Sigma} \mathbf{V}_{(k)}, \forall k = 1, \ldots, N_s, \tag{3.18}$$

where $\mathbf{\Sigma}$ is the $D \times D$ diagonal matrix, whose non-zero elements are $\left\{\sigma_1^{-2}, \sigma_2^{-2}, \ldots, \sigma_D^{-2}\right\}$.

The ML estimator in (3.18), in Gaussian noise, is *unbiased* ; it is also efficient, in that it attains the Cramer-Rao lower bound for the covariance matrix, and it is the *Minimum Variance Unbiased* estimator [96].

If the noise is non-Gaussian, on the other hand, the rhs of eq. (3.12) yields a *different* (non quadratic) measure of the residual error of (3.14), whose minimization can be quite complicated. And indeed, in this case the accuracy of the LS solution (3.18) is too much sensitive to the tail behaviour in the noise PDF, to be useful even as an approximate solution. Several error metrics have been proposed for inverting over-determined linear systems like (3.14), for the case where the noise in the data is non-Gaussian, including absolute, truncated quadratic, and bisquared error metrics [79]. A general framework for constructing such error metrics, while taking into account possible ill-conditioning of the problem, has been discussed in [87], based on the minimization of the Kullback-Leibler distance (mutual information) between the actual and estimated data-generating noise distribution. In practical cases the actual non-Gaussian noise distribution will be only loosely specified, due, e.g., to non-stationarity in time, suggesting the use of *robust* estimators [101], which are not too much sensitive to uncertainty and/or variation of the noise PDF in a given class.

Hereafter, in order to have a manageable expression for the ML estimator, we shall exploit again the *weak* signal assumption. Expanding the logarithm of the LR up to second order we obtain[7]:

$$\begin{aligned}\lg\Lambda \approx & \sum_{k=1}^{N_s}\sum_{d=1}^{D} g_{LO}^{(d)}(V_{dk})\left(F_d^{+}h_k^{+}+F_d^{\times}h_k^{\times}\right)+\\ +&\sum_{k=1}^{N_s}\sum_{d=1}^{D}\frac{1}{2}\Gamma^{(d)}\left(V_{dk}\right)\left[\left(F_d^{+}h_k^{+}\right)^2+\left(F_d^{\times}h_k^{\times}\right)^2+2F_d^{+}F_d^{\times}h_k^{\times}h_k^{+}\right],\end{aligned} \tag{3.19}$$

where

$$\Gamma^{(d)}(x)=\frac{f_n''^{(d)}(x)}{f_n^{(d)}(x)}-\left(\frac{f^{(d)}{}'_n(x)}{f_n^{(d)}(x)}\right)^2. \tag{3.20}$$

Setting the partial derivatives of eq. (3.19) w.r.t. to the unknown h_k^{+} and $h_k^{\times}$, equal to zero, we obtain, a linear system whose solutions are

$$\left\{\begin{aligned}\widehat{h}_k^{+} &= \frac{\sum_{d=1}^{D} g_{LO}^{(d)}(V_{dk})\left(I_k^{+\times}F_d^{\times}-I_k^{\times\times}F_d^{+}\right)}{I_k^{++}I_k^{\times\times}-(I_k^{+\times})^2}\\ \\ \widehat{h}_k^{\times} &= \frac{\sum_{d=1}^{D} g_{LO}^{(d)}(V_{dk})\left(I_k^{+\times}F_d^{+}-I_k^{++}F_d^{\times}\right)}{I_k^{++}I_k^{\times\times}-(I_k^{+\times})^2}\end{aligned}\right. ,k=1,2,\ldots,N_s, \tag{3.21}$$

where

$$\begin{aligned}I_k^{++} &= \sum_{d=1}^{D}\Gamma^{(d)}(V_{dk})(F_d^{+})^2\\ I_k^{\times\times} &= \sum_{d=1}^{D}\Gamma^{(d)}(V_{dk})(F_d^{\times})^2\\ I_k^{+\times} &= \sum_{d=1}^{D}\Gamma^{(d)}(V_{dk})F_d^{+}F_d^{\times}\end{aligned}\quad . \tag{3.22}$$

Equations (3.21) represent the *Locally Optimum Estimator* (LOE, [33, 117]) of $\mathbf{h}_{(k)}$. It can be shown that if the number of data D in (3.21) goes to infinity and the GW amplitude

---

[7] We indeed maximize, for convenience, the ratio between the likelihood function and its value in the absence of the GW signal, which is the Likelihood Ratio.

go to zero as $\mathcal{O}(D^{-1/2})$, the LOE is asymptotically normal and efficient, in the Cramer-Rao sense [33, 78].
Eqs. (3.21) can be written as follows

$$\widehat{\mathbf{h}}_{(k)} = \left(\mathbf{F}^T \mathbf{\Sigma}_{(k)} \mathbf{F}\right)^{-1} \mathbf{F}^T \mathbf{g}_{(k)}, \;\; k = 1, \ldots, N_s. \tag{3.23}$$

where

$$\mathbf{g}_{(k)} = \left(g_{LO}^{(1)}(V_{1k}), g_{LO}^{(2)}(V_{2k}), \ldots, g_{LO}^{(D)}(V_{Dk}) \right)^T, \tag{3.24}$$

and $\mathbf{\Sigma}_{(k)}$ is a diagonal $D \times D$ matrix, whose non-zero elements are $\Sigma_{(k)}^{ii} = -\Gamma^{(i)}(V_{ik})$. Equation (3.23) shares the same structure as eq. (3.18), derived in the Gaussian noise case, except that the matrix $\mathbf{\Sigma}_{(k)}$ changes with the time sample k, and the output data are passed through the $g_{LO}^{(d)}(\cdot)$ functions. For Gaussian noise, $\Gamma^{(d)}(x) = -\sigma_d^{-2}$, and $g_{LO}^{(d)}(x) = x/\sigma_d^2$, so that eq. (3.23) gives back eq. (3.18). Also, in the Gaussian noise case, eq. (3.18) reduces to the Moore-Penrose pseudo-inverse matrix based solution [133], viz.

$$\widehat{\mathbf{h}}_{(k)} = \left(\overline{\mathbf{F}}^T \overline{\mathbf{F}} \right)^{-1} \overline{\mathbf{F}}^T \overline{\mathbf{V}}_{(k)}, \forall k = 1, \ldots, N_s, \tag{3.25}$$

where

$$\overline{\mathbf{V}}_{(k)} = \left(V_{1k}/\sigma_1, V_{2k}/\sigma_2 \ldots V_{Dk}/\sigma_D \right)^T,$$

$$\overline{\mathbf{F}} = \begin{pmatrix} F_1^+/\sigma_1 & F_1^\times/\sigma_1 \\ F_2^+/\sigma_2 & F_2^\times/\sigma_2 \\ \cdots & \\ F_D^+//\sigma_D & F_D^\times/\sigma_D \end{pmatrix}. \tag{3.26}$$

are the noise-weighted counterparts of eqs. (3.15) and (3.17).

In the non-Gaussian case, whenever the matrices $\Sigma_{(k)}$ are negative semi-definite, the estimator in eq. (3.23) minimizes a generalized weighted squared residual. We shall further discuss this point in Section 3.4.

Regularization

The network response matrix may be ill-conditioned in some regions of the celestial sphere [121], and the variance of the corresponding estimator of $\mathbf{h}$ can accordingly blow up dramatically. Under these circumstances, with reference to a general linear system

$$\mathbf{b} = \mathbf{\Xi} \mathbf{h}, \tag{3.27}$$

the noise $\delta\widehat{\mathbf{h}}$ in $\widehat{\mathbf{h}}$ can be larger than the noise $\delta\mathbf{b}$ in the data $\mathbf{b}$, and the following upper bound exists [57, 58]

$$\frac{\left\|\delta\widehat{\mathbf{h}}\right\|}{\left\|\widehat{\mathbf{h}}^{(0)}\right\|} \leq \text{cond}[\Xi]\frac{\|\delta\mathbf{b}\|}{\|\mathbf{b}^{(0)}\|} \tag{3.28}$$

where $\mathbf{b}^{(0)}$ and $\widehat{\mathbf{h}}^{(0)}$ are the noise-free data and reconstructed waveform, and $\text{cond}[\Xi] = \|\Xi\|\,\|\Xi^{-1}\|$ is the condition number of matrix Ξ. While this is only an upper bound, we see that even for mild ill-conditioning (i.e., $cond[\Xi] \sim 10$), waveform reconstruction via (3.18) can be badly inaccurate[8]. Several approaches have been proposed to mitigate this problem [75, 86]. In the simple regularization scheme á la Tikhonov, one minimizes the following quantity

$$\mathcal{R} + \gamma\mathbf{h}\boldsymbol{\Omega}\mathbf{h}^T. \tag{3.29}$$

where $\mathcal{R}$ is a general residual of the linear system in eq. (3.27), $\boldsymbol{\Omega}$ and γ are the so called regulator matrix and intensity, respectively. This approach results in adopting a *regularized* pseudo-inverse, such that

$$(\Xi)^{-1}_{reg} = \left(\Xi^T\boldsymbol{\Sigma}\Xi + \gamma\boldsymbol{\Omega}\right)^{-1}, \tag{3.30}$$

where $\boldsymbol{\Sigma}$ is a diagonal matrix defining the possible non-unitary weights of the squared residual.

In its eigenvector space $\Xi^T\boldsymbol{\Sigma}\Xi$ is

$$\begin{pmatrix} \mu_1 & 0 \\ 0 & \mu_2 \end{pmatrix} \tag{3.31}$$

where $\mu_{1,2}$ are the eigenvalues with $\mu_1 > \mu_2$. Ill-conditioning occurs because $\mu_2 \sim 0$. Rakhmanov in [121] proposed using regulator matrix, which, in the same vector space, can be written,

$$\begin{pmatrix} 0 & 0 \\ 0 & (\mu_2\mu_1)^{1/2} - \mu_1 \end{pmatrix} \tag{3.32}$$

and shew that a judicious choice of $\gamma \in [0, 1]$ can make the condition number of the r.h.s. of (3.30) as close to unity as desired. Obviously, some price is paid for, namely represented by a *bias* in the waveform estimate (see [121] for a discussion).

---

[8] As noted in [121], ill-conditioning will also amplify any error in the data due to inaccurate knowledge of the direction of arrival.

Using a regulator as in (3.30) in the estimator in eq. (3.23), and using the resulting estimate to compute the detection statistic (3.10), we obtain the locally optimum (LO) form of the generalized likelihood ratio test, GLRT, viz.

$$\mathrm{GLRT} = \sum_{k=1}^{N_s} \sum_{d,d'}^{1\ldots D} p_k^{dd'} g_{LO}^{(d)}(V_{dk}) g_{LO}^{(d')}(V_{d'k}), \tag{3.33}$$

where $p_k^{dd'}$ is the (d, d')-element of the $D \times D$ matrix $\mathbf{P}_k = \mathbf{F}\left(\mathbf{F}^T \boldsymbol{\Sigma}_{(k)} \mathbf{F}\right)^{-1} \mathbf{F}^T$.

The generalized likelihood ratio test if the noise is assumed to be Gaussian, GLRT_G, is obtained by using a regulator as in (3.30) in the estimator in eq. (3.18), and substituting the resulting estimate in the detection statistic (3.6).

3.2.2 GWB as a Random Signal

The complications affecting the estimation process discussed in Subsection 3.2.1, are substantially removed if the sought signals are modeled as *realizations* of a *random* processes. Adopting a maximum uncertainty attitude, it is natural to consider the two polarization components as independent random variables, having zero mean and impulsive auto-correlation, $\mathcal{R}_h(\tau) = \sigma_h^2 \delta(\tau)$. Under these assumptions, the locally optimum form of the LR statistic has been derived by Kassam (see Appendix A for details) and is

$$\Lambda^{(LO)} = \sum_{d=1}^{D} \sum_{k=1}^{N_s} \frac{f_n''^{(d)}(V_{dk})}{f_n^{(d)}(V_{dk})} + 2 \sum_{d=1}^{D} \sum_{p=d+1}^{D} \mathcal{R}_{dp} \mathbf{g}_d \left[\mathbf{V}_d\right] \cdot \mathbf{g}^p \left[\mathbf{V}_p\right]^T, \tag{3.34}$$

where

$$\mathcal{R}_{dp} = E[S_d S_p]. \tag{3.35}$$

The first term in (3.34) is a measure of the total *energy* in the data. The second term is a measure of the *correlation* between data from different detectors in the network, known as *Generalized Cross-Correlation* (henceforth GCC). The first term in eq. (3.34) may be large even if only *spurious* transients (glitches) are present in the data from *individual* interferometers. On the other hand, the GCC term accounts only for transients which overlap *consistently* to the assumption of having the same astrophisical origin. Therefore, following Kassam, it is reasonable to drop the first term in (3.34) and retain only the GCC term, as a detection statistic.

The coefficient $\mathcal{R}_{dp}$ in (3.36) is explicitly given by:

$$\mathcal{R}_{dq} = E[h_+^2] F_d^+ F_q^+ + E[h_\times^2] F_d^\times F_q^\times + E[h_+ h_\times] \left(F_d^+ F_q^\times + F_d^\times F_q^+ \right). \tag{3.36}$$

The expectations in (3.36) depend on the structure of the GWB source. Assuming h_+ and $h_\times$ as independent and identically distributed,

$$\mathcal{R}_{S_d S_p} = \left(F_d^+ F_p^+ + F_d^\times F_p^\times \right), \tag{3.37}$$

up to an irrelevant multiplying factor[9]. The GCC statistic can be accordingly written

$$\text{GCC} = \sum_{d=1}^{D} \sum_{p=d+1}^{D} \mathcal{R}_{dp} \mathbf{g}_d \left[\mathbf{V}_d \right] \cdot \mathbf{g}_p \left[\mathbf{V}_p \right]^T, \tag{3.38}$$

which sums the $D \cdot (D-1)$ cross-correlations between any couple of detectors, with proper weights.

Note that the structure of (3.38) is similar to (3.33), differing from this latter due to the absence of the *energy* terms ($d = p$), which are instead included in the GLRT statistic. Interestingly, the $\mathcal{R}_{S_d S_p}$ coefficients in (3.38) display a behaviour similar to that of the non-diagonal coefficients in (3.33), as functions of the source position on the celestial sphere, as will be shown in the last Section. For Gaussian noise (3.38) becomes a sum of linear correlators, LCC

$$\text{LCC} = \sum_{d=1}^{D} \sum_{p=d+1}^{D} \mathcal{R}_{dp} \frac{\mathbf{V}_d}{\sigma_d^2} \cdot \frac{\mathbf{V}_p}{\sigma_p^2}. \tag{3.39}$$

Computing the GCC statistic requires *no* inversion, and accordingly *no* ill-conditioning pathology may occur and needs to be taken into account. On the other hand, the GCC provides no information about the *shape* of the detected signal, and as such it qualifies for *pure* detection purposes only.

3.3 Locally Optimum Network Detection for Correlated Noise

In the previous Section I assumed that the noise in each detector consists of a white Gaussian process corrupted by a colored non-Gaussian (glitchy) component. Here we extend this derivation to the realistic case where the Gaussian components are colored as well.

---

[9] This factor is the variance σ_h^2 which is a constant and it does not affect the detection performance.

In general, there always exists a suitable linear transform of the data, yielding a set of uncorrelated samples; this is known as Karhunen-Loeve transform [96] (KLT). If the initial data are Gaussian distributed, the KLT yields a set of independent samples, and allows to factorize the joint PDF. On the contrary, in non-Gaussian distributed samples, non-correlation does not imply independence, so that the joint PDF cannot be factorized in principle. Nonetheless, we shall neglect correlations beyond the second order, assuming the data samples at the output of the KLT as being also independent. Under this assumption, all results in Section 3.2 still hold, in terms of the KLT-filtered data samples. This assumption was proposed and discussed by B. Allen in [52], who first introduced the LOD for the case of colored non-Gaussian noise in the GW technical Literature.

In the engineering technical Literature, it has been shown that in a variety of cases, this crude assumption still guarantees a sensible performance improvement compared to the plain Gaussian noise (no impulsive component) assumption (see e.g. [17]). The general problem of implementing an optimal detector structure in the case of colored non-Gaussian noise has been studied by several authors (see e.g. [47] or [148] and references therein). Under certain assumptions, it turned out that it is possible to keep the structure of this detector to be the same as for uncorrelated noise, varying only the non linearity applied to the data, or adding a correction term, depending not only on the first order but also on the higher order PDFs. We reserve for future work a deeper investigation about the optimal detector in dependent non-Gaussian noise samples, which will require a study of the correlation structure of the glitch noise, and about the benefit of using the Independent Component Analysis (ICA) [128] as a linear transform, to be used in place of the KLT, to provide a set of independent samples even in non-Gaussian noise.

The proposed simplified approach allows to modify at minimum existing pipelines implemented for the detection of GWBs, and the statistics for correlated time series are a straightforward generalization of those obtained in the previous Section.

3.3.1 The Known Signal Case

As often conveniently done, the KLT is approximated by the Discrete Fourier Transform (DFT) [124], which, for suitably long data sequences, gives an asymptotically diagonal correlation matrix whose non-zero elements are the coefficients of the PSD of the sequence.

Let $\mathbf{V}_d$ be the correlated output time series corresponding to interferometer-d, and $\mathbf{V}_{dk} = \left(\widetilde{V}^r_{dk}, \widetilde{V}^i_{dk}\right)$ the vector whose components are the real and imaginary part of the k-th complex DFT coefficient $\widetilde{V}_{dk}$, denoted by a superfix r and i, respectively, and assume similar definitions for $\mathbf{S}_{dk}$, $\mathbf{n}_{dk}$ and $\widetilde{S}_{dk}$, $\widetilde{n}_{dk}$. In the case of an *a priori* known signal, the

Likelihood Ratio can be approximated as follows

$$\Lambda = \frac{\prod_{d=1}^{D} f_{\mathbf{n}_d}\left(\mathbf{V}_d - \alpha \mathbf{S}_d\right)}{\prod_{d=1}^{D} f_{\mathbf{n}_d}\left(\mathbf{V}_d\right)} \approx \frac{\prod_{d=1}^{D} \prod_{k=1}^{N_b} f_{dk}\left(\widetilde{V}_{dk} - \alpha \widetilde{S}_{dk}\right)}{\prod_{d=1}^{D} \prod_{k=1}^{N_b} f_{dk}\left(\widetilde{V}_{dk}\right)}, \tag{3.40}$$

where $f_{dk}(\cdot)$ is the PDF of $\widetilde{n}_{dk}$, and N_b s the number of DFT coefficients. Note that in view of the symmetry properties of the DFT of real sequences, the number of independent frequency bins is $N_b = (N_s - 1)/2$ for odd N_s or $N_b = N_s/2 - 1$ for even N_s. $f_{dk}(Z)$ can be written as the product $p_{dk}(Z^r)p_{dk}(Z^i)$ of the two (identical) PDFs of the real and imaginary parts of the argument. Furthermore, we assume that the $f_{dk}(\cdot)$ are even functions[10]. To obtain the Locally Optimum Detection (LOD) statistic, the LR in eq. (3.40) must be expanded in Taylor series around the point $\alpha = 0$ up to the first order terms, yielding

$$\Lambda \approx \Lambda^{(LO)} = \sum_{k=1}^{N} \sum_{d=1}^{D} \mathbf{G}_{dk}(\mathbf{V}_{dk}) \cdot \mathbf{S}_{dk}^{T}, \tag{3.41}$$

where $\mathbf{G}_{dk}(\mathbf{Z})$, for $\mathbf{Z} = (Z^r, Z^i)$, is a vector defined as

$$\begin{aligned} \mathbf{G}_{dk}(\mathbf{Z}) = \left(-\frac{\partial_{Z^r} f_{dk}(\mathbf{Z})}{f_{dk}(\mathbf{Z})}, -\frac{\partial_{Z^i} f_{dk}(\mathbf{Z})}{f_{dk}(\mathbf{Z})} \right) = \\ \left(g_{dk}(Z^r),\ g_{dk}(Z^i) \right), \end{aligned} \tag{3.42}$$

where ∂ denotes the partial derivative, the prime denotes the full derivative and $g_{dk}(\cdot) = -p'_{dk}(\cdot)/p_{dk}(\cdot)$.

In the case of pure Gaussian noise, we have

$$\mathbf{G}_{dk}(\mathbf{Z}) = \left(Z^r/P_{dk},\ Z^i/P_{dk} \right), \tag{3.43}$$

P_{dk} being the PSD coefficient corresponding to the k-th frequency bin of the d-th antenna, so that eq. (3.41) becomes the matched filter statistic, viz.

$$\Lambda^{(LO)} = \sum_{d=1}^{D} \sum_{k=1}^{N_s} \left(\widetilde{S}_{dk}^{r} \frac{\widetilde{V}_{dk}^{r}}{P_{dk}} + \widetilde{S}_{dk}^{i} \frac{\widetilde{V}_{dk}^{i}}{P_{dk}} \right). \tag{3.44}$$

---

[10] This is reasonable if we assume that the first order PDFs of noise time samples are zero-mean even functions. This entails the evenness also for the PDF of any Fourier coefficient, which results from the convolution of N zero mean even PDFs.

3.3.2 GWBs as Unknown Deterministic Signals

The discussion about the ML estimator in Section 3.2.1 applies to this case as well. Hence, the weak signal assumption yields the LOE, which is obtained by maximizing only the first two terms of the LR, viz.

$$\lg\Lambda \approx \sum_{k=1}^{N}\sum_{d=1}^{D} \mathbf{G}_{dk}(\mathbf{V}_{dk})\cdot\mathbf{S}_{dk}^{T} + \frac{1}{2}\mathbf{S}_{dk}^{T}\mathbf{H}_{dk}(\mathbf{V}_{dk})\mathbf{S}_{d} =$$

$$\sum_{k=1}^{N}\sum_{d=1}^{D}\mathbf{G}_{dk}(\mathbf{V}_{dk})\cdot\mathbf{F}_{d}\widetilde{\mathbf{h}}_{k} + \frac{1}{2}\widetilde{\mathbf{h}}_{k}^{T}\mathbf{F}_{d}^{T}\mathbf{H}_{dk}(\mathbf{V}_{dk})\mathbf{F}_{d}\widetilde{\mathbf{h}}_{k}, \tag{3.45}$$

where, in the second equation, I used $\mathbf{S}_{dk} = \mathbf{F}_{d}\widetilde{\mathbf{h}}_{k}$, obtained by eq. (3.2), which is also valid in the frequency domain, and

$$\mathbf{H}_{dk}(\mathbf{Z}) = \begin{pmatrix} \frac{\partial_{Z^r Z^r} f_{dk}(\mathbf{Z})}{f_{dk}(\mathbf{Z})} - \left(\frac{\partial_{Z^r Z^r} f_{dk}(\mathbf{Z})}{f_{dk}(\mathbf{Z})}\right)^2 & \frac{\partial_{Z^r Z^i} f_{dk}(\mathbf{Z})}{f_{dk}(\mathbf{Z})} - \frac{\partial_{Z^r} f_{dk}(\mathbf{Z})\partial_{Z^i} f_{dk}(\mathbf{Z})}{f_{dk}(\mathbf{Z})^2} \\ \\ \frac{\partial_{Z^r Z^i} f_{dk}(\mathbf{Z})}{f_{dk}(\mathbf{Z})} - \frac{\partial_{Z^r} f_{dk}(\mathbf{Z})\partial_{Z^i} f_{dk}(\mathbf{Z})}{f_{dk}(\mathbf{Z})^2} & \frac{\partial_{Z^i Z^i} f_{dk}(\mathbf{Z})}{f_{dk}(\mathbf{Z})} - \left(\frac{\partial_{Z^i} f_{dk}(\mathbf{Z})}{f_{dk}(\mathbf{Z})}\right)^2 \\ \\ \end{pmatrix}, \tag{3.46}$$

$$\mathbf{F}_{d} = \begin{pmatrix} F_d^{+} & F_d^{\times} & 0 & 0 \\ 0 & 0 & F_d^{+} & F_d^{\times} \end{pmatrix}, \tag{3.47}$$

$$\widetilde{\mathbf{h}}_{k} = \begin{pmatrix} \Re\widetilde{h}_k^{+} \\ \Re\widetilde{h}^{\times} \\ \Im\widetilde{h}^{+} \\ \Im\widetilde{h}^{\times} \end{pmatrix}. \tag{3.48}$$

It is easy to show that the off-diagonal terms of the matrix $\mathbf{H}_{dk}(\mathbf{Z})$ are zero. Therefore, the r.h.s. of eq. (3.45) can be written as the sum of two terms, depending on the real and imaginary part of the GWB waveform separately, viz.

$$\Lambda \approx \Lambda_r + \Lambda_i, \tag{3.49}$$

where

$$\begin{gathered}
\Lambda_r = \sum_{k=1}^{N_b} \sum_{d=1}^{D} g_{dk}(\widetilde{V}_{dk}^r)(F_d^+ \, \Re\widetilde{h}_k^+ + F_d^\times \, \Re\widetilde{h}_k^\times)+ \\
\frac{1}{2}\sum_{k=1}^{N_s} \sum_{d=1}^{D} \Gamma_{dk}(\widetilde{V}_{dk}^r) \left[(F_d^+ \, \Re\widetilde{h}_k^+)^2 + (F_d^\times \, \Re\widetilde{h}_k^\times)^2 + 2F_d^+ F_d^\times \, \Re\widetilde{h}_k^+ \, \Re\widetilde{h}_k^\times\right], \\
, \\
\Lambda_i = \sum_{k=1}^{N_b} \sum_{d=1}^{D} g_{dk}(\widetilde{V}_{dk}^i)(F_d^+ \, \Im\widetilde{h}_k^+ + F_d^\times \, \Im\widetilde{h}_k^\times)+ \\
\frac{1}{2}\sum_{k=1}^{N_s} \sum_{d=1}^{D} \Gamma_{dk}(\widetilde{V}_{dk}^i) \left[(F_d^+ \, \Im\widetilde{h}_k^+)^2 + (F_d^\times \, \Im\widetilde{h}_k^\times)^2 + 2F_d^+ F_d^\times \, \Im\widetilde{h}_k^+ \, \Im\widetilde{h}_k^\times\right]
\end{gathered} \tag{3.50}$$

and $\left\{\Gamma_{dk}(\widetilde{V}_{dk}^r), \Gamma_{dk}(\widetilde{V}_{dk}^i)\right\}$ are the diagonal terms of the matrix $\mathbf{H}_{dk}(\widetilde{\mathbf{V}}_{dk})$, viz.

$$\Gamma_{dk}(V_{dk}^x) = \frac{\ddot{p}_{dk}(\widetilde{V}_{dk}^x)}{p_{dk}(\widetilde{V}_{dk}^x)} - \left(\frac{\dot{p}_{dk}(\widetilde{V}_{dk}^x)}{p_{dk}(\widetilde{V}_{dk}^x)}\right)^2, \ x = r, i. \tag{3.51}$$

Hence, the quantity in eq. (3.45) is maximized if Λ_r and Λ_i, are maximized with respect to $\mathbf{h}_k^r = \left(\Re\widetilde{h}_k^+, \Re\widetilde{h}_k^\times\right)^T$ and $\mathbf{h}_k^i = \left(\Im\widetilde{h}_k^+, \Im\widetilde{h}_k^\times\right)^T$, respectively. Λ_r and Λ_i are structurally identical to each other and to eq. (3.19), which is maximized by the solution in eq. (3.23). Accordingly, eq. (3.49) is maximized by

$$\begin{gathered}
\hat{\mathbf{h}}_k^r = \left(\mathbf{F}^T \mathbf{\Sigma}_{(k)}^r \mathbf{F}\right)^{-1} \mathbf{F}^T \widetilde{\mathbf{G}}_{(k)}^r, \\
, \ k = 1, \ldots, N_s. \\
\hat{\mathbf{h}}_k^i = \left(\mathbf{F}^T \mathbf{\Sigma}_{(k)}^i \mathbf{F}\right)^{-1} \mathbf{F}^T \widetilde{\mathbf{G}}_{(k)}^i,
\end{gathered} \tag{3.52}$$

where $\mathbf{F}$ is the network response matrix defined in eq. (3.17),

$$\widetilde{\mathbf{G}}_{(k)}^x = \begin{pmatrix} g_{1k}(\widetilde{V}_{1k}^x) \\ g_{2k}(\widetilde{V}_{2k}^x) \\ \cdots \\ g_{Dk}(\widetilde{V}_{Dk}^x) \end{pmatrix}, \ x = r, i, \tag{3.53}$$

and $\mathbf{\Sigma}_{(k)}^x$ is a diagonal $D \times D$ matrix, whose non-zero elements are $\Big\{\Gamma_{1k}(\widetilde{V}_{dk}^x), \Gamma_{2k}(\widetilde{V}_{dk}^x), \ldots,$ $\ldots, \Gamma_{Dk}(\widetilde{V}_{dk}^x)\Big\}$, $x = r, i$.

The Tikhonov regularization scheme can further be used to mitigate the ill-conditioning of the problem, in the same way as described in the previous Section. However, the expression of the LOE allows to adopt any other scheme of regularization as in the case of Gaussian noise, which will affect the computation of the inverse matrix in eq. (3.52).

3.3.3 The Random Signal Case

Alternatively as in Section 3.2.2 approach we can model the unknown GWB polarization waveforms as two independent and identically distributed random processes, with zero mean and flat PSD with level P_h, according to the maximum uncertainty approach.

Under the weak signal assumption, we expand the LR up to second order as in eq. (3.45), where now the signal $\mathbf{S}_{dk}$ is considered a random process. Λ is a random process as well, whose expected value is evaluated and considered as a detection statistic [17, 96]. The first order term vanishes due to the zero mean assumption; the second order term consists of two addends, one depending on the energies of single antennas, which is ignored as in Section 3.2.2, and an other one, depending on the cross-correlations between different antennas' outputs, which is used as detection statistic, i.e. *Generalized Cross-Correlation* (GCC). The procedure described in Appendix A can be easily extended to the present case, yielding the following detection GCC statistics

$$\mathrm{GCC} = \sum_{k=1}^{N_b} \sum_{d=1}^{D} \sum_{q>d}^{D} \mathbf{G}(\mathbf{V}_{dk}) E\left[\mathbf{S}_d \mathbf{S}_q^T\right] \mathbf{G}(\mathbf{V}_q)^T, \tag{3.54}$$

where the expectation $E[\cdot]$ is done w.r.t. the random GW amplitude. Eq. (3.54) is in accordance with the locally optimum statistic for stochastic signals obtained by Allen in [52]. Writing explicitly eq. (3.54) yields

$$\begin{aligned} \mathrm{GCC} = \textstyle\sum_{k=1}^{N_b} \sum_{d=1}^{D} \sum_{q>d}^{D} \Bigg(& E[\widetilde{S}^r_{dk}\widetilde{S}^r_{qk}] \tfrac{\dot{p}_{dk}(\widetilde{V}^r_{dk})}{p_{dk}(\widetilde{V}^r_{dk})} \tfrac{\dot{p}_{qk}(\widetilde{V}^r_{pk})}{p_{qk}(\widetilde{V}^r_{qk})} + \\ & + E[\widetilde{S}^r_{dk}\widetilde{S}^i_{qk}] \tfrac{\dot{p}_{dk}(\widetilde{V}^r_{dk})}{h_{dk}(\widetilde{V}^r_{dk})} \tfrac{\dot{p}_{qk}(\widetilde{V}^i_{qk})}{p_{qk}(\widetilde{V}^i_{qk})} + E[\widetilde{S}^i_{dk}\widetilde{S}^r_{qk}] \tfrac{\dot{p}_{dk}(\widetilde{V}^i_{dk})}{p_{dk}(\widetilde{V}^i_{dk})} \tfrac{\dot{p}_{qk}(\widetilde{V}^r_{qk})}{p_{qk}(\widetilde{V}^r_{qk})} + \\ & + E[\widetilde{S}^i_{dk}\widetilde{S}^i_{qk}] \tfrac{\dot{p}_{dk}(\widetilde{V}^i_{dk})}{p_{dk}(\widetilde{V}^i_{dk})} \tfrac{\dot{p}_{qk}(\widetilde{V}^i_{qk})}{p_{qk}(\widetilde{V}^i_{qk})} \Bigg). \end{aligned} \tag{3.55}$$

Under the made assumptions on the random GW amplitude, we obtain that

$$\begin{aligned} E[\widetilde{S}^r_{dk}\widetilde{S}^r_{pk}] = E[\widetilde{S}^i_{dk}\widetilde{S}^i_{pk}] = \mathcal{R}_{dp} = P_h \left(F_d^+ F_p^+ + F_d^\times F_p^\times\right), \\ E[\widetilde{S}^r_{dk}\widetilde{S}^i_{pk}] = E[\widetilde{S}^i_{dk}\widetilde{S}^r_{pk}] = 0. \end{aligned} \tag{3.56}$$

We note that the two statistics obtained in this Section, i.e. the GLRT, eq. (3.41) using eq. (3.52), and the GCC, eq. (3.54), are the sum of the statistics derived in the previous Section, applied to the real and imaginary parts separately. This is an obvious consequence of the independence of the real and imaginary parts of the GWB signal.

3.4 Robust and Nonparametric Implementation

In Sections 3.2 and 3.3 we derived the locally optimum GLRT and GCC detectors, assuming the PDF of the noise processes affecting the output of all antennas as *perfectly known* in writing the $g_{LO}(\cdot)$ and $\Gamma(\cdot)$ functions in eqs. (3.8) and (3.20) respectively.

Whenever the noise distributions are not fully known or are varying in time, a workable approach consists in identifying a functional class in which the noise distribution at any IFO lies and/or fluctuates, and adopting a detector which performs well over the whole class. Clearly, the coarser the knowledge about the noise, the wider the class where the noise will supposedly belong to.. Depending on how large the noise class is, it is expedient to distinguish *robust* form *nonparametric* detectors. *Robust* detectors are eligible when the noise distribution is known to belong to a relatively small functional neighborhood of a nominal PDF; in general, it is possible to compute a lower bound on performance in the specified class. *Nonparametric* detectors, on the other hand, perform well over a much broader class of noise distributions, exploiting *minimal* information about some gross features (e.g. zero median, symmetry, etc.) of the noise distribution. They are structurally very simple, being based on ranks and/or polarities of the observed data, and have the interesting property of constant false alarm rate over the whole class of PDFs, which allows to fix the detection threshold even if the actual noise distribution is unknown (see e.g. [18, 28]). Obviously, nonparametric detectors are expected to achieve worse perforomance than robust detectors.

In this Section, I propose simple robust and nonparametric implementations of the network detectors of unmodeled GWBs discussed in the previous Sections, identifying two functional classes where the IFOs' noise distributions can lie/fluctuate due to uncertainties and/or non-stationarities.

Let the noise distributions be symmetric, and consist of a Gaussian component contaminated by a generic non-Gaussian one, viz.

$$f_n(x) = (1-\epsilon) f_N(x) + \epsilon h(x) \tag{3.57}$$

where $f_N(x)$ is a (zero mean and σ_G^2 variance) Gaussian PDF, $h(\cdot)$ is a generic, symmetric non-Gaussian probability density and $\epsilon \in [0,1]$ is a mixture parameter. The noise PDF discussed in Chapter 2 can be recognized as a special case of (3.57), where

$$\epsilon = 1 - \exp(-\lambda T) \tag{3.58}$$

and (see eq. (2.9))

$$\epsilon h(x) = \mathcal{F}^{-1}\left\{\exp(-\lambda T)\left[\exp(\lambda T \mathcal{B}(\xi)) - 1\right]\right\} * f_N(x), \tag{3.59}$$

$\mathcal{F}$ being the Fourier transform operator, and $*$ denoting convolution.

Let the PDF class, spanned by the unknown/fluctuating non-Gaussian component, be denoted by $\mathcal{C}$.

The following general result due to Huber [101] can be used to implement a robust detector in C. The LOD computed for the particular noise distribution $\tilde{f}_n(x) \in \mathcal{C}$ which *minimizes* the Fisher information, defined as

$$\mathcal{I}[f_n] = \int_{-\infty}^{\infty} dx f_n(x) \left(\frac{f_n'(x)}{f_n(x)} \right)^2 , \tag{3.60}$$

has the property that its performance for *any* other $f_n \in \mathcal{C}$ will *not* be worse. The above criterion for building a robust detector is called *Min-Max*, and the related distribution $\tilde{f}_n$ is called the *least favourable* one in the class $\mathcal{C}$.

In [16] it is shown that the least favorable distribution in the class $\mathcal{C}$ has the following form

$$\widetilde{f}_n = (1-\epsilon) \frac{exp\left[-g(x)\right]}{\sigma_G\sqrt{2\pi}}, \tag{3.61}$$

where

$$g(x) = \begin{cases} \frac{x^2}{2\sigma_G^2}, \ |x| < K \\ \\ \frac{K|x|}{\sigma_G^2} - \frac{K^2}{2\sigma_G^2}, \ |x| \geq K \end{cases} . \tag{3.62}$$

The corresponding non-linearity computed, according to eq. (3.8), is the *Hard Limiter* (HL) function, viz.

$$g_{HL}(x) = \frac{1}{\sigma_G^2} \begin{cases} x, \ |x| \leq K \\ K\mathrm{sgn}(x), \ |x| > K \end{cases} . \tag{3.63}$$

In (3.63), sgn($\cdot$) is the Dirichlet signum function, and the parameter K is related to ϵ by [39]:

$$\int_{-K}^{K} f_N\left(x\right) dx + \frac{2\sigma_G^2}{K} \ f_N\left(K\right) = \frac{1}{1-\epsilon}, \tag{3.64}$$

which follows from the obvious unit area property of $\widetilde{f}_n$. Equations (3.64) and (3.58) can be combined to relate the parameter K in (3.63) to the glitch-rate λ as follows,

$$\int_{-K}^{K} f_N\left(x\right) dx + \frac{2\sigma_G^2}{K} \ f_N\left(K\right) = \exp(\lambda T). \tag{3.65}$$

Assume that the only time-varying and/or uncertain parameter affecting the noise distribution is the glitch firing rate λ, which may take values in some known range $[0, \lambda_{max}]$, all other parameters being constant and known. The least favourable PDF in this case is the one corresponding to the largest admissible glitch rate λ_{max}. Therefore, letting $\lambda = \lambda_{max}$ in (3.65) and solving for K, one obtains the Min-Max robust detector for the class of noise distributions (3.57), for which (3.65) holds.

The Min-Max *robust* implementation, over the broadest class of noises $\mathcal{C}$, of the detection statistics in eq. (3.33) and (3.38) are obtained by using the Hard-Limiter non-linearity in place of the $g_{LO}^{(d)}(\cdot)$ for any d.

For the least favorable distribution, $\widetilde{f}_n$ in eq. (3.61), the corresponding quantity $\Gamma(x)$, computed via eq. (3.20), is zero for $|x| \geq K$, and takes the constant value of $-1/\sigma_G^2$ for $|x| < K$, so that the waveform estimator eq. (3.23) belongs to the class of M-estimators introduced by Huber [101], minimizing a non-quadratic norm of the residual of the linear system (3.14).

In deriving a nonparametric detector, as a rather extreme case yielding a fiducially minimum performance detector, I may, e.g., give up any information about the noise PDF, except that it has zero median. In this case, the simplest nonparametric detector is based on sign coincidences of the output samples between different pairs of detectors, and in the statistics in eqs. (3.33) and (3.38) the signum function is used in place of the the $g_{LO}^{(d)}$ functions. The nonparametric GCC statistic is the generalization to the case of D detectors of the 2 detectors polarity coincidence statistic, which is known to be asymptotically optimal for double-exponential noise [17].

The noise PDF corresponding to the choice of the signum nonlinearity corresponds to the rather extreme case of Laplace (double exponential)-distributed noise. This is an unphysical case (infinite moments), for which $\Gamma(x)$ is identically zero. Hence, we may assume that $\Gamma^{(d)}(x)$, in this case, is a very *small* but *nonzero* constant for any d.

Remarkably, even the simplest nonparametric detector may outperform the linear correlator in simulated non-Gaussian noise. However, more sophisticated nonparametric detectors have been proposed for detection in non-Gaussian noise, which use nonlinear rank statistics (see e.g. [27]) and achieve better performance. Alternative nonparametric detectors are discussed in [125] based on nonparametric estimators [125] of the underlying noise distribution.

Chapter 4

Numerical Results

In this Chapter the detection performance of the statistics derived in Chapter 3 are evaluated on simulated and real instrumental (LIGO) noise. Numerical results show that the proposed statistics are effective in improving the detection efficiency compared to the Gaussian-noise tailored statistics, removing the need of additional checks and/or *ad hoc* vetoes. An existing implemented pipeline for the detection of GWBs has been accordingly modified, and the resulting boost in efficiency is a further proof of the goodness of the proposed approach.

4.1 Simulated Noise

The performance of the detection statistics derived in Chapter 3 is evaluated here in simulated glitchy noise, first, and in real LIGO noise, then. In this Section numerical results pertinent to simulated noise will be shown. In particular a Monte Carlo approach, by running 10000 noise realizations, has been adopted. For all cases the injected waveform is a Sine-Gaussian GWB, whose amplitude is gauged by the *intrinsic* quantity

$$\delta_h = \frac{2h_{rss}}{N} \tag{4.1}$$

where

$$h_{rss} = \left\{ \int \left[h_+^2(t) + h_\times^2(t) \right] dt \right\}^{1/2} \tag{4.2}$$

and N is the (two-sided) power spectral density of the white(ned) Gaussian component of the noise floor, supposed here to be equal in all antennas. Note that the SG shape does not affect the detector performance [118]. The actual SNR at the IFOs will be less than δ_h by a direction-of-arrival dependent factor given by the antenna directivity pattern.

The noise instances are generated using the model described in Section 2, going through the following steps: 1) fix the glitch rate λ, the glitch waveform (atom), and the probability distributions of the glitch shape parameters (amplitude, center frequency, duration, etc.); 2) fix the width T of the analysis window, and draw the number of glitches in it, according to the Poisson law with parameter λ; 3) generate the random glitch firing times t_k, uniformly distributed in T; 4) for each glitch draw the shape parameters values, using the chosen *a priori* distributions; 5) add white bandlimited Gaussian noise with fixed variance, chosen to be 1 for convenience. In all simulations we adopt the minimum-spread un-chirped Gabor (aka, Sine-Gaussian) atom to represent all glitches. The glitch amplitude distribution is assumed as uniform in $[-G_M, G_M]$, where G_M is the glitch amplitude corresponding to the maximum allowable glitch signal-to-noise ratio against the Gaussian floor, $SNR_{max}^{(g)}$. The distributions of center-frequency and duration estimated from (unclustered) triggers collected in 1 week of LIGO S5[1] data [34]. The distributions obtained for f_0 and σ_t are sketched in Figure 4.1.

The performance of all detectors discussed above is obviously dependent on the source location. Note that in view of the direction-dependence of the coefficients weighting the single terms in all considered detection statistics, i.e., eqs., (3.33), (3.38), even in the absence of a signal (H_0 hypothesis), the distribution of the statistics is direction-dependent, and hence

---

[1] S5 identifies the fifth science run (2005/2006) in which LIGO data were collected.

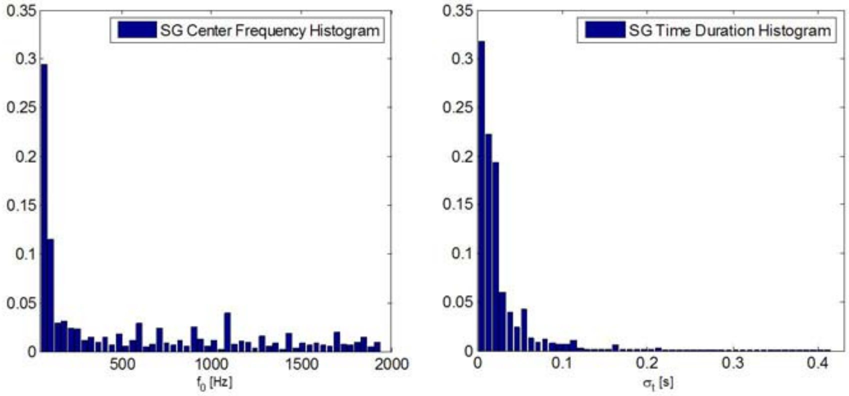

Figure 4.1: Empirical distributions of the center frequency and the time duration of events, detected by the Q-pipeline [34] during one week of LIGO S5 data.

the threshold corresponding to a fixed false alarm probability is *also* direction-dependent. For illustrative purposes, we shall draw the sky maps of the detection probability P_D, at the same false alarm level of 10^{-2}, for all proposed detectors. All sky maps are constructed by evaluating P_D over a grid of source positions $\Omega = (\varphi, \vartheta)$ in the celestial sphere, uniformly sampled in φ and $cos(\vartheta)$. Also, for all detectors we computed the Receiver Operating Characteristics (ROCs) displaying P_D versus P_{FA} for a fixed source position, corresponding to the maximum network sensitivity for both linear polarizations.

Note that, for sources located at or near the poles, i.e. at $\vartheta \approx 0, \pi$, the detector performance oscillates with φ. This is not surprising: the variation of φ produces a rotation of the (spherical) polarization basis $(\hat{u}_\vartheta, \hat{u}_\varphi)$, orthogonal to the wave propagation vector $\hat{u}_\rho$, which defines the wave polarization components (see e.g. [150]). As a result, the antenna patterns F^+ and $F^\times$ oscillate with φ, even in the limit $\vartheta \to 0, \pi$. For a source whose orientation is kept fixed, the wave polarization components would oscillate with φ as well, in such a way to make the signal at the output of the IFO independent from φ, in the limit $\vartheta \to 0, \pi$. Here, on the other hand, we keep the incoming wave (linear) polarization fixed, irrespective of the direction of arrival, which implies rotating the source accordingly, so that, when φ is varied in $[0, 2\pi]$, the GW signal keeps linearly polarized along the $+$ or $\times$ component. In this case, the signal received by an IFO changes as φ is varied, since the GW polarizations components remain constant by assumption, while the antenna patterns F^+ and $F^\times$ oscillate.

We start from the simplest ideal case of a pure Gaussian noise, where the glitch component is absent. In this case the optimal detection statistics are given by GLRT_G, obtained by using the estimator in eq. (3.18) in eq. (3.6), and LCC in eq. (3.39). The relevant sky maps are shown in Figures 4.2 and 4.3 for the $+$ and $\times$ polarizations, respectively, for $\delta_h = 20$.

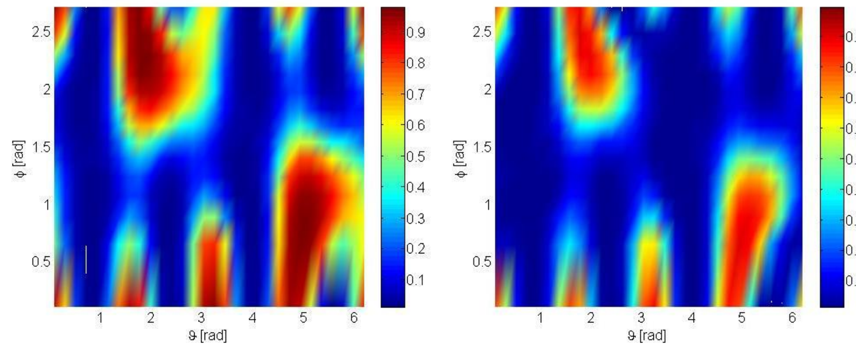

Figure 4.2: Sky maps of detection probability at false alarm level of 10^{-2}. Data corrupted by Gaussian noise. Left: Gaussian-noise version of generalized likelihood ratio, GLRT$_G$. Right: Gaussian-noise version of generalized cross-correlation detector, LCC eq. (3.39). Linearly (+)-polarized GWB, $\delta_h = 20$.

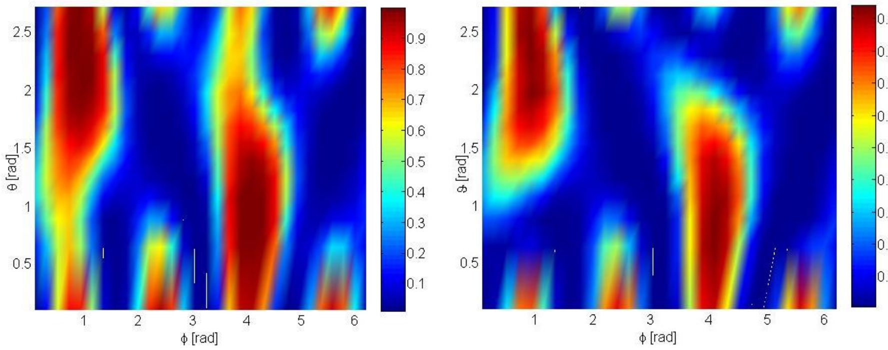

Figure 4.3: Sky maps of detection probability at false alarm level of 10^{-2}. Data corrupted by Gaussian noise. Left: Gaussian-noise version of generalized likelihood ratio, GLRT$_G$. Right: Gaussian-noise version of generalized cross-correlation detector, LCC eq. (3.39). Linearly ($\times$)-polarized GWB, $\delta_h = 20$.

The performance of the Gaussian noise tailored network detectors GLRT$_G$ and LCC is seriously spoiled after switching on the (non-Gaussian) glitch-noise component. This is illustrated in Figures 4.4 and 4.5, where $\delta_h = 20$, $\lambda = 0.5s^{-1}$, $SNR^{(g)}_{max} = 10^2$.

On the other hand, the locally optimum detectors GLRT and GCC, using the noise-tailored non-linearity defined in eq. (3.8) to pre-filter data, behave reasonably well, as shown in Figures 4.6 and 4.7.

The ROCs of the GLRT and GCC detectors in non-Gaussian noise are displayed in Figures 4.8 and 4.9 for the two linear polarizations, and compared to those of the Gaussian-noise tailored detectors GLRT$_G$ and LCC, both in Gaussian and non-Gaussian (glitchy) noise. Here $\delta_h = 20$, $\lambda = 0.5s^{-1}$, $SNR^{(g)}_{max} = 10^2$, and the source is located at a position corresponding to the best network performance, viz. $\{\vartheta = 2.28rad, \varphi = 1.99rad\}$ for the +

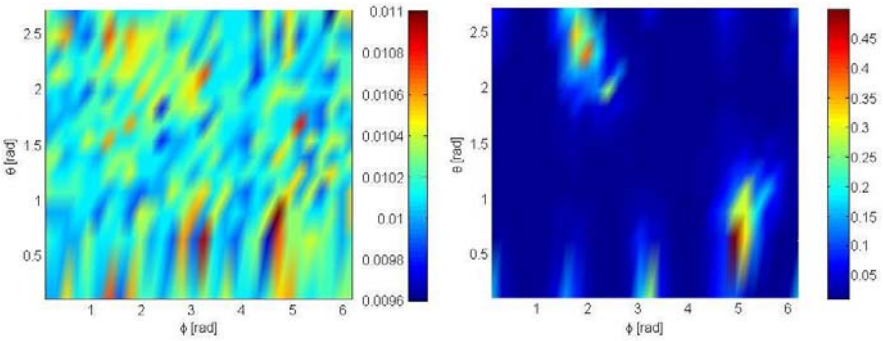

Figure 4.4: Sky maps of detection probability at false alarm level of 10^{-2}. Data corrupted by non-Gaussian noise, with $\lambda = 0.5s^{-1}$, $SNR^{(g)}_{max} = 100$. Left: Gaussian-noise version of generalized likelihood ratio, GLRT$_G$. Right: Gaussian-noise version of generalized cross-correlation detector, LCC eq. (3.39). Linearly (+)-polarized GWB, $\delta_h = 20$.

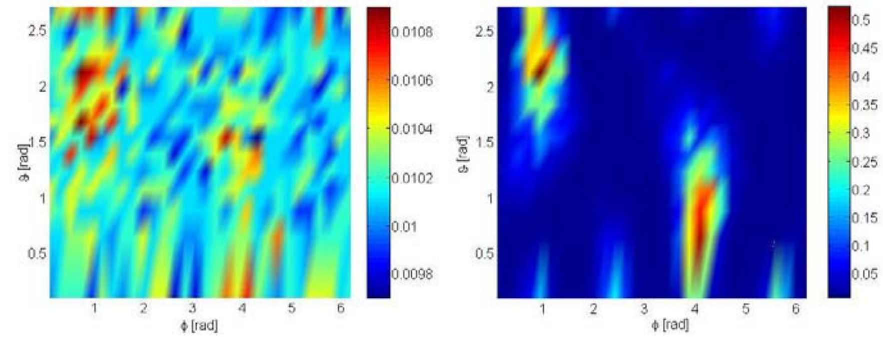

Figure 4.5: Sky maps of detection probability at false alarm level of 10^{-2}. Data corrupted by non-Gaussian noise, with $\lambda = 0.5s^{-1}$, $SNR^{(g)}_{max} = 100$. Left: Gaussian-noise version of generalized likelihood ratio, GLRT$_G$. Right: Gaussian-noise version of generalized cross-correlation detector, LCC eq. (3.39). Linearly (×-polarized GWB, $\delta_h = 20$.

polarization, and $\{\vartheta = 2.28rad, \varphi = 0.94rad\}$ for the × polarization.

Notably, in the small P_{FA} limit (below $P_{FA} \approx 10^{-2}$), the GCC offers the best performance. Only for false-alarm rates above $\sim 2 \cdot 10^{-2}$, the GLRT takes over. The GCC detector differs from the GLRT mainly due to the absence of the energy (auto-correlation) terms. Dropping these terms, the performance of the GLRT improves, becoming comparable to that of the GCC. Indeed, the sky maps of the coefficients $\mathcal{R}_{dd'}$ and $p_{dd'}$, $d \neq d'$, these latter computed using the matrix $\mathbf{\Sigma}$ in eq. (3.18), show a very similar behaviour, as shown in Figure 4.10.

Figures 4.11 and 4.12, show the influence of the glitch rate and the $SNR^{(g)}_{max}$ on the performance of the GLRT and GCC, respectively. Both detectors perform similarly, in this respect.

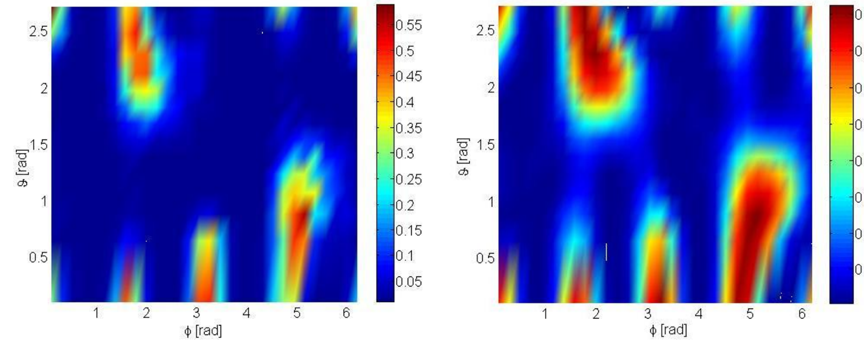

Figure 4.6: Sky maps of detection probability at false alarm level of 10^{-2}. Data corrupted by non-Gaussian noise, with $\lambda = 0.5 s^{-1}$, $SNR^{(g)}_{max} = 100$. Left: generalized likelihood ratio GLRT eq. (3.33). Right: generalized cross-correlation detector, GCC eq. (3.38). Linearly (+)-polarized GWB, $\delta_h = 20$.

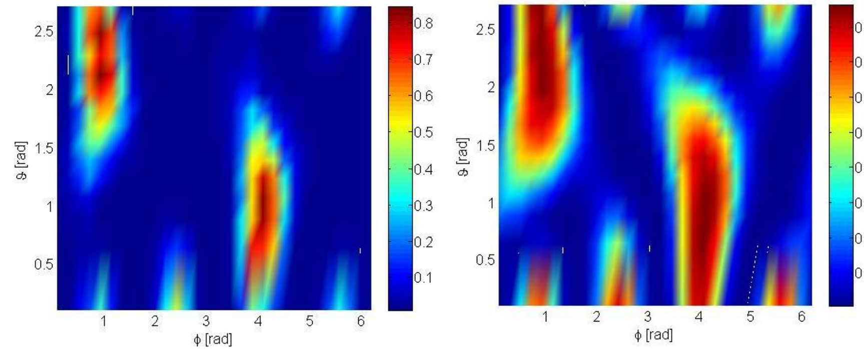

Figure 4.7: Sky maps of detection probability at false alarm level of 10^{-2}. Data corrupted by non-Gaussian noise, with $\lambda = 0.5 s^{-1}$, $SNR^{(g)}_{max} = 100$. Left: generalized likelihood ratio GLRT eq. (3.33). Right: generalized cross-correlation detector, GCC eq. (3.38). Linearly (×)-polarized GWB, $\delta_h = 20$.

Figure 4.13 and 4.14, on the other hand, displays the ROCs of the GLRT and GCC detectors for different values of δ_h (the intrinsic GWB strength), and fixed values of $\lambda = 0.5 s^{-1}$, $SNR^{(g)}_{max} = 10^2$, for linearly polarized radiation.

Overall, the GCC performs better than the GLRT in non-Gaussian glitchy noise, and has the advantage that it is not plagued by the ill-conditioning problem, providing no estimate of the possibly present GW signal. Figures 4.15 and 4.16 display the sky maps of the detection probability P_D, at a false alarm probability of 10^{-2} for the robust and non-parametric versions of the GCC, GCC_R and GCC_{NP}, respectively. Here again, $\delta_h = 20$, $\lambda = 0.5 s^{-1}$, $SNR^{(g)}_{max} = 10^2$, for both linear polarizations.

Finally, in Figures 4.17, the robust and non-parametric versions of the GCC are compared to the GCC in terms of ROCs, at fixed $\delta_h = 20$, $\lambda = 0.5 s^{-1}$, $SNR^{(g)}_{max} = 10^2$. The tradeoff

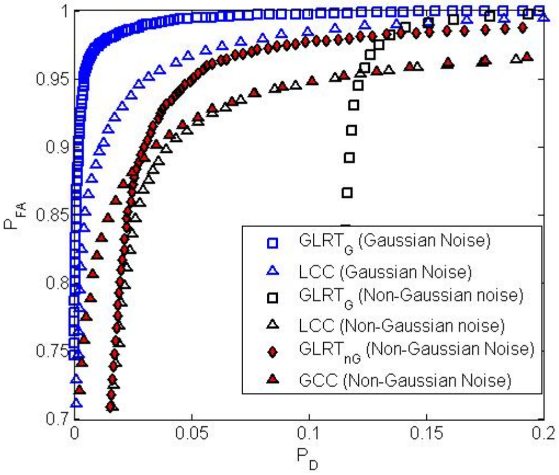

Figure 4.8: ROCs of the GLRT eq. (3.33) and GCC, eq. (3.38) in non Gaussian noise with $\lambda = 0.5s^{-1}$, $SNR^{(g)}_{max} = 10^2$ (red markers). ROCs of the Gaussian-noise versions GLRT$_G$, and LCC are also shown for comparison, both in (the same) non-Gaussian noise (black markers) and in Gaussian noise (blue markers). Linearly (+)-polarized GWB with $\delta_h = 20$ emitted by a source at ($\vartheta = 2.28$ rad, $\varphi = 1.99$ rad).

between the competing requirements for a detection statistic of applying to a broad noise class and yielding good performance is clearly illustrated. The robust implementation based on the Hard-Limiter non-linearity offers a good trade off between performance, and accuracy in the noise model. Heuristic prescriptions to fix the K parameter in the HL filter, e.g. setting K to 2 or 3 times the standard deviation of the Gaussian floor, have been also discussed in the pertinent Literature. The GCC$_{NP}$ offers a worse performance. It is worth reminding here that the GCC$_{NP}$ is optimal for the *broadest* class of noises with zero-median distribution, and otherwise unspecified. As such it stands as a lower performance bound, yet significantly better than the Gaussian-noise tailored detector.

4.2 Real LIGO S5 data

In this Section the proposed detection statistics are evaluated using a bunch of LIGO S5 data. In dealing with real data we need to adopt the statistics designed for colored noise in Section 3.3. In this case, one should estimate the PDFs of uncorrelated samples (DFT coeffcients), which in principle could be different, to derive the $g^{(d)}_{LO}$ and Γ^d functions. Although this is possible in principle [85], here I use a sub-optimum non-linearity, which is robust against variations/uncertainties of the actual PDFs, namely the hard-limiter (HL) function $g_{HL}(x)$ in eq. (3.63). The HL non-linearity is applied, as stated in Section 3.3, to the real and imaginary parts of the DFT coefficients, and the value of the breakpoint K is chosen to be

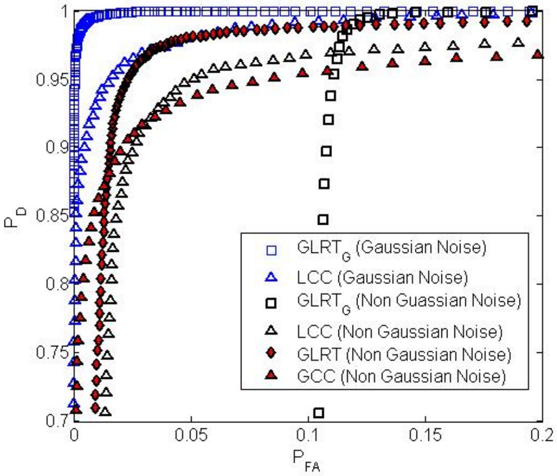

Figure 4.9: ROCs of the GLRT eq. (3.33) and GCC, eq. (3.38) in non Gaussian noise with $\lambda = 0.5s^{-1}$, $SNR^{(g)}_{max} = 10^2$ (red markers). ROCs of the Gaussian-noise versions GLRT$_G$, and LCC are also shown for comparison, both in (the same) non-Gaussian noise (black markers) and in Gaussian noise (blue markers). Linearly (×)-polarized GWB with $\delta_h = 20$ emitted by a source at ($\vartheta = 2.28$ rad, $\varphi = 0.94$ rad).

3 times the standard deviation of the noise in each spectral single bin.

I use a set of S5 data collected at the output of the three LIGO interferometers and inject linearly (+) polarized Sine-Gaussian bursts, whose energy is gauged by the quantity δ_h defined in eq. (4.1). Figure 4.18 shows the PSDs of the three IFOs for the considered data set.

For brevity, I show only the ROCs for one source position as in the previous Section. Figures 4.19 and 4.20 show the performances, respectively, for $\delta_h = 20$ and $\delta_h = 30$, evaluated on the chosen set of real data. For a better comparison, I plot the same ROCs, evaluated on simulated Gaussian noises, featuring the same PSDs as in Figure 4.18.

It is evident that in pure Gaussian noise the GLRT outperforms the LCC, both, as expected, achieving better performances than the corresponding statistics where the Hard-Limiter non-linearity has been applied. In real LIGO noise, on the contrary, the LCC and GCC outperform the GLRT statistics. This provides some evidence that the noise corrupting even "high" quality data behaves differently from a pure Gaussian noise.

As a next step, I added to both the simulated Gaussian and the real LIGO data sets, a glitchy component, as described in Chapter 2, injecting first weak and then loud glitches, having, respectively, $SNR^{(g)}_{max} = 30,\ 300$, with two values of the glitch rate $\lambda = 0.2,\ 1s^{-1}$.

Figure 4.21 shows the performances of the detection statistics when weak artificial glitches are added to the set of LIGO data, for two values of the firing rate. The maximum SNR for glitches is set equal to that of the injected GWB, the center frequency is uniformly distributed in the whole considered range, and the duration is uniformly distributed from zero and the length of the analysis window, viz. $0.5s$. In this case, the GCC achieves the best performance, which is comparable to that of the LCC for low glitch rate. Indeed, the noise is non-Gaussian but the glitch amplitude is slighlty larger than the floor level, hence, for low glitch rate, the effect of the Hard-Limiter non-linearity on the data is negligible.

If loud glitches are added, whose maximum SNR is one order of magnitude larger than that of the injected GWB, the performances of all detection statistics, plotted in Figure 4.22, deteriorate as expected, but the gain of the GCC w.r.t. the LCC increases. In this case, the benefit of the applied clipping is clearly evident.

The larger the expected number of glitchy samples in the analysis window γ, i.e. (see Chapter 2) the glitch rate times the expected glitch duration, and/or the larger the maximum glitch SNR, $SNR^{(g)}_{max}$, the more evident the gain in performance due to the clipping non-linearity. In the presence of loud and/or frequent glitches, the best statistic is the GCC. In the presence of weak rare glitches, GCC and LCC achieve comparable performance. It is important to note that the non-Gaussian tailored statistics, i.e. GLRT and GCC, are more robust with respect to glitches than the Gaussian tailored ones, i.e. GLRT_G and LCC, in the sense that an increase in the glitch rate and/or maximum glitch SNR spoils the performance of GLRT_G and LCC more than that of GLRT and GCC (see Figures 4.21,4.22).

The results obtained in this Section are in accordance with those obtained in simulated noise, shown in the previous Section.

4.3 The modified RIDGE pipeline

The GLRT and GCC statistics derived in Chapter 3 and tested in the previous Sections, have the same basic structure as the (Gaussian-noise tailored) statistics, on which currently implemented pipelines for the detection of unmodeled GWBs are based. The main clear difference is the presence of the non-linearity $g_{LO}(\cdot)$ clipping the data. This suggests that such pipelines could be improved, at the minimum effort, by applying a properly chosen non-linearity to the data before they are used to compute the detection statistics.

I implemented this modification in the RIDGE pipeline, developed by prof. S. Mohanty of University of Texas at Brownsville, where I spent six months supported by a *Fulbright* fellowship for Visiting Student Researcher. RIDGE pipeline is described in [72] and is based on the Standard Likelihood [43,75,121] to perform a *triggered* search of GWBs. The statistics RIDGE uses are the *Correlation Map* (CM) and the *Radial Distance* (RD), defined as follows [72]:

$$CM = \frac{max_{\Omega}\mathcal{L}(\Omega)}{min_{\Omega}\mathcal{L}(\Omega)} \tag{4.3}$$

and

$$RD = \left[\left(\frac{max_{\Omega}\mathcal{L}(\Omega)}{max_{\Omega}\overline{\mathcal{L}}_0(\Omega)} - 1\right)^2 + \left(CM\frac{min_{\Omega}\overline{\mathcal{L}}_0(\Omega)}{max_{\Omega}\overline{\mathcal{L}}_0(\Omega)} - 1\right)^2\right]^{-1/2}, \tag{4.4}$$

where $\mathcal{L}(\Omega)$ is the Likelihood statistic evaluated at source position Ω, and $\overline{\mathcal{L}(\Omega)}_0$ is the expected value of $\mathcal{L}(\Omega)$ in the H_0 (no GW signal) hypothesis. The modification I introduced consists in applying the g_{HL} non linearity (3.63) to the DFT samples of the data set, before computing the statistics (4.3) and (4.4). The breakpoint K is, as before, chosen to be 3 times the standard deviation of the noise affecting the DFT coefficients.
Figure 4.23 shows the ROC of the two statistics for the same LIGO S5 data set used in the previous Section, for $\delta_h = 30$, computed with and without the modification. "Modified" statistics are denoted with a subscript HL.

As before, I further tested the same statistics adding artificial glitches. For $\delta_h = 30$ we add weak glitches[2], whose maximum SNR is $SNR^{(g)}_{max} = 30$. The pertinent results are shown in Figure 4.24, from which it is clear that the application of the non-linearity entails a large improvement in the detection efficiency of the RIDGE pipeline.

In Figure 4.25 the performances of modified RIDGE statistics are compared with the GLRT and GCC.

---

[2] The addition of loud glitches deteriorates too much the performance of all the statistics.

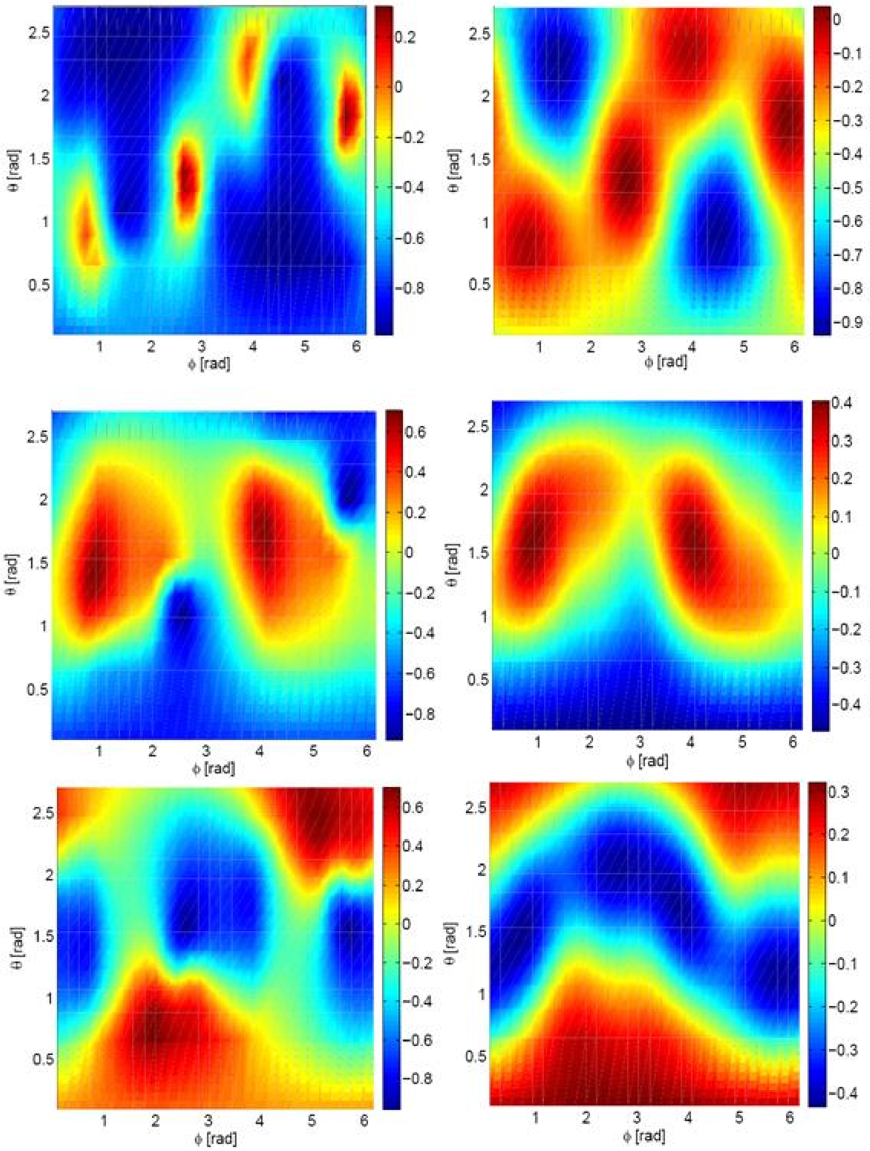

Figure 4.10: Sky maps of coefficients $p^{dd'}$, $d \neq d'$ in GLRT (left) and $\mathcal{R}_{dp}$ in GCC (right) corresponding to cross-correlation terms. First row: LHO-LLO; second row: LHO-Virgo; third row: LLO-Virgo.

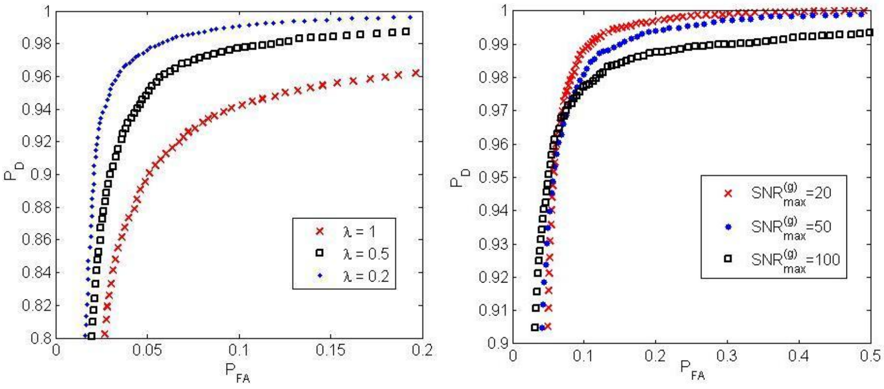

Figure 4.11: ROC of GLRT detector, eq. (3.33), for different values of the glitch rate, at fixed $SNR^{(g)}_{max} = 10^2$ (left), and for different values of $SNR^{(g)}_{max}$ at fixed λ=0.5 s-1 (right). Linearly (+)-polarized GWB with $\delta_h = 20$ emitted by a source at ($\vartheta = 2.28$ rad, $\varphi = 1.99$ rad).

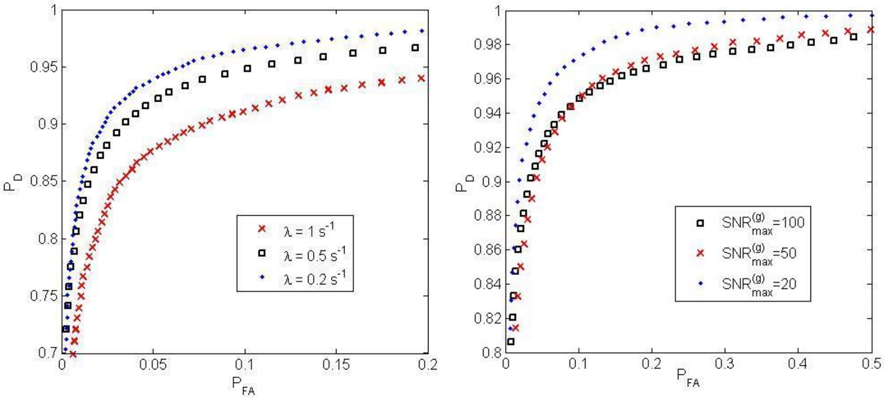

Figure 4.12: ROC of GCC detector, eq. (3.38), for different values of the glitch rate, at fixed $SNR^{(g)}_{max} = 10^2$ (left), and for different values of $SNR^{(g)}_{max}$ at fixed $\lambda = 0.5s^{-1}$ (right). Linearly (+)-polarized GWB with $\delta_h = 20$ emitted by a source at ($\vartheta = 2.28$ rad, $\varphi = 1.99$ rad).

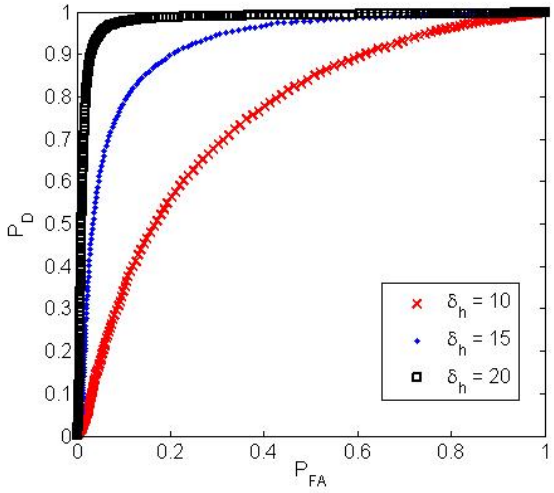

Figure 4.13: ROC of GLRT detector, eq. (3.33), for different values of the intrinsic SNR of the GWB, $\delta_h = 20$. Non-Gaussian noise with $\lambda = 0.5s^{-1}$ $SNR^{(g)}_{max} = 10^2$ (left). Linearly (+)-polarized GWB emitted by a source at ($\vartheta = 2.28$ rad, $\varphi = 1.99$ rad).

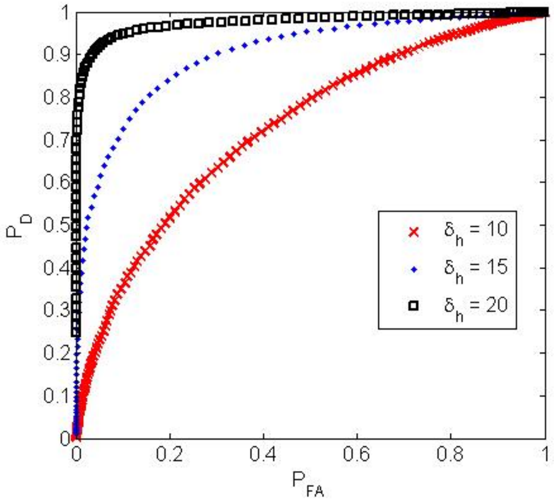

Figure 4.14: ROC of GCC detector, eq. (3.38), for different values of the intrinsic SNR of the GWB, $\delta_h = 20$. Non-Gaussian noise with $\lambda = 0.5s^{-1}$ $SNR^{(g)}_{max} = 10^2$ (left). Linearly (+)-polarized GWB emitted by a source at ($\vartheta = 2.28$ rad, $\varphi = 1.99$ rad).

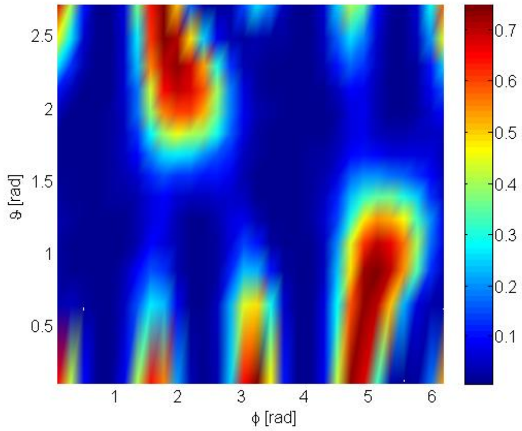

Figure 4.15: Sky map of detection probability at false alarm level of 10^{-2} of the robust version of GCC detector, GCC$_R$, based on the HL non-linearity. Data corrupted by non-Gaussian noise, with $\lambda = 0.5s^{-1}$, $SNR^{(g)}_{max} = 10^2$. Linearly (+)-polarized GWB, $\delta_h = 20$.

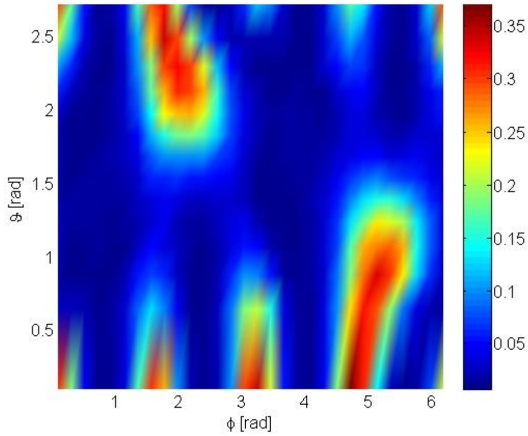

Figure 4.16: Sky map of detection probability at false alarm level of 10^{-2} of the nonparametric version of GCC detector, GCC$_{NP}$, based on the signum non-linearity. Data corrupted by non-Gaussian noise, with $\lambda = 0.5s^{-1}$, $SNR^{(g)}_{max} = 10^2$. Linearly (+)-polarized GWB, $\delta_h = 20$.

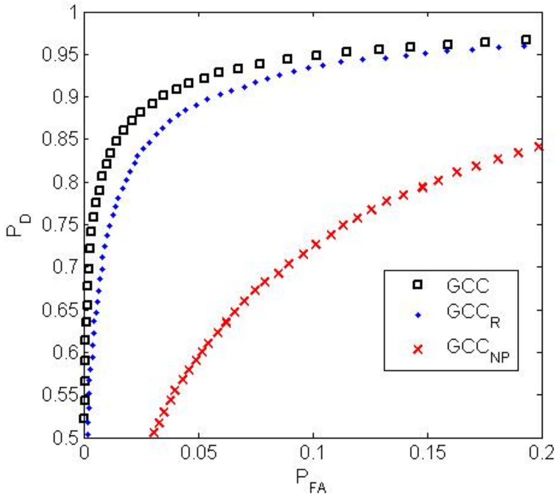

Figure 4.17: ROCs of GCC detector, eq. (3.38), vs its robust, GCC$_R$, and non-parametric, GCC$_{NP}$, versions. Non Gaussian noise with $\lambda = 0.5s^{-1}$, $SNR^{(g)}_{max} = 10^2$. Linearly (+)-polarized GWB with $\delta_h = 20$ emitted by a source at ($\vartheta = 2.28$ rad, $\varphi = 1.99$ rad).

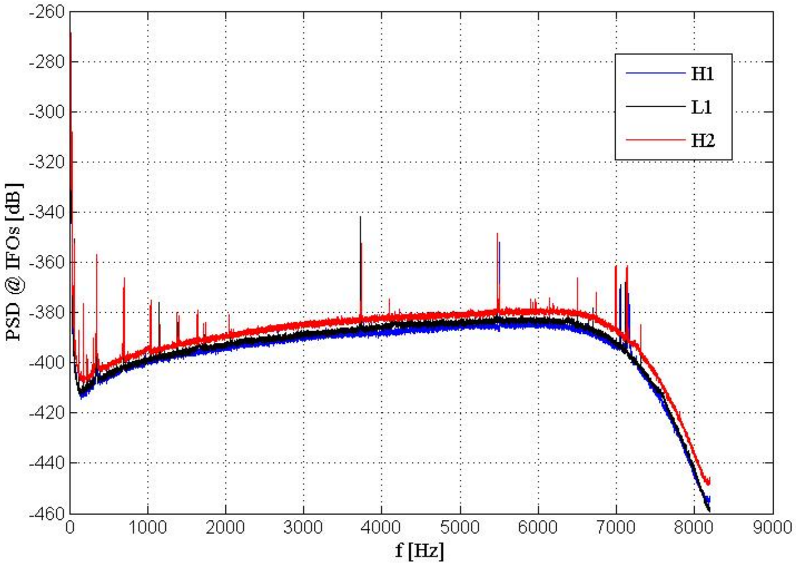

Figure 4.18: Power Spectral Density of the noises at the three LIGO IFOs for the analyzed set of data: the two IFOs at Hanford site (H1, H2), and the one at Livingston site (L1).

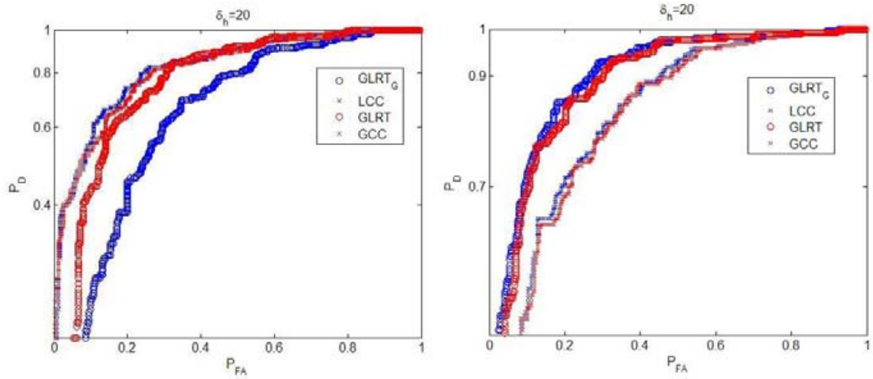

Figure 4.19: ROCs in real S5 data (left) and simulated colored Gaussian noise (right). (+)-polarized SG GWB, $\delta_h = 20$, emitted from a source at ($\vartheta = 2.28$ rad, $\varphi = 1.99$ rad).

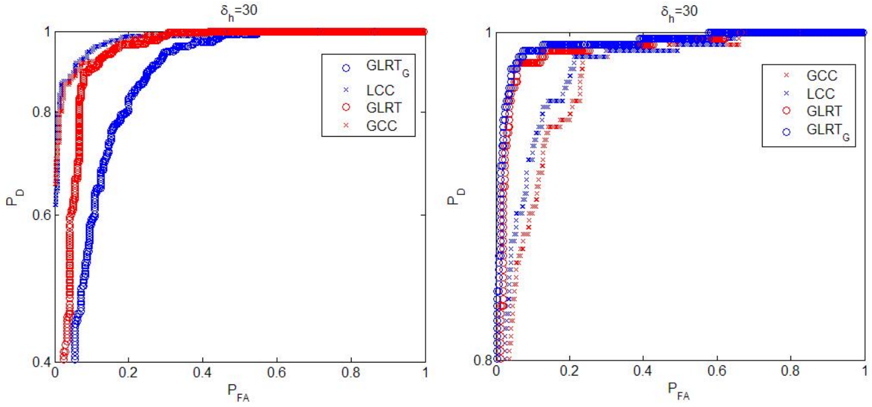

Figure 4.20: ROCs in real S5 data (left) and simulated colored Gaussian noise (right). (+)-polarized SG GWB, $\delta_h = 30$, emitted from a source at ($\vartheta = 2.28$ rad, $\varphi = 1.99$ rad).

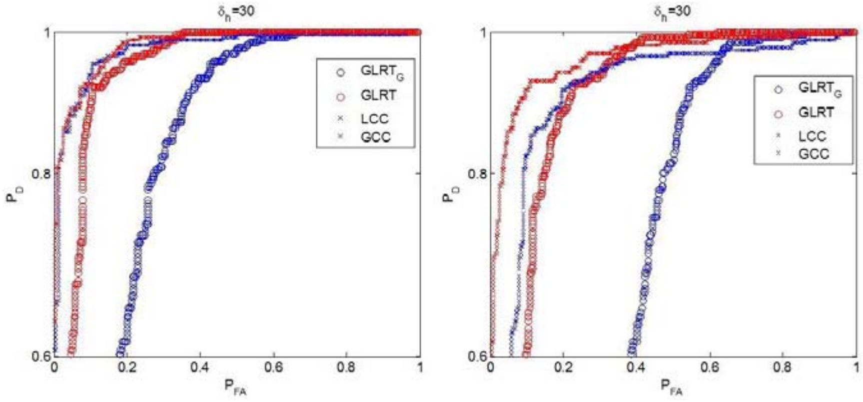

Figure 4.21: ROCs in real S5 data. Weak ($SNR^{(g)}_{max} = 30$) glitches added: $\lambda = 0.2s^{-1}$ (left) and $\lambda = 1s^{-1}$ (right). Linearly (+)-polarized SG GWB, $\delta_h = 30$, emitted from a source at ($\vartheta = 2.28$ rad, $\varphi = 1.99$ rad).

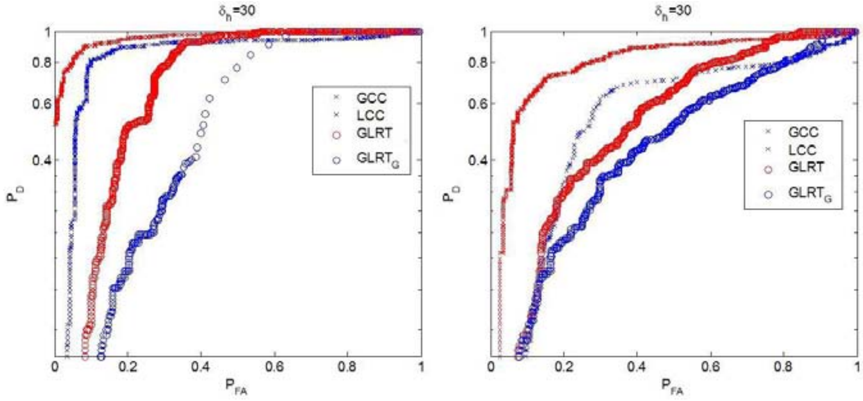

Figure 4.22: ROCs in real S5 data. Loud ($SNR^{(g)}_{max} = 300$) glitches added: $\lambda = 0.2s^{-1}$ (left) and $\lambda = 1s^{-1}$ (right). Linearly (+)-polarized SG GWB, $\delta_h = 30$, emitted from a source at ($\vartheta = 2.28$ rad, $\varphi = 1.99$ rad).

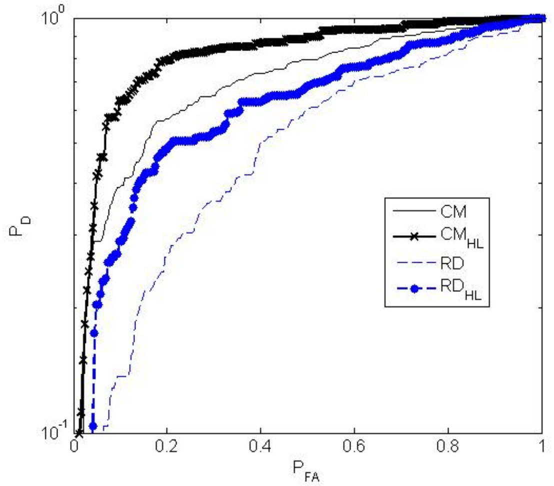

Figure 4.23: ROCs of the unmodified (no subscript) vs modified (subscript HL) RIDGE statistics in LIGO S5 data. Linearly (+)-polarized SG GWB, $\delta_h = 30$, emitted from a source at (ϑ=2.28 rad, $\varphi = 1.99$ rad).

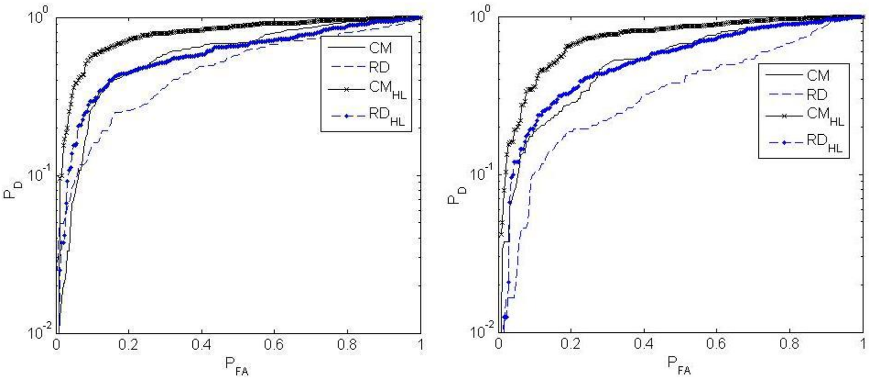

Figure 4.24: ROCs of the RIDGE statistics in real S5 data. Weak glitches added. Linearly (+)-polarized SG GWB, $\delta_h = 30$, emitted from a source at (ϑ=2.28 rad, φ=1.99 rad).

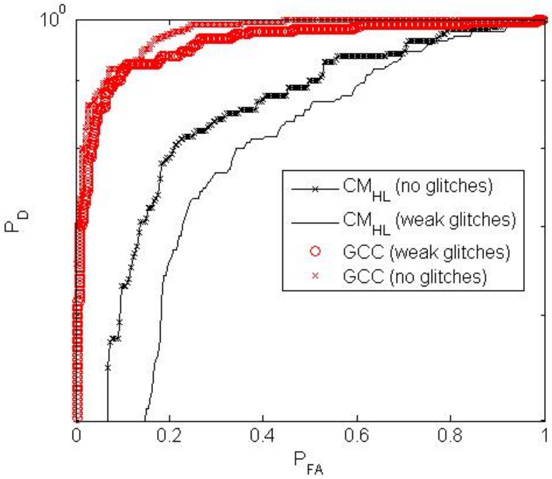

Figure 4.25: RIDGE statistics vs GCC in real S5 data. No Glitches and weak glitches ($SNR^{(g)}_{max} = 30$, $\lambda = 1s^{-1}$). Linearly (+)-polarized SG GWB, $\delta_h = 30$, emitted from a source at (ϑ=2.28 rad, φ=1.99 rad).

Chapter 5

Thermal Noise in Interferometers

In this Chapter I overview thermal noise theory, and describe the different components of thermal noise, connected to different mechanisms of dissipation, viz. the Brownian, the thermo-elastic and the thermo-refractive noises. Guidelines for the computation of such contributions for the mirror (test-mass) substrate and for a multilayer coating are provided as well.

5.1 Basics of Thermal Noise Theory

Thermal Noise (TN) in mirror test masses is expected to be the limiting noise contribution in the most sensitive bandwidth, i.e. between 40 Hz and few hundreds Hz, in advanced interferometric GW antennas, as shown in Figure 5.1.

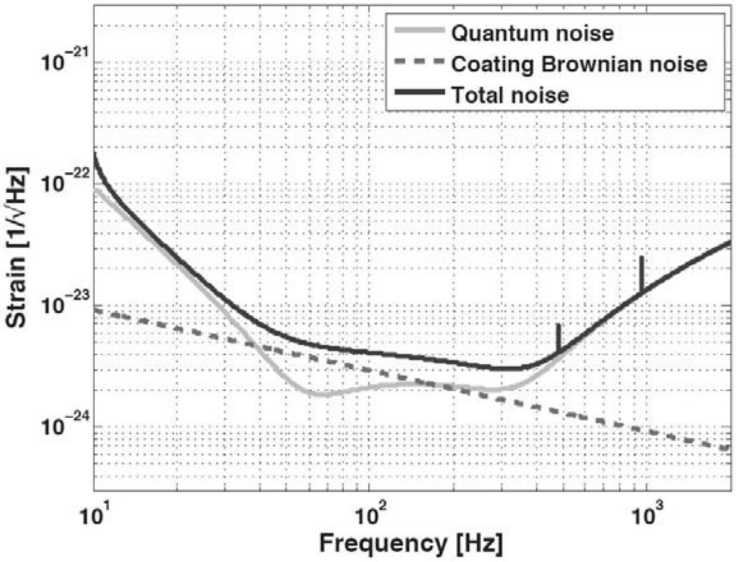

Figure 5.1: Projected noise floor of Advanced LIGO [97]. Brownian noise is limiting in the most sensitive frequency band.

We can identify two broad categories of thermal noise sources: i) *intrinsic* (dissipative) noise, arising when there is coupling of a mechanical motion to a heat reservoir, for which mechanical fluctuations are ruled by the Fluctuation-Dissipation theorem (to be stated below); ii) *extrinsic* (non-dissipative) noise, arising when externally imposed temperature variations (e.g. by heat absoprtion from the laser beam with fluctuating intensity [142]) drive thermal fluctuations. We focus here on the intrinsic noise, which is the major contribution to TN in the band of interest.

Intrinsic noise can arise in the thick transparent substrate of the IFO test masses, in the thin dielectric coating grown on top of this latter, or in their suspensions. If the mass suspensions are made by fused silica, as for Advanced LIGO (AdLIGO), their contribution to TN turns out to be negligible [12, 90]. TN fluctuations in the body of the mirror were first observed in [15, 29, 151]. The importance of the coating contribution to TN was realized by Levin in [151], and it has been throughly studied by several authors, in view of its importance for second generation of GW antennae (see e.g. [69, 70, 82, 108]). Coating TN arises from the fact that properties of the coating are quite different from those of the substrate[1], and the damping is not uniform in the entire test mass. Furthermore, while mirror substrates are carefully chosen for their low thermal noise (high mechanical Q-factor), mirror coating materials are chosen mostly for their optical properties (refraction index), and they do not have necessarily good mechanical properties. The coating on the surface of test masses is required in order to increase their reflectivity, which in turn increases the *finesse* of the Fabry-Perot cavities formed by the couple of mirrors placed in any interferometer arm.

Test masses for AdLIGO are made by a cylindrical substrate, with transverse diameter of about 30 cm, and thickness of about 20 cm. Preferred materials for the substrate are silica dioxide and sapphire; however the former offers a series of advantages over the latter. The coating is in general a multilayer dielectric structure, as it will be described in the next Chapter, and proposed materials for the coating include: silica dioxide, plain tantala, tantala pentoxide doped with Titania dioxide, titania, aluminum.

TN is also known as Brownian Noise, taking this name from the analogy with the jiggling of a particle within a medium, due to random collisions with other molecules, that was noted by R. Brown in 1827. This microscopic motion of molecules is the heat. In 1905, Einstein predicted that the mean square position, $\langle x^2(t)\rangle$, of a particle subjected to Brownian motion obeys the following relation

$$\left\langle x^2(t)\right\rangle = 2k_B T B t, \tag{5.1}$$

where k_B is the Boltzmann's constant[2], T is the temperature, B the mobility of the particle, depending on its size and the surrounding medium, t is the time. This expression was the first link between fluctuation, $x(t)$, and dissipation (due to collisions).

The fluctuations analogous to Brownian motion in any system with dissipation obey the Fluctuation-Dissipation theorem (FDT), formulated by Callen et al [25]. The power spectral density[3] (PSD) of the thermal driving force (playing the role of the random collisions) is given by

$$S_{th}(f) = 4k_B T \Re\left[Z(f)\right], \tag{5.2}$$

where $Z(f)$ is the mechanical impedance, defined as $Z(f) = F(f)/v(f)$, F being a force applied to the mass and v is its velocity. The FDT states that the PSD of the mass fluctuations is directly proportional to the real part of the mechanical admittance $Y(f) = Z(f)^{-1}$, $\Re\left[Y(f)\right]$, viz.

---

[1] To be precise, this is strictly true only for what will be called later thermo-optic noise. Coating Brownian noise (see later), on the other hand, simply sums to the substrate contribution, but this latter is negligible with respect to the former.

[2] k_B= 1.3806504 10-23 J/K.

[3] Unless otherwise specified, throughout this Chapter, I will refer to the one-sided power spectral density.

$$S_x(f) = \frac{k_B T \Re\left[Y(f)\right]}{\pi^2 f^2}. \tag{5.3}$$

The first method to compute the thermal noise was based on a normal-mode expansion [15, 134], and on the Equipartition theorem[4]. Levin in [151] proposed a direct application of the FDT to do the calculation, first introduced by Gonzalez and Saulson [99], which turned out to be more powerful and less computationally expensive. This method consists in i) mentally apply a pressure of amplitude F_0 oscillating at given frequency f_0 to the mass surface (Levin used a Gaussian profile for the oscillating pressure mimicking that of the Gaussian laser beam incident on the mirror), ii) compute the dissipated power P_d (the average power converted to heat), which is connected to the real part of the admittance as follows [151]

$$\Re\left[Y(f)\right] = \frac{2P_d}{F_0^2}; \tag{5.4}$$

iii) evaluate the PSD of fluctuactions depending on the dissipated power through the following equation, obtained by eqs. (5.3) and (5.4),

$$S_x(f) = \frac{2k_B T}{\pi^2 f^2}\frac{P_d}{F_0^2}. \tag{5.5}$$

In the following Sections I analyze the different components of the TN, all due to the thermal fluctuations, but associated to different mechanisms of dissipation, and provide the guidelines to compute their PSDs.

5.1.1 Internal Friction

Internal friction in solids was identified by Kimball [112], who described it as a phase shift between stress and strain. This is the TN component which is usually denoted, although being not strictly precise, as *Brownian (motion)* noise. The figure of merit for internal friction in a material is the *loss angle*, ϕ, defined as the phase of the complex elastic Young modulus [5],

---

[4] According to the Equipartition theorem, the average energy is equally distributed over all mechanical modes of the mirror. Hence the total TN is computed by summing the contributions of single modes.

[5] Young's modulus, Y, describes tensile elasticity, or the tendency of an object to deform along an axis when opposing forces are applied along that axis; it is defined as the ratio of tensile stress to tensile strain.

$$Y = Y_0(1 + \imath\phi). \tag{5.6}$$

One model for internal friction, identified by Saulson [134], is the *structural damping*, in which ϕ is independent on frequency. In the case of homogenously distributed damping, as in the case of the mirror substrate, the spectral density of fluctuations is [29]

$$S_x^B(f) = \frac{4k_B T}{(2\pi)^{3/2} f} \frac{\phi(f)\,(1-\sigma^2)}{Y r_0}, \tag{5.7}$$

where σ is the Poisson's ratio [6], and r_0 is the radius of the laser beam ($1/e$ of central power)[7]. Here and henceforth ϕ will be assumed to be constant in frequency.

If a multilayer dielectric coating is laid on top of the mass, its contribution to $S_x^B(f)$ is taken into account by substituting ϕ, in eq. (5.7), with the effective loss angle ϕ_{tot} of the mirror, given by the sum of the loss angle of the substrate, ϕ, and the effective loss angle of the coating, ϕ_{coat}, i.e.

$$\phi_{tot} = \phi + \phi_{coat}, \tag{5.8}$$

where ϕ_{coat} is given by

$$\begin{aligned} \phi_{coat} &= d/\left(\sqrt{\pi} r_0 Y_\perp\right) \cdot \\ &\left(\left(Y/(1-\sigma_\perp) - 2\sigma_\perp^2 Y Y_{||}/\left(Y_\perp\left(1-\sigma^2\right)\left(1-\sigma_{||}\right)\right)\right)\phi_\perp\right. \\ &+ Y_{||}\sigma_\perp\left(1-2\sigma\right)/\left(\left(1-\sigma_{||}\right)\left(1-\sigma\right)\right)\left(\phi_{||}-\phi_\perp\right) \\ &\left.+ Y_{||}Y_\perp\left(1+\sigma\right)\left(1-2\sigma\right)^2/\left(Y\left(1-\sigma_{||}^2\right)\left(1-\sigma\right)\right)\phi_{||}\right), \end{aligned} \tag{5.9}$$

where d is the coating physical thickness, Y, σ and ϕ are the Young's moduli, the Poisson's ratios and loss angles of the substrate (no subscript), the coating for stress perpendicular (subscript $\perp$), and parallel (subscript $||$) to the optic face. The elastic constants of the coating can be obtained from the bulk values of the materials making up the coating. If the alternating dielectrics are two, denoted with the subscripts 1 and 2, the following equations are valid

---

[6] Poisson's ratio is the ratio of the contraction or transverse strain (perpendicular to the applied load), to the extension or axial strain (in the direction of the applied load).

[7] Note that for some authors the definition of r_0 can vary by a factor of $\sqrt{2}$.

$$
\begin{aligned}
Y_\perp &= (d_1 + d_2)/(d_1/Y_1 + d_2/Y_2) \\
Y_{||} &= (Y_1 d_1 + Y_2 d_2)/(d_1 + d_2) \\
\sigma_\perp &= (\sigma_1 Y_1 d_1 + \sigma_2 Y_2 d_2)/(Y_1 d_1 + Y_2 d_2) \\
\phi_\perp &= Y_\perp(\phi_1 d_1/Y_1 + \phi_2 d_2/Y_2) \\
\phi_{||} &= (Y_1 \phi_1 d_1 + Y_2 \phi_2)/(Y_{||}(d_1 + d_2)).
\end{aligned}
\tag{5.10}
$$

while $\sigma_{||}$ satisfies the following equation

$$
\frac{\sigma_1 Y_1}{(1+\sigma_1)(1-2\sigma_1)} + \frac{(d_2/d_1)\sigma_2 Y_2}{(1+\sigma_2)(1-2\sigma_2)} = -\frac{Y_{||}(\sigma_\perp^2 Y_{||} + \sigma_{||} Y_\perp)(1 + d_2/d_1)}{(\sigma_{||}+1)\left(2\sigma_\perp^2 Y_{||} - (1-\sigma_{||})Y_\perp\right)}. \tag{5.11}
$$

If all Poisson's ratios are small[8], eq. (5.9) can be approximated by the following simpler formula

$$
\phi_{coat} \approx \frac{d}{\sqrt{\pi} r_0}\left(\frac{Y}{Y_\perp}\phi_\perp + \frac{Y_{||}}{Y}\phi_{||}\right). \tag{5.12}
$$

From the approximation in eq. (5.12), it is evident that, as long as $\phi_\perp \approx \phi_{||}$, matching coating and substrate Young's moduli helps reducing the thermal noise from internal friction. An acceptably good matching can be achieved using silica substrates. Furthermore, in this case, the substrate contribution to Browanian noise is negligible with respect to that of the coating, i.e. $\phi << \phi_{coat}$ and $\phi_{tot} \approx \phi_{coat}$.

With a little algebra, it is possible to write eq. (5.12) in the following convenient form

$$
\phi_{coat} \approx (b_1 d_1 + b_2 d_2), \tag{5.13}
$$

where

$$
b_{1,2} = \frac{\lambda_0}{\sqrt{2\pi} r_0}\frac{\phi_{1,2}}{n_{1,2}}\left(\frac{Y_{1,2}}{Y} + \frac{Y}{Y_{1,2}}\right) \tag{5.14}
$$

is the loss density for unit thickness of material 1 and 2, respectively.

---

[8] For the case of fused silica or sapphire substrates coated with alternating layers of Ta_2O_5 and SiO_2, the Poissons ratio of the coating may be small enough (≤ 0.25) to allow this approximation.

5.1.2 Thermo-Elastic Noise

Thermo-Elastic (TE) noise is the name given to the TN due to thermo-elastic dissipation, i.e. the dissipation due to heat flow down temperature gradients, produced by inhomogeneous compression and expansion of the test mass material. The method of calculation of such noise is, as before, the one adopted in [151]: i) imagine applying a sinusoidally oscillating pressure to one face of the test mass, with the same spatial profile as that of the laser beam; ii) compute the energy dissipated by thermo-elastic flow and iii) use this latter quantity in eq. (5.5).

For infinite size test masses, the thermoelastic noise in a homogeneous mass is given by [30, 143]

$$S_x^{TE}(f) = \frac{8(1+\sigma)^2 \kappa \alpha^2 k_B T^2}{\sqrt{2\pi} C_V^2 \rho^2 r_0^3 (2\pi f)^2}, \tag{5.15}$$

where, here and throughout this Chapter, α is the linear thermal expansion coefficient, defined as

$$\alpha = \frac{1}{l}\frac{dl}{dT}, \tag{5.16}$$

κ is the thermal conductivity of the material, ρ is the volume density, and C_V is the specific heat per unit mass at constant volume. For finite size test-masses, the PSD of thermal noise can be obtained by including in eq. (5.15) a correction factor [143], which is, however, only several percents for typical mirror sizes.

Braginsky and Vyatchanin in [24] computed the PSD of TE noise due to thermodynamical fluctuations in thin coating, with elastic properties different from those of the mirror substrate. For a thin coating, the thickness d is much smaller than the diffusive heat transfer characteristic length $l_c = \sqrt{\kappa/\rho C_V 2\pi f}$, f being the frequency of observation; hence we may consider TD temperature fluctuations in the coating to be the same, and independent on its specific thickness. The simple way the authors in [24] adopted to do this calculation is the following.

Using the definition of α in eq. (5.16), the displacement of the coating outer surface can be written to first order in the temperature fluctuations ΔT[9],

$$\Delta x^{TE}\big|_c \cong -\alpha_{eff} d \Delta T, \tag{5.17}$$

where α_{eff} is the effective coating TE coefficient[10]. Denoting, as above, the quantities referring to the two materials making up the coating with the subscripts 1 and 2, and no subscript for the quantities of the substrate, α_{eff} is given by

---

[9] By definition, temperature does not fluctuate. Here, temperature fluctuations express energy fluctuations.

[10] The x axis being oriented toward the substrate, $\Delta x^{TE}\big|_c$ should be negative, for positive α_{eff}.

$$\alpha_{eff} = (1+\sigma)^2 \left(\frac{\alpha_1 d_1}{d_1+d_2} \frac{Y_1(1-2\sigma)}{Y(1-2\sigma_1)} + \frac{\alpha_2 d_2}{d_1+d_2} \frac{Y_2(1-2\sigma)}{Y(1-2\sigma_2)} - \alpha \right), \tag{5.18}$$

and the PSD of surface fluctuations due to TE damping in the coating is

$$S_c^{TE}(f) = \left(\frac{\Delta x^{TE}}{\Delta T} \right)^2 S_{\Delta T}(f) = \frac{4\sqrt{2}}{\pi} \frac{\alpha_{eff}^2 d^2 k_B T^2}{r_0^2 \sqrt{\kappa \rho C_V 2\pi f}}. \tag{5.19}$$

Taking into account the finite size of the mirror, a multiplicative factor must be included in eq. (5.19), which for realistic values of LIGO coating is slightly larger than 1 [24].

For fused silica substrates, the substrate TE contribution is more than one order of magnitude smaller than that of the coating, and hence can be ignored; while for sapphire substrates, it is dominant with respect to the coating TE contribution.

5.1.3 Thermo-Refractive Noise

Thermodynamical fluctuations of temperature in mirrors produce additional noise, not only through thermal expansion, but also through the dependence on the temperature of the refraction indexes of materials composing the test masses. This change in the refraction indexes produce change in the phase of the reflected wave, which is seen at the photodetector as fluctuations of the mirror surface. These fluctuations are known as Thermo-Refractive (TR) noise, and the associated loss mechanism is the electrocaloric dissipation [142]. While reflecting, the optical wave penetrates in the test mass on a certain depth, which, for the LIGO experiment, is of the order of magnitude of $\sim 1\mu$. In view of the presence of a multilayer dielectric coating on the mass' surface, the penetration depth involves only the very first few layers of the coating, which are the only ones contributing to TR noise[11]. The penetration depth is much smaller than the characteristic length of diffusive heat transfer, l_c; hence, as before, we may consider the fluctuations of temperature as correlated in the layers. The dependence of the refraction indexes n_i of the coating materials is measured by the thermo-refractive coefficients $\beta_i = dn_i/dT$. We can use the reflection coefficient transport equation [102] to find that, to first order in the temperature fluctuations ΔT, the following approximation is valid

$$\Delta x^{TR} \cong \lambda_0 \beta_{eff} \Delta T, \tag{5.20}$$

---

[11] Other contributions to TR noise are given by the optics laser beam passes through, e.g. the beamsplitter. However these are not major contributions [142].

where β_{eff} is the effective coating thermo-refractive coefficient and λ_0 is the operation wavelength *in vacuo*. Braginsky et al. in [31] computed the PSD of TR noise in IFO test masses to be

$$S_x^{TR}(f) = \beta_{eff}^2 \lambda^2 \frac{\sqrt{2} k_B T^2}{\pi r_0^2 \sqrt{2\pi \rho C_V \kappa f}}, \tag{5.21}$$

where β_{eff} for the case of coatings made of cascaded quarter-wavelength (QWL) low-high index doublets is given by

$$\beta_{eff}|_{QWL} = \frac{n_H^2 \beta_L + n_L^2 \beta_H}{4(n_L^2 - n_H^2)}. \tag{5.22}$$

I generalized this formula to the case of non-QWL coatings, which is of interest in view of the coating optimization described in the next Chapter. Such a generalization is given by [10]

$$\beta_{eff} = -\frac{1}{2\pi} \left(\frac{\Delta \overline{B}}{1 + \overline{B}_0^2} \right), \tag{5.23}$$

where $\overline{Y}^{(0)} = \imath \overline{B}_0$ and $\Delta \overline{Y} = \imath \Delta \overline{B}$ are, respectively, the (normalized) input admittance of the coating at the reference temperature ($T = T_0$) and its variation due to temperature deviation from T_0, to first order in ΔT. The derivation of formulas in eq. (5.22) and (5.23) is reported in Appendix B.

5.2 Thermo-Optic versus Brownian Noise

A crucial assumption implicitly made above is the *adiabaticity*, i.e. the temperature in the coating does not fluctuate on characteristic time scales whereby the multiply reflected field in the coating builds up. This assumption, togheter with the already mentioned spatial uniformity of the temperature fluctuations across the coating thickness, suggests that thermo-elastic and thermo-refractive fluctuations should be *coherently* summed to form what is called *thermo-optic* (TO) noise, whose PSD would be

$$S_x^{TO}(f) = \left(\frac{\Delta x^{TE}}{\Delta T} + \frac{\Delta x^{TR}}{\Delta T} \right)^2 S_{\Delta T}(f) = (\alpha_{eff} d + \beta_{eff} \lambda)^2 \, \frac{\sqrt{2} k_B T^2}{\pi r_0^2 \sqrt{2\pi f C_V \rho \kappa}}. \tag{5.24}$$

However, the *coherent* versus the *incoherent* sum of TE and TR noises is still matter of debate. In [67] the authors showed that TE and TR have opposite signs when summed coherently, and there exists a frequency where they sum to zero. However, preliminary measurements under work at Caltech laboratories do not confirm this result.

For its low mechanical loss angle and low TE contribution, the substrate for AdLIGO will be made by fused silica, so that becomes crucial the optimization of the coating, in order to reduce the total amount of thermal noise.

Chapter 6

Coating Optimization for minimal Thermal Noise

After a brief review of multilayer dielectric mirrors, the problem of coating optimization is formulated. First, the optimization strategy for single-wavelength operation is described and the results of experimental measurements of Brownian noise on an optimized monochroic prototype are discussed. Then, the optimization strategy is extended to the more complicated case of double-wavelength operation, and applied to the design of optimized coatings for the *end* and *inner* test masses of AdLIGO.

6.1 AdLIGO Coating Requirements

The test masses in GW interferometers (IFOs) (Figure 6.1) are coated with dielectric layers in order to guarantee low optical losses and high reflectance, Γ, (or reduce their power transmittance τ) at the operation wavelength(s). The higher the reflectivity of these masses, the higher the *finesse* of the Fabry-Perot cavity, formed in any arm by a couple of masses (mirrors). In turn, a high value of the finesse allows a better resolution of the interference fringes at the photodetector placed at the output of the instrument [115]. The masses closer to the beamsplitter in any arm are called *inner* or *input* test masses, ITMs, while the ones at the opposite ends of the arms are called *end* test masses, ETMs (see Figure 6.1). The reflectivity requirements are different for ITMs and ETMs.

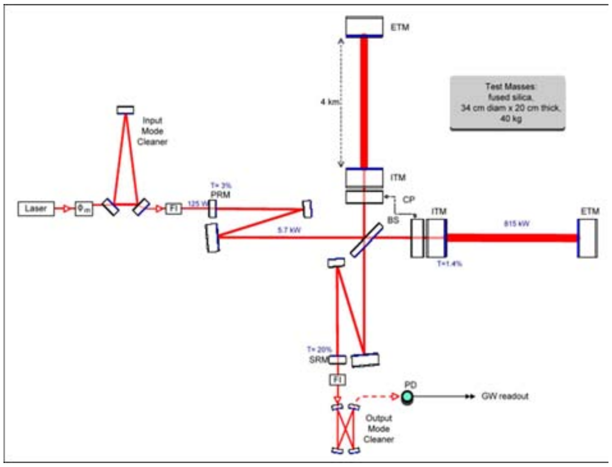

Figure 6.1: Simplified optical scheme of a Michelson-Morley interferometer for GW detection.

The operation wavelength is $\lambda_0 = 1024\ nm$, at which the initial LIGO design required a transmittance of 3% on the ITMs and between 5 and $10ppm$ for the ETMs. For the Advanced LIGO (AdLIGO) design [146], the requirements on the transmittances become more stringent, i.e. 1.4% for the ITMs and $< 6ppm$ for the ETMs. Furthermore, AdLIGO is required to operate at double-wavelength, where the second wavelength ($532\ nm$, second harmonic of the main beam) is needed by the new cavity alignment locking system. In addition, sufficient high reflectance is recommended on a third wavelength (e.g. $670\ nm$) used for Hartmann sensors, as well as optical levers at some wavelength to be chosen among 670, 946, 980, 1319, 1550 nm [22]. Table 6.1 summarizes the AdLIGO optical requirements.

As of today, the coating is made by alternating layers of two dielectric materials, with low and high refraction index, respectively. Currently preferred materials (see Table 6.2 for their properties of interest here) are: silica dioxide, for the low index material, and tantala

Table 6.1: AdLIGO Requirements on test masses optical properties. Source: AdLIGO wiki.

	ITM	ETM
τ@1064nm	14000 ppm	< 6 ppm
Γ@532nm	> 0.99	0.85 to 0.99 (pref 0.95)
Γ@670nm	> 0.05	unsp

Table 6.2: Refraction index, loss angle and Young modulus of candidate materials for coatings.

	n@1064nm	ϕ	Y
Silica dioxide (SiO_2)	1.46	$4\ 10^{-5}$	$72\ 10^{9}$
Tantala pentoxide (Ta_2O_5)	2.09	$4\ 10^{-4}$	$140\ 10^{9}$
Titania dioxide-doped Tantala pentoxide ($TiO_2 :: Ta_2O_5$)	2.12	$2\ 10^{-4}$	-

pentoxide doped with titania dioxide[1], for the high index material. This latter exhibits lower mechanical loss (and lower optical absorption) than pure tantala [71]. While the use of the silica dioxide for the low-index material has no controversies, other materials have been proposed in the past for the high-index material in the coatings, e.g. niobia, hafnia, alumina. Indeed, silica exhibits a very low mechanical loss angle, while the greatest contribution to TN is given by the high-index material, whose loss angle is about one order of magnitude larger than that of silica. In this respect, it is anticipated that the optimal coating configuration will use less high-index (more lossy) material compared to the standard quarter-wavelength design. For protective purposes, the first layer of any coating is silica, because of its hardness.

The coating optimization problem consists in finding the coating configuration that, while satisfying the optical requirements, features minimal thermal noise.

We consider here only the Brownian component, since, as I will show in Section 6.3, the thermo-optic (TO) component if relevant will be minimized at the same time. The PSD of Brownian noise due to coating is given by

$$S^B_{coat}(f) = \frac{4k_BT}{(2\pi)^{3/2}f}\frac{\phi_{coat}\,(1-\sigma^2)}{E_0r_0}, \tag{6.1}$$

where ϕ_{coat} is given by eq. (5.9) or approximated by (5.12). From the expression above, it is evident that, to minimize S^B_{coat} by varying the structure of the coating, the quantity to be minimized is the effective loss angle, ϕ_{coat}, which is the only factor depending on the coating configuration. There are two possible directions to minimize ϕ_{coat}: i) fix the materials and find the optimal set of layers' thicknesses; ii) synthesize new low-loss materials through proper mixture techniques [21], e.g. using pure titania dioxide, which exhibits higher refraction index and lower loss angle than titania-doped tantala, but is prone to crystalization for regular values of thickness used for coatings.

---

[1] The doped tantala is obtained using the Formula 5 of *Laboratoires des Materiaux Avances* in Lyon, France, corresponding to an incorporation of 14% of titania in a tantala layer [65].

Note that a reduction of $p\%$ in ϕ_{coat} means an increase of $p^{-3/2}\%$ in the event rate and the visibility volume, assuming an isotropic source distribution[2].

In this study I explored the first direction to solve the coating optimization problem, while the second direction is being currenlty investigated in collaboration with Caltech [84].

6.2 Multilayer Coating Reflectivity

We consider the general stack, shown in Figure 6.2, constisting of an arbitrary number M of dielectric slabs with refraction indexes n_i and arbitrary phase thicknesses $\delta_i = k_i l_i = 2\pi n_i l_i/\lambda$, where l_i is the physical thickness of slab i and λ is the operation wavelength. The left and right most media are semi-infinite and the corresponding quantities are denoted with subscripts a and b, respectively. We assume a plane wave incident on the structure from the medium a, a time-harmonic dependence as $exp(\imath\omega t)$.

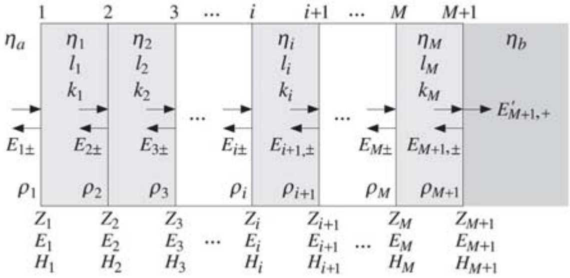

Figure 6.2: General multilayer dielectric slab stracture.

The (dimensionless) transmission matrix $\mathbf{T}$ for the i-th dielectric layer, relating the complex electric E and magnetic H field amplitudes at its terminal interfaces, viz.

$$\begin{bmatrix} E_i \\ Z_0 H_i \end{bmatrix} = \mathbf{T} \begin{bmatrix} E_{i+1} \\ Z_0 H_{i+1} \end{bmatrix}, \; i = M, M-1, \dots, 1, \tag{6.2}$$

---

[2] This can be easily obtained from the fact that the minimum detectable GW amplitude $h_{min} \propto S_x^{1/2}$, and $h_{min} \propto r_{max}^{-1}$. Hence the event rate in the visibility volume r_{max}^3, assuming an isotropic soucre distribution is proportional to $S_n^{-3/2}$.

is given by [102]

$$\mathbf{T} = \left[\begin{array}{cc} cos(\delta_i) & \imath n_i^{-1} sin(\delta_i) \\ \imath n_i sin(\delta_i) & cos(\delta_i) \end{array} \right] \tag{6.3}$$

where $Z_0 = \sqrt{\mu_0/\epsilon_0}$ is the vacumm characteristic impedance. One way to compute the electromagnetic fields at the left-most interface ($i = 1$) is to recursively evaluate it at each interface, starting from the $(M+1)$-th interface

$$\left[\begin{array}{c} E_{M+1} \\ Z_0 H_{M+1} \end{array} \right] = \left[\begin{array}{c} 1 \\ n_{M+1} \end{array} \right] E'_{M+1,+}. \tag{6.4}$$

From $\{E_1, H_1\}$ it is possible to compute the input impedance $Z_1 = E_1/H_1$, and the reflection coefficient $\mathcal{R}$ of the whole multilayer structure at the leftmost interface, viz.

$$\mathcal{R} = \frac{Z_a - Z_1}{Z_a + Z_1}. \tag{6.5}$$

We shall focus on (truncated) periodic multilayer structure, made of $M/2$ identical *doublets*, whose transmission matrix is given by

$$\mathbf{T}_D = \mathbf{T}_1 \cdot \mathbf{T}_2, \tag{6.6}$$

where $\mathbf{T}_{1,2}$ are the transmission matrices of the two layers, computed via eq. (6.3). In this case the recursive evaluation reduces to

$$\left[\begin{array}{c} E_1 \\ Z_0 H_1 \end{array} \right] = \mathbf{T}_D^{M/2} \left[\begin{array}{c} E_{M+1} \\ Z_0 H_{M+1} \end{array} \right], \tag{6.7}$$

and the behavior of the multilayer coating is ruled by the eigenvalues of $\mathbf{T}_D$ [102], which are most conveniently written as exponentials, i.e.

$$\beta = \exp \imath B, \tag{6.8}$$

where B is the *Bloch exponent*. In the absence of optical losses, there are two values for B, either purely real or imaginary, differing only by the sign. A lossless infinite periodic structure exhibits an infinite sequence of alternating frequency bands where propagation is either allowed (transmission bands) or forbidden (reflection bands), according to whether the B is either purely real or imaginary, respectively.

6.3 Monochroic Optimization

The coating multilayer structure, represented schematically in Figure 6.2, must be properly designed in order to satisfy the AdLIGO requirements. In this section I consider the single-wavelength operation. Here and henceforth, subscripts L and H are used to denote quantities corresponding, respectively, to the low and high index material.

6.3.1 The Reference Design

The coating structure achieving a desired value of transmittance with the minimum number of doublets, $N_D = M/2$, M being the total number of layers is the (truncated) periodic quarter-wavelength (QWL) configuration, where $\delta_i = \pi/2, \forall i = 1, \ldots, 2N_D$. In this case, it is possible to write the exact expression of the coating reflection coefficient $\mathcal{R}$ at λ_0, viz.

$$\mathcal{R}(\lambda_0) = \frac{1 - \left(\frac{n_H}{n_L}\right)^{N_D} \frac{n_H^2}{n_a n_b}}{1 + \left(\frac{n_H}{n_L}\right)^{N_D} \frac{n_H^2}{n_a n_b}}, \tag{6.9}$$

which, for $N_D \to \infty$, approaches -1, i.e. total reflection, and whose bandwidth can be easily computed as the separation between the wavelenghts where the Bloch exponent changes from pure real to pure imaginary and viceversa. This results in [102]

$$\frac{\Delta\lambda}{\lambda_0} = \frac{\pi}{2}\left[\frac{1}{\text{acos}(\rho)} - \frac{1}{\text{acos}(-\rho)}\right], \ \rho = \frac{n_H - n_L}{n_H + n_L}. \tag{6.10}$$

Figure 6.3 shows the reflectivity of the ETM design over the whole useful range of frequency[3]

6.3.2 The Optimized Design

In [49] genetic algorithms [152] were used for synthesizing minimal noise coatings where all layer thicknesses were treated as free parameters. It was found that the optimal coating configuration converges to a cascade of identical doublets, each of which has a phase thickness is about π, i.e. half-wavelength (HWL). Deviations from the above are confined only to the terminal layers. This suggests restricting the optimization study to coating geometries consisting of identical cascaded doublets, each having a total phase thickness of π, thus

---

[3] Throughout this Chapter the reflectivity spectra are computed by using for the real part of the refraction index, a function of the frequency obtained by interpolating some known values at few frequencies [35]. The extintion coefficient is ignored in the analysis, since it is several order of magnitude smaller than the refraction index in the frequency band of interest.

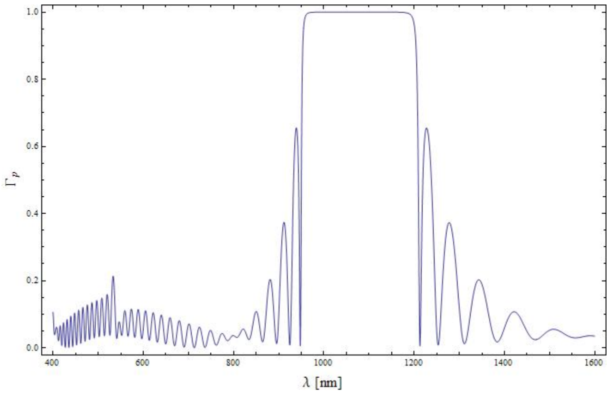

Figure 6.3: Power reflectivity spectrum for the QWL design satisfying ETM requirement in single-wavelength operation.

reducing dramatically the dimensionality of the optimization problem from $1 + 2N_D$ to N_D, the two degrees of freedom being the total number of doublets N_D and a quantity ξ in [0, 1/4] such that

$$z_H = \frac{1}{4} - \xi, \; z_L = \frac{1}{4} + \xi, \tag{6.11}$$

where z_i is the layer thickness in units of local wavelength, defined as $z_i = n_i l_i/\lambda_0$.

The suggested optimization strategy consists in the following steps: i) start from the QWL design achieving the desired transmittance; ii) add one doublet[4], and adjust the layers' thicknesses varying ξ, until the desired value of the transmittance is recovered; iii) calculate the ϕ_{coat} of the current coating configuration according to eq. (5.12); iv) repeat steps ii)-iii) until the minimum of ϕ_{coat} is found. At the end of this procedure, further improvement can be obtained by tweaking the thicknesses of the two terminal layers[5]

The *Thermal Noise Interferometer* (TNI) [59] is a small-scale interferometer built at Caltech to measure accurately the coating thermal noise. A TNI tailored prototype has been designed to validate experimentally the efficacy and accuracy of the optimization strategy.

then realized by the *Laboratoires des Materiaux Avances* (LMA) in Lyon, France, in order to test

The required transmittance for the TNI at $\lambda_0 = 1064nm$ is 300ppm. To achieve this transmittance value, the reference QWL design consists of 14 silica/tantala doublets (Figure

---

[4] Since the QWL configuration is the one achieving a given value of transmittance with the minimum number of doublets, any deviation from the QWL configuration *must* imply an increase in the number of doublets to conserve the same transmittance.

[5] In [49] it was shown that tweaking the further layers next to the first and last terminal layers produces less dramatic improvement.

6.4), and exhibits a transmittance of 278ppm at the operation wavelength[6].

The optimized coating was constrained to have the same transmittance value at the operation wavelength, in order to measure the net effect of the optimized layers' thicknesses. Figure 6.5 shows the effective coating loss angles (normalized to that of the reference design) computed at step iii) of the optimization strategy, as N_D is increased (and ξ is correspondigly adjusted). The minimum noise configuration stems from a balance between the reduction in the amount of tantala, which reduces noise, and the parallel increase in the amount of silica, which increases noise. The minimum thermal noise is achieved at $N_D = 17$, when these two effects balance (Figure 6.5).

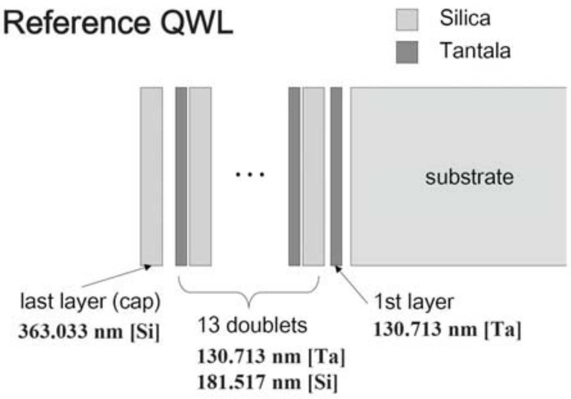

Figure 6.4: The structure of the reference quarter-wavelength TNI coating.

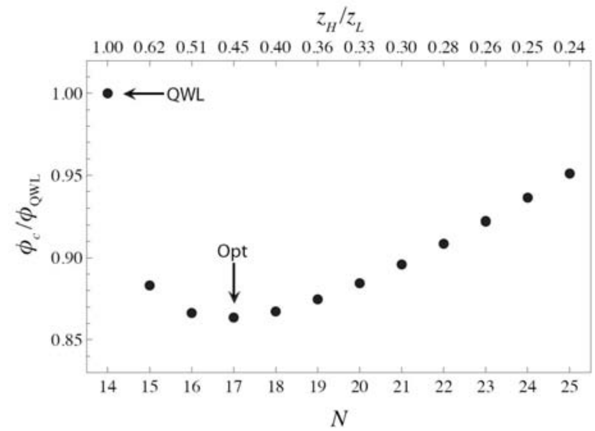

Figure 6.5: Coating loss angle reduction factor as a function of the number of doublets N_D. The corresponding values of the ration z_H/z_L are shown at the top of the plot. The QWL and the optimized coatings are indicated.

---

[6] Note that, in this reference design, a HWL silica cap is included for protective purposes.

Further reduction of the coating loss angle can be achieved by tweaking the design obtained above, by adjusting the thicknesseses of the two terminal layers, as suggested by GAs, while keeping the reflectance unchanges [88].

The optimized TNI coating configuration is shown in Figure 6.6. Using the approximated formula in eq. (5.12), and a value for $b_H/b_L \approx 7$, the predicted ratio between the effective coating loss angle of the optimized and reference QWL configuration is 0.843.

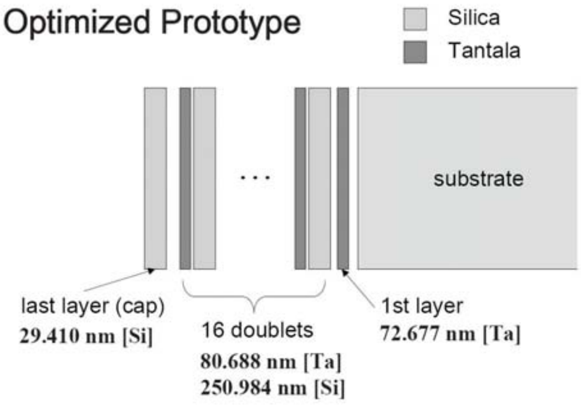

Figure 6.6: Structure of the optimized TNI coating.

6.3.3 Direct Measurements

The optimized design for the TNI was manufactured by LMA (Laboratoires des Materiaux Avances, CNRS, Lyon FR, a member of LIGO-Virgo collaboration), and tested at Caltech to verify the compliance of actual (measured) with theoretically expected values of the coating loss angle reduction. Figure 6.7 shows the spectral density of TNI cavity length noise for the QWL design, and the analysis region, where the effective coating loss angle has been estimated from measurements for both designs.

The measurement setup and data analysis procedure is described in detail in [88]. The measured loss angle reduction factor was (0.82 ± 0.04). Comparing such a result with the predicted ratio of 0.843, this latter turns out to be within the uncertainty range of the measures, confirming the validity of the theoretical model and the effectiveness of the optimization strategy. In Figure 6.8 the measured spectra of the QWL (light) and the optimized (dark) cavity length noise are plotted, after a Savitzky-Golay smoothing filter [20] was applied to them, showing clearly that the optimized design entails a sensible reduction on ϕ_{coat}.

Inclusion of thermo-optica noise does not yield a different optimized design, as shown in Figure 6.9, irrespective of how the thermo-elastic and thermo-refractive components combine.

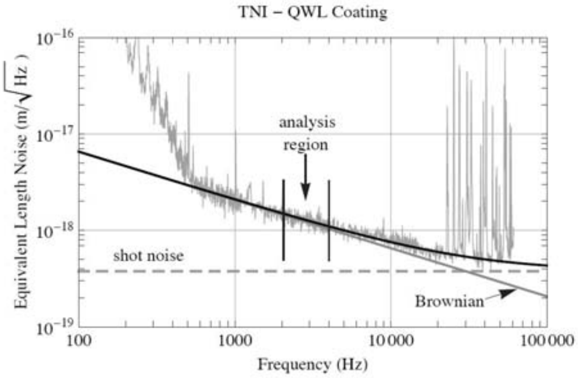

Figure 6.7: Measured spectral density of the cavity length noise for the QWL design along with the shot noise (dashed line) and Brownian noise (solid line). The two vertical lines identify the analysis region, where the fit was done to extract the loss angle.

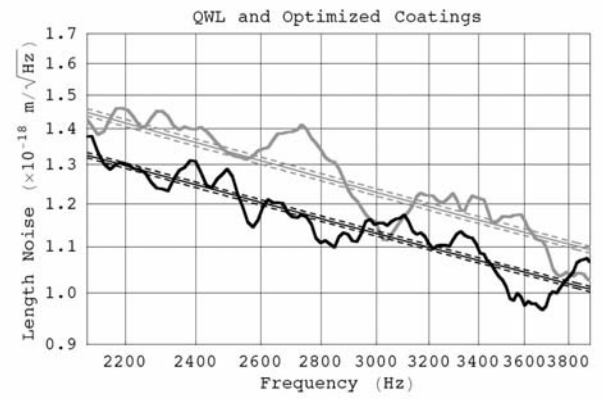

Figure 6.8: Plot of the measured spectra in the analysis region after the Savitzky-Golay smoothing filter was applied.

6.4 Dichroic Optimization

In AdLIGO, high reflectivity is required at two wavelengths, $\lambda_0 = 1064nm$ and $\lambda_1 = 532nm$, according to Table 6.1, and the optimization strategy described in the previous Section must be suitably reformulated.

6.4.1 The Reference Design

The simplest *dichroic* design, which was proposed first and used as a reference, consists of a first stack grown on top of the substrate, where

$$l_L n_L = \frac{\lambda_0}{8} = \frac{\lambda_1}{4},\ l_H n_H = \frac{3\lambda_0}{8} = \frac{\lambda_1}{4} + \frac{\lambda_1}{2}, \tag{6.12}$$

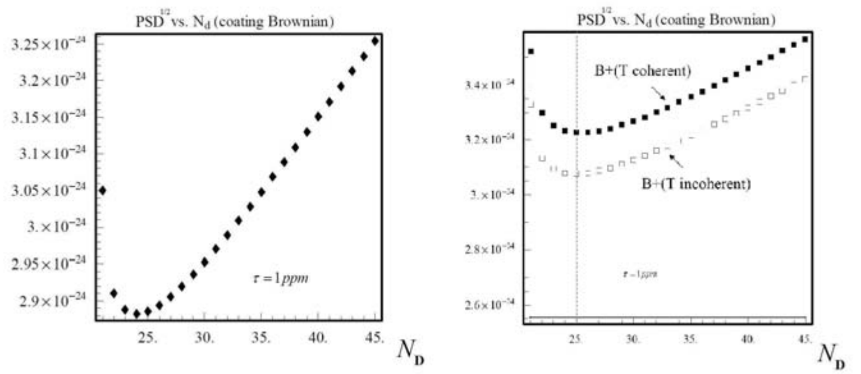

Figure 6.9: Square root of coating noise PSD versus the number of doublets. Left: Brownian noise only. Right: Brownian and thermo-optic noise.

and a second stack, grown on top of the first one, where

$$l_L n_L = \frac{\lambda_0}{4} = \frac{\lambda_1}{2},\ l_H n_H = \frac{\lambda_0}{4} = \frac{\lambda_1}{2}. \tag{6.13}$$

The first stack provides the required reflectance at λ_1; the second one, while being ideally transparent at λ_1, provides the required reflectance at λ_0 [7].

The reference design for the ETMs and ITMs, satisfying the AdLIGO requirements, are schematically represented in Figure 6.10, its key features are summerized in Table 6.3, and the corresponding reflectivity spectra are plotted in Figures 6.11, 6.12. For the ITMs, a single $\left(\frac{\lambda_0}{8}, \frac{3\lambda_0}{8}\right)$-stack is enough to achieve the required transmitance at both λ_0 and λ_1.

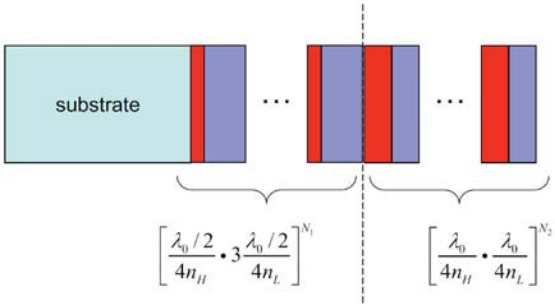
substrate
...
...
$\left[\frac{\lambda_0/2}{4n_H}\cdot 3\frac{\lambda_0/2}{4n_L}\right]^{N_1}$
$\left[\frac{\lambda_0}{4n_H}\cdot\frac{\lambda_0}{4n_L}\right]^{N_2}$

Figure 6.10: Schematic representation of the ETM reference dichroic design. The ITM reference design consists only of the bottom stack. Parameters of both designs are in Table 6.3.

---

[7] Note, however, that this reasoning is only approximate, since the dispersion of the materials is ignored.

Table 6.3: Parameters of ETM and ITM reference dichroic designs.

	ITM	ETM
N_1	11	7
N_2	0	14
τ_P@1064nm	11300ppm	4.45ppm
Γ_P@670nm	0.999	0.949
ϕ_{coat}	3.055 10^{-9}	7.422 10^{-9}

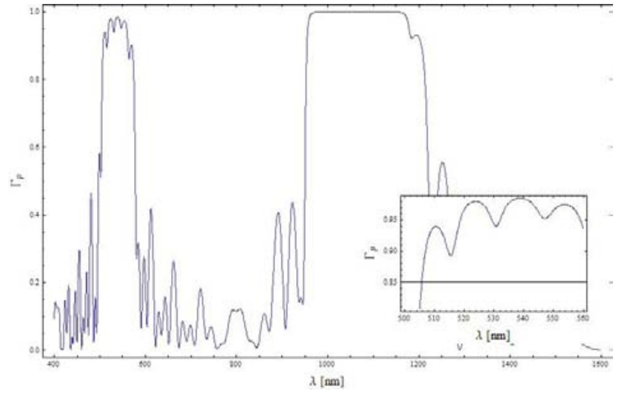

Figure 6.11: Power reflectivity spectrum of ETM reference dichroic design. A close-up around the second operation wavelength is shown in the inset.

6.4.2 The Optimized Design

Extensive implementations of genetic algorithms, where any layer thickness is a free parameter, showed that the optimal configuration, even in this case, features an end-tweaked stacked doublets structure, where the total doublet thickness deviates from the HWL, unlike the single-wavelength case. Hence, as before, it is possible to reduce the number of free parameters, from $1 + 2N_D$ to 3, namely the number of doublets N_D and the deviations, ξ_L and ξ_H, from QWL of the low and high index layers, viz.

$$z_H = \frac{1}{4} - \xi_H, \ z_L = \frac{1}{4} + \xi_L, \tag{6.14}$$

where ξ_H, ξ_L vary independently in the range $[0, 1/4]$. Indeed, in view of the additional optical requirement on the second wavelength, one more free parameter is needed with respect to the single-wavelength operation.

The optimization strategy, in this case, consists in i) fixing the number of doublets, identify, for several values of the number of doublets N_D, the (non-empty) region in the (ξ_L, ξ_H)-plane where the AdLIGO reflectance requirements are satisfied; ii) pick, in this

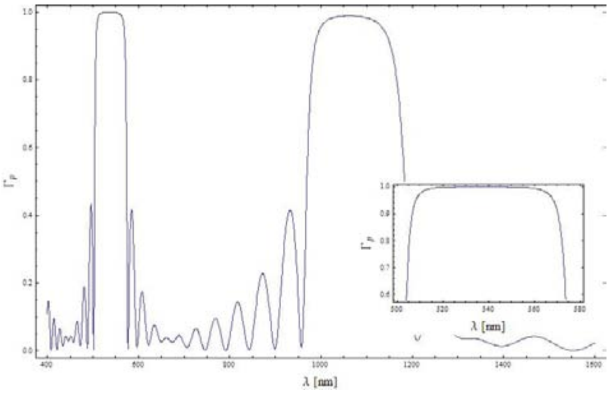

Figure 6.12: Power reflectivity spectrum of ITM reference dichroic design. A close-up around the second operation wavelength is shown in the inset.

region, the minimal Brownian noise point, identified by the triplet (N_D, ξ_L^0, ξ_H^0), and compute the corresponding effective coating loss angle, ϕ_{coat}; iii) identify the triplet exhibiting the minimum value of ϕ_{coat}, among all disegns corresponding to different values of N_D. Further improvement of the design can be achieved by tweaking properly the two extreme layers.

Instead of considering the whole acceptable ranges, indicated in Table 6.1 for the power transmittance at 1064nm ($\tau@1064nm$) and power reflectance at 532 nm ($\Gamma@532m$), which would yield a 2D (bounded) admissibility region in the (ξ_L, ξ_H)-plane, I consider here two *preferred* values for $\tau@1064nm$ and $\Gamma@532m$, so that the admissibility region is actually a set of two points in the (ξ_L, ξ_H)-plane. The chosen *preferred* values are $\tau^{(p)} = 5.5ppm$ and $\Gamma^{(p)} = 0.95$, in order to leave a margin, where the actual values of $\tau@1064nm$ and $\Gamma@532m$ might vary, because of errors of different kinds (e.g. fluctuations of laser wavelength, errors on layers' thicknesses, inaccuracy of refraction index values, etc.).

The optimization strategy, in this case, was applied to design the silica/titania-doped tantala coating for the ETMs and ITMs. The minimum number of doublets yielding a non-empty admissibility region, for the ETM design, is 19. Figure 6.13 shows, in the (ξ_L, ξ_H)-plane, the iso-reflectance at 532 nm and iso-transmittance at 1064 nm curves, corresponding to the preferred values. The two intersections between these curves are acceptable operation points, satisfing the optical requirements at both operation wavelengths. Figure 6.14 shows the behavior of ϕ_{coat} in the same region of the (ξ_L, ξ_H)-plane.

Increasing the number of doublets yields a larger ϕ_{coat}, as Table 6.4 shows. Hence, the best design is given by the configuration with 19 doublets.

The design can be tweaked in order to further reduce its loss angle, by adjusting the thickness of the first and last layers; however, such a reduction is of the order of 0.1%. For this reason, it is more convenient to adjust the thicknesses of the two terminal layers in

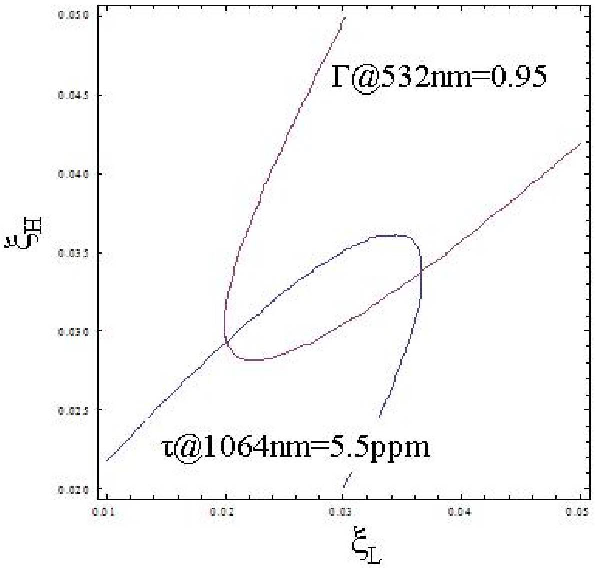

Figure 6.13: Iso-reflectance (0.95 @532nm) and iso-transmittance (5.5 ppm @1064nm) curves in (ξ_L,ξ_H)-plane for 19 doublets, corresponding to the preferred values. The two intersections are acceptable operating points.

Table 6.4: Minimal Brownian noise points in (ξ_L, ξ_H)-plane for different number of doublets for the ETM design.

N_D	ξ_L	ξ_H	ϕ_{coat}
19	0.0201	0.0294	$6.742\ 10^{-9}$
20	0.0262	0.0442	$6.777\ 10^{-9}$
...	...	...	...

order to minimize the amplitude of the total electric field on the face of the coating. A low amplitude of the electric field on of the outermost surface prevents a large amount of dust to be attracted on it, thus reducing the scattering of the radiation incident on the mass. Minimizing the amplitude of the total electric field, viz. $|E_{sur}| = |E_i||1 + \mathcal{R}|$, E_i being the incident electric field, keeping $\mathcal{R}$ unchanged, is tantamount to let the phase of the reflection coefficient $\mathcal{R}$ be as close as possible to π. Figure 6.15 shows the iso-reflectance at $\lambda_1 = 532nm$ and iso-transmittance at $\lambda_0 = 1064nm$ curves, corresponding to the preferred values, in ($\xi_L^{first}, \xi_H^{last}$)-plane, in a neighbourhood of the intersection point, where ξ_L^{first} and ξ_H^{last}, represent the deviation from the QWL thickness of first (low index) and last (high index) layers.

The configuration with minimum $|E_{sur}|$ is searched along a segment belonging to the line tangent at the intersection point to the two curves in Figure 6.15. The segment in centered

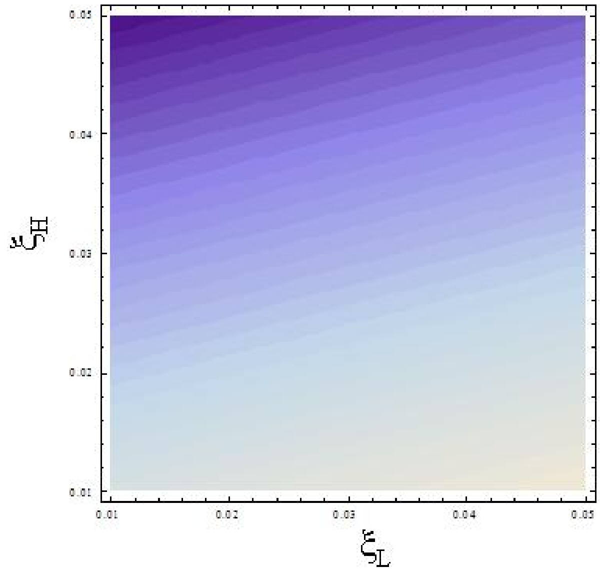

Figure 6.14: Level map of ϕ_{coat} for the dichroic design in the (ξ_L, ξ_H)-plane for 19 doublets. Dark colour implies low value of ϕ_{coat}.

Table 6.5: Parameters of final dichroic optimized design for the ETM coating.

N_D	ξ_L	ξ_H	ξ_L^{first}	ξ_H^{last}	ϕ_{coat}
19	0.0201	0.0294	-0.2286	0.0459	$6.742\ 10^{-9}$

at the same intersection point, and is relatively small , in order to conserve the reflectivity values as close as possible to the preferred values. The trend of $|E_{sur}|$ on this segment is plotted in Figure 6.16, and the configuration reaching its minimum gives the final optimized dochroic design. The parameters are summarized in Table 6.5, the reflectivity spectrum is plotted in Figure 6.17, and Table 6.6 shows the value of the power reflectivity at other potentially interesting wavelengths. The optimization strategy entails a reduction of ϕ_{coat} of about 10% for the ETM coating.

The same strategy has been implemented to derive the minimal noise design for the ITM coating. I used as *preferred* values: 14000 ppm for the power transmittance at the main wavelength (1064 nm) and 0.99 for the power reflectance at the second harmonic (532 nm).

Figure 6.18 shows the curves in the (ξ_L, ξ_H)-plane, in a neighbourhood of the intersection point, where these two constraints are satisfied separately for $N_D = 9$, which is the minimum number of doublets for the AdLIGO specifics to be matched; the intersection points correspond to the acceptable coating configurations where both requirements are satisfied.

Table 6.7 lists the minimal Brownian noise points for different number of doublets, where

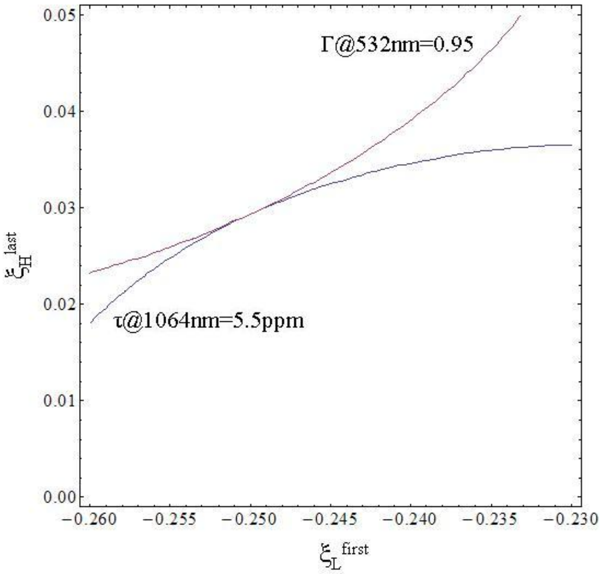

Figure 6.15: Iso-reflectance (0.95 at 532 nm) and iso-transmittance (5.5 ppm at 1064 nm) curves in $(\xi_L^{first}, \xi_H^{last})$-plane of the dichroic design for 19 doublets.

the first row, corresponding to 9 doublets, is the best design.

Even in this case, it is possible to adjust the thicknesses of the two terminal layers, in order to minimize the amplitude of the total electric field at the coating face. Figure 6.19 shows the iso-reflectance at $\lambda_1 = 532nm$ and iso-transmittance at $\lambda_0 = 1064nm$ curves, corresponding to the preferred values, in $(\xi_L^{first}, \xi_H^{last})$-plane, where ξ_L^{first} and ξ_H^{last} represent, as before, the deviation from the QWL thickness of first (low index) and last (high index) layers, according to eq. (6.14).

Figure 6.20 shows the behavior of $|E_{sur}|$ on a segment of the tangent line at both the curves in Figure 6.19 centered at their intersection point. The configuration corresponding

Table 6.6: Reflectivities of ETM optimized dichroic design at the two operation wavelengths and other potentially useful wavelengths.

$\tau@1064nm = 5.59$ppm
$\Gamma@532nm = 0.947$
$\Gamma@670nm = 0.176$
$\Gamma@946nm = 0.996$
$\Gamma@980nm = 0.999$
$\Gamma@1319nm = 0.337$
$\Gamma@1550nm = 0.030$

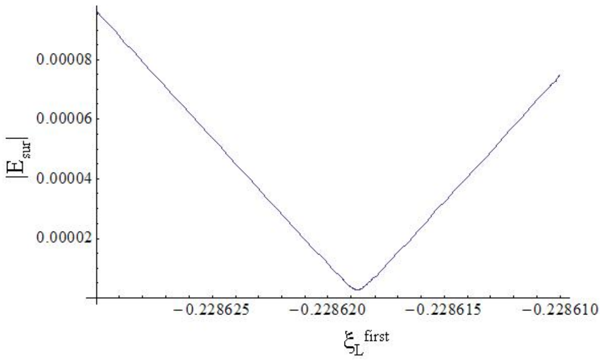

Figure 6.16: Amplitude of the total electric field on top of the ETM coating as function of ξ_L^{first}. ξ_H^{last} is accordingly identified by the equation of the tangent line at the intersection point of the two curves in Figure 6.15.

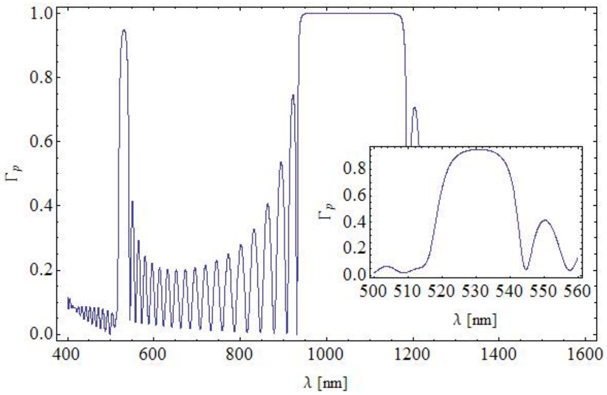

Figure 6.17: Power reflectivity spectrum of dichroic ETM optimized design. A close-up around the second operation wavelength is shown in the inset.

to the minimum of $|E_{sur}|$ is the optimized ITM coating. Its key relevant parameters are summarized in Table 6.8, the reflectivity spectrum is plotted in Figure 6.21, while Table 6.9 shows the values of the power reflectivity at other potentially interesting wavelengths. The optimization strategy entails a reduction of ϕ_{coat} of about 16% for the ITM coating.

Taking into account the noise reductions in all coatings, the reduction in the total interferometer's noise is about 11% and the increase in the event rate is of 19%, with respect to the reference design.

An optimized dichroic prototype for the TNI with parameters as in Table 6.5, has been manufactured by LMA and is presently under test at the Caltech *Thermal Noise Interferometer*. The prototype is a scaled version of the optimised ETM design, where the number of doublets was reduced to 13, to let the power transmittance at $\lambda_0 = 1064nm$ to be as close as possible to the nominal value required for best opertaion of the TNI, i.e. 300ppm. Prelim-

Table 6.7: Minimal Brownian noise points in (ξ_L, ξ_H)-plane for different number of doublets for the ITM design.

N_D	ξ_L	ξ_H	ϕ_{coat}
9	0.0768	0.0907	$2.614\ 10^{-9}$
10	0.0793	0.1026	$2.776\ 10^{-9}$
...	...	...	...

Table 6.8: Parameters of final dichroic optimized design for the ITM coating.

N_D	ξ_L	ξ_H	ξ_L^{first}	ξ_H^{last}	ϕ_{coat}
9	0.0768	0.0907	-0.1952	0.1272	$2.586\ 10^{-9}$

Table 6.9: Reflectivities of ITM optimized dichroic design at the two operation wavelengths and other potentially useful wavelengths.

$\tau@1064nm = 14907\text{ppm}$
$\Gamma@532nm = 0.986$
$\Gamma@670nm = 0.039$
$\Gamma@946nm = 0.913$
$\Gamma@980nm = 0.977$
$\Gamma@1319nm = 0.121$
$\Gamma@1550nm = 0.046$

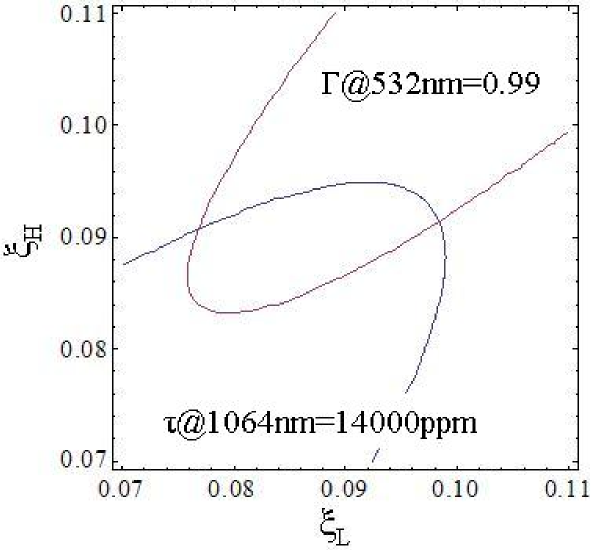

Figure 6.18: Iso-reflectance (0.99 at 532 nm) and iso-transmittance (14000 ppm at 1064 nm) curves in (ξ_L, ξ_H)-plane of the dichroic design for 9 doublets.

inary results, yet unpublished, indicate an excellent agreement with theoretically expected values.

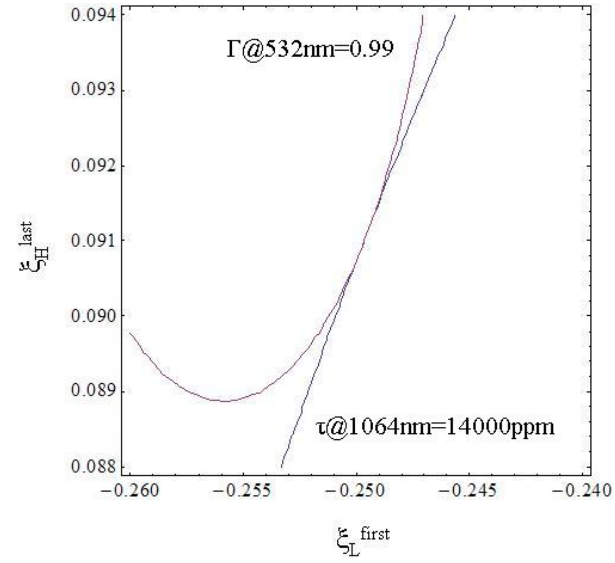

Figure 6.19: Iso-reflectance (0.99 at 532 nm) and iso-transmittance (14000 ppm at 1064 nm) curves in $(\xi_L^{first}, \xi_H^{last})$-plane of the dichroic design for 9 doublets.

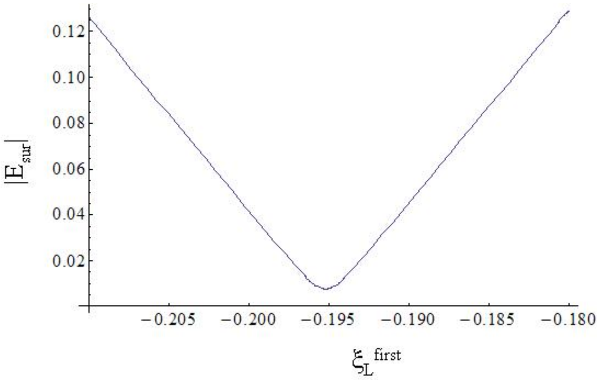

Figure 6.20: Amplitude of the total electric field on top of the ITM coating as function of ξ_L^{first}. ξ_H^{last} is accordingly identified by the equation of the tangent line at the intersection point of the two curves in Figure 6.19.

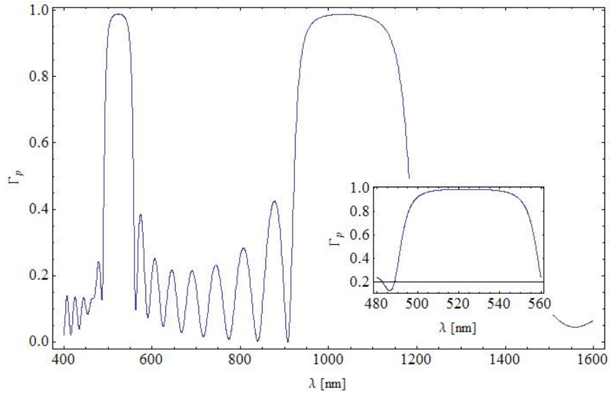

Figure 6.21: Power reflectivity spectrum of dichroic ITM optimized design. A close-up around the second operation wavelength is shown in the inset.

Chapter 7

Conclusions

This thesis summarizes my research work during the three years of my PhD. Within the LIGO-Virgo experiment, I implemented an engineering approach to two important problems in gravitational wave detection experiments based on large baseline optical interferometers. These problems deal with the two sources of noise that presently limit the antennas' sensitivity, i.e. the presence of spurious transient signal, *glitches*, at the output channel due to disturbances of several environmental or instrumental origins, and the thermal noise originated in the test-mass (end-mirror) reflective coatings.

As regards the first issue, I identified as a major limitation for the efficiency of the currently implemented pipelines for Gravitational Waves (GWs) detection the common simplifying assumption that the background noise is Gaussian, even if *data quality flagging* and *event vetoing* are allowed. Indeed, glitches make the noise distinctively non-Gaussian, producing heavier tails in the total noise probability density function. If not properly treated, glitches are detrimental in the search for GW signals, especially for unmodeled GW *Bursts*. Accordingly, I introduced an analytical physically-motivated statistical model for the impulsive component (the glitches), described in Chapter 2, which allowed a more accurate statistical characterization of the total noise in the output (data) channel. An accurate model for the noise is crucial in designing an *optimal* detection strategy, which, I derived in the *weak* signal limit (*local optimality*), in Chapter 3 following two alternative approaches: i) estimating the GWB waveform from the data themselves, yielding the *generalized likelihood ratio* test, GLRT; and ii) modeling the GWB waveform as a random process, yielding the *generalized cross-correlation* test, GCC. In Chapter 4 the detection performance of the proposed strategies are evaluated in simulated glitch noise, first, and, then, in real LIGO data. Numerical simulations show clearly the effectiveness of the proposed approach in improving the detection efficiency in the presence of glitches. The GCC statistic turns out to outperform the GLRT in non-Gaussian noise. These results are corroborated by numerical evaluations on a bunch of S5 real LIGO noise. I further modified, according to the locally optimum approach, one of the existing pipelines (the RIDGE pipeline) for the detection of GWBs, and compared the performance of the modified and the unmodified statistics. The former outperform the latter, confirming the effectiveness of the proposed method and the fact that the instrument noise is essentially non-Gaussian, even in high-quality non-vetoed data segments.

Thermal noise originated in the reflctive coatings of the interferometer test mass end-mirrors turns out to limit the instrument sensitivity in the observationally most important spectral band, as discussed in Chapter 5. Hence, the coating optimization is a crucial issue. The originally proposed coating designs, based on the Bragg (quarter-wavelength) multilayer structure, do not achieve the minimum of thermal noise under the AdLIGO prescribed reflectances. In Chapter 6 I formulated an optimization strategy to design coatings, achieving the minimum of thermal noise for a prescribed reflectance. Such a strategy was formulated first for single-wavelength operation, and it has been adopted to design coatings for the *Thermal Noise Interferometer* (TNI), a small-scale interferometer built at Caltech. The coating has been then prototyped by the *Laboratoires des Materiaux Avances* (LMA), Lyon FR, and tested at Caltech using the Thermal Noise Interferometer (TNI) facility. The measured reduction in the coating thermal noise level, compared to the Bragg configuration, was in excellent agreement with theoretical predictions.
The optimization strategy was further extendend to the double-wavelength operation case, required by the new AdLIGO cavity locking system. Compared to the initially proposed *dichroic* design, made by a stack of two cascaded Bragg multilayer structures operating at the two design wavelengths, the optimized design achieved a thermal noise reduction of about 10% for the *end* test masses and 6% for *inner* test masses, resulting in a total interferometer noise reduction of 11% and a consequent boost in the event rate of 18%. A dichroic prototype has been also manufactured by LMA and its noise properties are currently under test at Caltech.

References

[1] http://auriga9.lnl.infn.it/IGEC2/.

[2] http://www.ligo.caltech.edu.

[3] http://www.virgo.infn.it.

[4] http://www.geo600.uni-hannover.de.

[5] http://tamago.mtk.nao.ac.jp.

[6] http://gw.icrr.u-tokyo.ac.jp/lcgt.

[7] http://www.et-gw.eu/.

[8] www.lisa.nasa.gov.

[9] http://www.einsteinathome.org/.

[10] A general formula for thermo-refractive noise coefficient of stacked-doublet mirror coatings. *LIGO Technical Report LIGO-T070159-00-Z*, 2007.

[11] Bilenko I A and Lyaskovskaya N Yu. The investigation of thermal and non-thermal noises in fused silica fibers for advanced ligo suspension. *Phys Lett A*, 339:181, 2005.

[12] Bilenko N A and Lyaskovskaya N Yu. The investigation of thermal and non-thermal noises in advanced ligo suspension prototype. *Phys. Lett. A*, 339:181–187, 2004.

[13] Buonanno A and Chen Y. Improving the sensitivity to gravitational-wave sources by modifying the input-output optics of advanced interferometers. *Phys Rev D*, 69:102004, 2004.

[14] Einstein A. On the electrodynamics of moving bodies. 1905.

[15] Gillespie A and Raab F. Thermally excited vibrations of the mirrors of laser interferometric gravitational-wave detectors. *Phys. Rev D*, 52:577–585, 1995.

[16] Kassam S A. Locally robust array detectors for random signals. *IEEE Trans Info Theory*, 24:209, 1978.

[17] Kassam S A. *Signal Detection in Non-Gaussian Noise*. Springer-Verlag, 1988. ISBN 0-387-96680-3.

[18] Kassam S A and Thomas B. *Benchmark Papers in Electrical Engineering and Computer*. New York Academic, vol. 23, 1980. Non-parametric Detection, Theory and Application.

[19] Postnov K A and Yungelson L R. The evolution of compact binary star systems. *Living Rev Relativity*, 9:6, 2006. http://www.livingreviews.org/lrr-2006-6.

[20] Savitsky A and Golay M J E. Smoothing and differentiation of data by simplified least squares. *Anal Chem*, 36:1627–1639, 1964.

[21] Sihvola A. *Electromagnetic Mixing Formulas and Applications*. The Institution of Electrical Engineers, London, United Kingdom, 1999.

[22] Ballmer S Adhikari R and Fritschel P. Interferometer sensing and control design requirements. *LIGO-T070236-00-D*, 2008.

[23] Sintes AM and Schutz B F. Coherent line removal: Filtering out harmonically related line interference from experimental data, with application to gw detectors. *Phys Rev D*, 58:122003, 1998.

[24] Braginsky V B and Vyatchanin S P. Thermodynamical fluctuations in optical mirror coatings. *Phys Lett A*, 312:244–255, 2003.

[25] Callen H B and Welton. Irreversibility and generalized noise. *Phys. Rev.*, 83:34, 1951.

[26] Roberts J B. Distribution of the responses of linear systems to poisson distributed random pulses. *Journal of Sound & Vibration*, 28:93–103, 1973.

[27] Seyfe B and Sharafat A R. Signed-rank nonparametric multiuser detection in non-gaussian channels. *IEEE Trans Info Theory*, 51:1478–1486, 2005.

[28] Thomas J B. Nonparametric detection. *Proc. IEEE*, 58:623, 1970.

[29] Hello P Bondu F and Vinet J Y. Thermal noise in mirrors of interferometric gravitational wave antennas. *Phys Lett A*, 246:227–236, 1998.

[30] Gorodetsky M L Braginsky V B and Vyatchanin S P. Thermodynamical fluctuations and photo-thermal shot noise in gravitational wave antennae. *Phys Lett A*, 264:1–10, 1999.

[31] Gorodetsky M L Braginsky V B and Vyatchanin S P. Thermo-refractive noise in gravitational wave antennae. *Phys Lett A*, 271:303–307, 2000.

[32] MacKay D J C. *Information Theory, Inference, and Learning Algorithms*. 2003. http://www.inference.phy.cam.ac.uk/mackay/itila/.

[33] Lee CC and Longley L A. Nonparametric estimation algorithms based on input quantization. *IEEE Trans*, IT-31:682, 1985.

[34] Chatterji. http://ldas-jobs.ligo-wa.caltech.edu/ qonline/.

[35] personal communication CSIRO.

[36] Creighton J D. Data analysis stretegies for the detection of gravitational waves in non-gaussian noise. *Phys Rev D*, 60:021101, 1999.

[37] Gabor D. Theory of communication. *J Inst Electrical Eng*, 93:429, 1946.

[38] Kontorovich D and Lyandrev B. Impulsive noise: a non-traditional approach. *Signal Processing*, 51:121, 1996.

[39] Martin R D and Schwartz S C. Robust detection of a known signal in nearly gaussian noise. *IEEE Trans*, IT-17, 1971.

[40] Middleton D. On the theory of random noise. phenomenological models. *J Appl Phys*, 22:1143, 1951. ; ibid. 22:1326, 1951; ibid. 22:1153, 1951.

[41] Middleton D. Man-made noise in urban environments and transportation systems: Models and measurements. *IEEE Trans Comm*, COM-21:1232–1241, 1973.

[42] Mohanty S D. Robust test for detecting nonstationarity in data from gravitational wave detectors. *Phys Rev D*, 61:122001, 2000.

[43] Mohanty S D. Variability of signal-to-noise ratio and the network analysis of gravitational wave burst signals. *Class Quantum Grav*, 23:4799, 2006.

[44] Font J Dimmelmeier H and Muller E. Relativistic simulations of rotational core collapse 2. collapse dynamics and gravitational radiation. *Astron Astrophys*, 393:523, 2002.

[45] Chassande-Mottin E and Dhurandhar S V. Adaptive filtering techniques for gravitational wave interferometric data: Removing long-term sinusoidal disturbances and oscillatory transients. *Phys Rev D*, 63:042004, 2001.

[46] Flanagan E and Hughes S A. Measuring gravitational waves from binary black hole coalescences. ii. the waves' information and its extraction, with and without templates. *Phys Rev D*, 57:4566, 1988.

[47] Swaszek P F Efron A J and Tufts D W. Detection in correlated gaussian plus impulsive noise. *IEEE Trans. Aerosp. Electr. Systems*, 28:932–943, 1992.

[48] Abbot N et al. Upper limits on gravitational wave bursts in ligo's second science run. *Phys Rev D*, 72:062001, 2005.

[49] Agresti J et al. Optimized multilayer dielectric mirror coatings for gravitational wave interferometers. *Proc. SPIE*, 6286:628608–628617, 2006.

[50] Ajith P et al. Robust vetoes for gravitational-wave burst triggers using known instrumental couplings. *Class Quantum Grav*, 23:5825, 2006.

[51] Ajith P et al. A phenomenological template family for black-hole coalescence waveforms. *Class Quantum Grav*, 24:S689, 2007.

[52] Allen B et al. Robust statistics for deterministic and stochastic gravitational waves in non-gaussian noise. 1: Frequentist analyses. *Phys. Rev. D*, 65:122002, 2002.

[53] Allen B et al. Robust statistics for deterministic and stochastic gravitational waves in non-gaussian noise. 2: Bayesian analyses. *Phys. Rev. D*, 67:122002, 2003.

[54] Anderson W G et al. An excess power statistic for detection of bursts sources of gravitational radiation. *Phys Rev D*, 63:042003, 2001.

[55] Arnaud N et al. Detection in Coincidence of Gravitational Wave Bursts with a Network of Interferometric Detectors: Geometric Acceptance and Timing. *Phys Rev D*, 65:042004–042017, 2002.

[56] Arnaud N et al. Coincidence and coherent data analysis methods for gravitational wave bursts in a network of interferometric detectors. *Phys Rev D*, D68:102001, 2003.

[57] Bertero M et al. Linear inverse problems with discrete data: I. general formulation and singular system analysis. *Inverse Problems*, 1:300, 1985.

[58] Bertero M et al. Linear inverse problems with discrete data: Ii. stability and regularisation. *Inverse Problems*, 4:573, 1988.

[59] Black E D et al. Direct observation of broadband coating thermal noise in a suspended interferometer. *Phys Lett A*, 328:1–5, 2004.

[60] Blackburn L et al. The lsc glitch group: Monitoring noise transients during the fifth ligo science run. *Class Quantum Grav*, 25:18404, 2008.

[61] Cagnoli G et al. Mechanical shot noise induced by creep in suspension devices. *Phys Lett A*, 271:37, 2002.

[62] Cerdonio M et al. Wideband dual sphere detector of gravitational waves. *Phys Rev Lett*, 87:031101, 2001.

[63] Chatterji et al. Coherent network analysis technique for discriminating gw bursts from instrumental noise. *Phys Rev D*, 74:082005, 2006.

[64] Chatterji S et al. Multiresolution Techniques for the Detection of Gravitational-Wave Bursts. *Class. Quantum Grav.*, 21:S1809, 2004.

[65] Comtet C et al. Reduction of tantala mechanical losses in ta2o5/sio2 coatings for the next generation of virgo and ligo interferometric gravitational waves detectors. *Proc. Recontre de Moriond*, March 2007.

[66] Dimmelmeier H et al. Generic gravitational-wave signals from the collapse of rotating stellar cores. *Phys Rev Lett*, 98:251101, 2007.

[67] Evans M et al. Thermo-optic noise in coated mirrors for high-precision optical measurements. *Phys Rev D*, 78:102003–102013, 2008.

[68] Gehrels N et al. The swift gamma-ray burst mission. *Astrophys J*, 611:1005, 2005.

[69] Harry G et al. Thermal noise in interferometric gravitational wave detectors due to dielectric coatings. *Class. Quantum Grav.*, 19:897–917, 2002.

[70] Harry G et al. Thermal noise from optical coatings in gravitational wave detectors. *App Opt*, 45:1569–1574, 2006.

[71] Harry G et al. Titania-doped tantala/silica coatings for gravitational-wave detection. *Class. Quantum Grav.*, 24:405–415, 2007.

[72] Hayama K et al. Coherent network analysis for triggered gravitational wave burst searches. *Class Quantun Grav*, 24:S681, 2007.

[73] Hayama K et al. Searches for gravitational waves associated with pulsar glicthes using a coherent network algorithm. *Class Quantum Grav*, 25:184016, 2008.

[74] Kaaret P et al. http://arxiv.org/abs/astro-ph/0611716.

[75] Klimenko S et al. Constraint likelihood analysis for a network of gravitational wave detectors. *Phys Rev D*, 72:122002–122015, 2005.

[76] Klimenko S et al. A coherent method for detection of gravitational wave bursts. *Class Quantum Grav*, 25:114029, 2008.

[77] Manchester R N et al. The atnf pulsar catalogue. *Astron J*, 129:1993–2006, 2005. arXiv: astro-ph/0412641.

[78] Marano S et al. Distributed estimation in large wireless sensor networks via a locally optimum approach. *IEEE Trans*, SP-56:748, 2008.

[79] Maronna R et al. *Robust Statistics: Theory and Methods*. Wiley, NY, 2006.

[80] McNabb J et al. Overview of the blocknormal event trigger generator. *Class. Quantum Grav.*, 21:S1705, 2004.

[81] Miyoki S et al. Status of clio project. *Class Quantum Grav*, 21:S1173, 2004.

[82] Nagakawa N et al. Thermal noise in half-infinite mirrors with uniform loss: A slab of excess loss in a half-infinite mirror. *Phys. Rev D*, 62:102001, 2001.

[83] Ott C et al. Gravitational waves from axisymmetric, rotational stellar core collapse, 2004.

[84] Principe M et al. Minimal noise coatings with sub-wavelength sandwiched dielectrics. *LIGO-G0900880*, 2009.

[85] Scott S M et al. Caltech 40m interferometer characterisation: Spectral properties of the data. *LIGO Scientific Collaboration Meeting*, 1999.

[86] Summerscales T Z et al. Maximum entropy for gravitational wave data analysis: Inferring the physical parameters of core-collapse supernovae. *Astrophys J*, 678:1142, 2008.

[87] Urmanov A M et al. Information complexity-based regularization parameter selection for solution of ill-conditioned inverse problems. *Inverse Problems*, 18:L1, 2002.

[88] Villar A et al. Measurement of thermal noise in multilayer coatings with optimized layer thickness. *Phys. Rev D*, 81:122001, 2010.

[89] Schutz B F and Sathyaprakash B S. Templates for stellar mass black holes falling into supermassive black holes. *Class Quantum Grav*, 20:S209, 2003.

[90] Gonzalez G. Suspensions thermal noise in the ligo gravitational wave detector. *Class. Quantum Grav.*, 17:4409–4436, 2000.

[91] Cramr H. *Mathematical Methods of Statistics.* Princeton University Press, Princeton, 1957.

[92] Hurwitz H and Kac M. Statistical analysis of certain types of random functions. *Ann Math Stat*, 15:173, 1944.

[93] Santamore D H and Levin Y. Eliminating thermal violin spikes from ligo noise. *Phys Rev D*, 64:042002, 2001.

[94] Taylor J H. Binary pulsar and relativistic gravity. *Nobel Lecture in Physics*, December 1993. Princeton University, NJ, USA.

[95] Willet P K Han C and Abraham D A. Some methods to evaluate the performance of page's test as used to detect transient signals. *IEEE Trans. on Signal Process*, SP-47:2112, 1999.

[96] Helstrom. *Statistical Theory of Signal Detection.* Pergamon Press, London, 1968.

[97] http://ilog.ligo wa.caltech.edu:7285/advligo/GWINC.

[98] Achieser N I. *Theory of Approximation.* Frederic Ungar, New York, 1956. translated by C. T. Hyman.

[99] Gonzalez G I and Saulson P R. Brownian motion of a mass suspended by an anelastic wire. *J Acoust Soc Am*, 96:207–212, 1994.

[100] Bastiaans M J. Gabors expansion of a signal into elementary gaussian signals. *Proc. IEEE*, 68:538, 1980.

[101] Huber P J. Robust estimation of a location parameter. *Ann. Math. Stat.*, 35:73, 1964.

[102] Orfanidis S J. *Electromagnetic Waves and Antennas.* 2008. http://www.ece.rutgers.edu/ orfanidi/ewa/.

[103] Owen B J. Detectability of periodic gravitational waves by initial interferometers. *Class Quantum Grav*, 23:S1, 2006.

[104] Sylvestre J. Optimal generalization of power filters for gravitational wave bursts from single to multiple detectors. *Phys Rev D*, 68:102005, 2003.

[105] Weber J. Detection and generation of gravitational waves. *Phys Rev*, 117:306, 1960.

[106] Sarkar T Jain V and Weiner D. Rational modeling by pencil-of-functions method. *IEEE Trans. on Acoustic, Speech and Signal Processing*, ASSP-6:897, 1981.

[107] Richter W J Jr. and Smits T I. Numerical evaluation of rices integral representation of the probability density function for posisson impulse noise. *J Acoust Soc Am*, 56:481–496, 1974.

[108] Somiya K and Yamamopto K. Coating thermal noise of a finite-size cylindrical mirror. *Phys Rev D*, 79:102004, 2009.

[109] Thorne K. Gravitational waves. *CaltechWeb Course*, 2002. http://elmer.tapir.caltech.edu/ph237/.

[110] Blanchet L. http://www.livingreviews.org/lrr-2006-4.

[111] Cadonati L and Marka S. Corr-power: a cross-correlation based algorithm for triggered and untriggered gw bursts. *Class Quantum Grav*, 22:S1159, 2005.

[112] Kimball A L. Internal friction theory of shaft whirling. *Phys Rev*, 21:701–703, 1923.

[113] Van Blaricum M L and Mittra R. Problems and solutions associated with prony's method for processing transient data. *IEEE Trans. on Antennas and Prop*, AP-26:174, 1978.

[114] Basseville M and Nikiforov I V. *Detection of Abrupt Changes, Theroy and Applications.* Prentice-Hall Inc., 1993.

[115] Born M and Wolf E. *Principles of Optics: Electromagnetic Theory of Propagation, Intereference and Diffraction of Light.* Cambridge University Press, 7th edition, 2005.

[116] Maggiore M. http://xxx.lanl.gov/abs/gr-qc/0008027v1.

[117] Maras A M. Threshold parameter estimation in nonadditive non-gaussian noise. *IEEE Trans*, SP-45:682, 1997.

[118] Principe M and Pinto I M. Modeling the impulsive noise component and its effect on the operation of a simple coherent network algorithm for unmodeled gravitational wave burst detection. *Class Quantum Grav*, 25:075013, 2008.

[119] Principe M and Pinto I M. Detecting unmodeled gw bursts in non-gaussian (glitchy) noise: Two locally optimum network detectors. *Class Quantum Grav*, 26:204001, 2009.

[120] Principe M and Pinto I M. Locally optimum network detection of unmodelled gravitational wave bursts in an impulsive noise background. *Class Quantum Grav*, 26:045003, 2009.

[121] Rakhmanov M. Rank deficiency and tikhonov regularization in the inverse problem for gravitational-wave bursts. *Class Quantum Grav*, 23:S673, 2006.

[122] Rakhmanov M and Klimenko S. A cross-correlation method for burst searches with networks of misaligned gravitational-wave detectors. *Class Quantum Grav*, 22:S1311, 2005.

[123] Sintes A M and Schutz B F. Removing nonstationary nonharmonic external interference from gravitational wave interferometer data. *Phys Rev D*, 60:062001, 1999.

[124] Unser M. On the approximation of the discrete karhunen-loeve transform for stationary processes. *Signal Processing*, 7:231–249, 1984.

[125] Zabin S M and Wright G A. Nonparametric density estimation and detectionin impulsive interference channels. part 1: Estimators. *IEEE Trans Comm*, COM-42, 1994.

[126] Thorne K S Misner C W and Wheeler J. *Gravitation.* W H Freema & Company, San Francisco (USA), 1973.

[127] Rice S O. Mathematical analysis of random noise. *Bell Syst Tech J*, 23:282–332, 1944.

[128] Comon P. Independent component analysis, a new concept. *Signal Processing*, 36:287–314, 1994.

[129] Jaranovski P and Krolak A. Optimal solution to the inverse problem for the gravitational wave signal of a coalescing compact binary. *Phys Rev D*, 49:1723, 1994. ibid. D58:063001, 1998; ibid. D59:063003, 1999; ibid. D61:062001, 2000.

[130] Saulson P. *Fundamentals of Interferometric GW Detectors*. World Scientific, Singapore, 1994.

[131] Saulson P. Listening to glitches. *LIGO-G070548-00-Z*, 2007.

[132] Cox D R and Isham V. *Point Processes*. CHAPAN AND HALL/CRC, 1980.

[133] Penrose R. A generalized inverse for matrices. *Proc Cambridge Phil Soc*, 51:406, 1955.

[134] Saulson P R. Thermal noise in mechanical experiments. *Phys Rev D*, 42:2437–2445, 1990.

[135] Viswanathan R and Varshney P K. Distributed Detection with Multiple Sensors: Part I - Fundamentals. *Proc IEEE*, 86:54–63, 1997.

[136] Heng I S. Rotating stellar core-collapse waveform decomposition: a principal component analysis approach. *Class Quantum Grav*, 26:105005, 2009.

[137] Kawamura S. The japanese space gravitational wave antenna - decigo. *LIGO-G060318-00-Z*, 2006.

[138] Klimenko S and Mitselmakher G. A wavelet method for detection of gravitational wave burst. *Class Quantum Grav*, 21:S1819, 2004.

[139] Mukherjee S. Median-based noise floor tracker (mnft): Robust estimation of noise floor drifts in interferometric data. *Class Quantum Grav*, 20:S925, 2003.

[140] Mukherjee S. Preliminary results from the hierarchical glitch pipeline. *Class Quantum Grav*, 24:S701, 2007.

[141] Mukherjee S and Finn L S. Data conditioning for gravitational wave detectors: A kalman filter for regressing suspension violin modes. *Phys Rev D*, 63:062004, 2001.

[142] Rao S. *Mirror Thermal Noise in Interferometric Gravitational Wave Detectors*. PhD thesis, Caltech, 2003.

[143] Liu Y t and Thorne K S. Thermoelastic noise and homogeneous thermal noise in finite size gravitational-wave test masses. *Phys. Rev D*, 62:122002–1220012, 2000.

[144] Zwerger T and Muller E. Dynamics and gravitational wave signature of axisymmetric rotational core collapse. *Astron. Astrophys.*, 320:209, 1997.

[145] Advanced LIGO Team. Advanced ligo reference design. *LIGO-M060056-v1*, 2009.

[146] Advanced LIGO team. Advanced ligo reference disegn. *LIGO-M060056-v1*, 2009.

[147] D'Agostino R V and Stephens M A. *Goodness of Fit Techniques*. Marcel Dekker, New York, 1986.

[148] Poor H V. Signal detection in the presence of weakly dependent noise-part 1: Optimum detection. *IEEE Trans. Inform. Theory*, IT-28:735–744, 1982.

[149] Helstrom C W. An expansion of a signal in gaussian elementary signals. *IEEE Trans.*, IT-12, 1966.

[150] Gursel Y and Tinto M. Near optimal solution to the inverse problem for gravitational-wave bursts. *Phys Rev D*, 40:3884, 1989.

[151] Levin Y. Internal thermal noise in the ligo test masses: A direct approach. *Phys. Rev. D*, 57:659–663, 1998.

[152] Rahmat-Samii Y and Michiessen E. *Electromagnetci Optimization by Genetic Algorithms*. J Wiley & Sons, 1999.

[153] Rice S O Yue O, Lugannani R. Series approximation for the amplitude distribution and density of shot processes. *IEEE Trans Comm*, COM-26:45–54, 1978.

Appendix A

Derivation of the GCC detection statistic

The derivation of the Generalized Cross-Correlation (GCC) statistic is derived in detail in this Appendix. It is based on the assumption that the sough GW signal is a random process, with minimal a priori assumption.

In this Appendix we summarize the derivation of the Generalized Cross-Correlation statistic, following Kassam [17].

In the hypotheses test in eq. (3.1) we assume: i) that the noise samples, $\mathbf{n}_d(k) = n_d(t_k)$, $\forall k = 1, \ldots, N_s$, are i.i.d. with probability density functions, $f_n^{(d)}(x)$ featuring zero mean and variance σ_n^2; ii) each of the two GW polarization components, $\mathbf{h}_+$ and $\mathbf{h}_\times$, is a random process; iii) the GW signal and the noise process are independent. iv) $f_n^{(d)}(\cdot)$ is regular enough to allow the results to be valid. Under these assumptions the PDF of the output data matrix $\mathcal{V} = \{\mathbf{V}_1, \ldots, \mathbf{V}_D\}$ in the two hypotheses can be written as

$$\begin{cases} H_0 : \; f_{\mathcal{V}}(\mathcal{V}) = \displaystyle\prod_{k=1}^{N_s} \prod_{d=1}^{D} f_n^{(d)}(V_{dk}) \\ \\ H_1 : \; f_{\mathcal{V}}(\mathcal{V}|\theta) = E\left[\displaystyle\prod_{k=1}^{N_s} \prod_{d=1}^{D} f_n^{(d)}(V_{dk} - \theta S_{dk})\right], \; \theta \neq 0 \end{cases}, \tag{A.1}$$

where the expectation $E[\cdot]$, here and henceforth, is taken with respect to the random GW polarization components. Let

$$P(\theta) = \prod_{k=1}^{N_s} \prod_{d=1}^{D} f_n^{(d)}(V_{dk} - \theta S_{dk}) \tag{A.2}$$

whence

$$f_{\mathcal{V}}(\mathcal{V}) = P(0), \quad f_{\mathcal{V}}(\mathcal{V}|\,\theta) = E\left[P(\theta)\right]. \tag{A.3}$$

To obtain the LO detection statistic, we must differentiate $f_{\mathcal{V}}(\cdot|\theta)$ with respect to θ, and evaluate it at $\theta = 0$. The derivative of $f_{\mathcal{V}}(\mathcal{V}|\,\theta)$ is

$$\frac{d}{d\theta}\, f_{\mathcal{V}}(\mathcal{V}|\,\theta) = E\left[\frac{dP(\theta)}{d\theta}\right] = \\ -E\left[\sum_{k=1}^{N_s} \sum_{d=1}^{D} P(\theta) \frac{f_n^{(d)\prime}(V_{dk} - \theta S_{dk})}{f_n^{(d)}(V_{dk} - \theta S_{dk})} S_{dk}\right], \tag{A.4}$$

which for $\theta = 0$ becomes

$$\left.\frac{d}{d\theta}\, f_{\mathcal{V}}(\mathcal{V}|\,\theta)\right|_{\theta=0} = -P(0) \sum_{k=1}^{N_s} \sum_{d=1}^{D} E[S_{dk}] \frac{f_n^{(d)\prime}(V_{dk})}{f_n^{(d)}(V_{dk})}. \tag{A.5}$$

The LO test statistic is thus

$$\frac{d}{d\theta} ln f_n(\mathcal{V})\Big|_{\theta=0} = \frac{\frac{d}{d\theta}\, f_{\mathcal{V}}(\mathcal{V}|\,\theta)\big|_{\theta=0}}{f_{\mathcal{V}}(\mathcal{V})} = \sum_{k=1}^{N_s}\sum_{d=1}^{D} E[S_{dk}]\, g_{LO}^{(d)}(V_{dk}), \tag{A.6}$$

the $g_{LO}(\cdot)$ function being defined in eq. (3.8). This result has the same structure of the LO statistic in the case of deterministic signal, exept that its amplitude has been replaced with the expected value. We make no a priori assumption about the sought GW signal except that:

$$\begin{array}{l} E\left[S_{dk}\right] = 0,\ \forall d = 1, \ldots, D\ \forall k = 1, \ldots, N_s \\ \\ E\left[S_{dk} S_{pm}\right] = \mathcal{R}_{dp} \delta_{k-m},\ \forall d, p = 1, \ldots, D\ \forall k, m = 1, \ldots, N_s \end{array} . \tag{A.7}$$

This results in an identically null first order LO statistic (A.6). In this case, according to the generalization of the Neymann-Pearson lemma [17], the LO detection statistic is the one maximizing the second-order derivative of the power function of the test in $\theta = 0$, viz.

$$\frac{\frac{d^2}{d\theta^2}\ f_{\mathcal{V}}(\mathcal{V}|\theta)|_{\theta=0}}{f_{\mathcal{V}}(\mathcal{V}|\theta = 0)} > \eta. \tag{A.8}$$

The second order derivative of $f_{\mathcal{V}}(\mathcal{V}|\,\theta)$ with respect to θ computed from eq. (A.4), and evaluated in $\theta = 0$, yields

$$\begin{aligned} \frac{d^2}{d\theta^2} f_{\mathcal{V}}(\mathcal{V}|\theta)\Big|_{\theta=0} &= P(0) \sum_{k=1}^{N_s}\sum_{d=1}^{D} E[S_{dk}^2] \frac{f_n^{(d)}{}''(V_{dk})}{f_n^{(d)}(V_{dk})} + \\ +P(0) \sum_{k=1}^{N_s}\sum_{d=1}^{D} \overset{(p,m)\neq(d,k)}{\sum_{m=1}^{N_s}\sum_{p=1}^{D}} & E[S_{dk} S_{pm}] \frac{f_n^{(d)}{}'(V_{dk})}{f_n^{(d)}(V_{dk})} \frac{f_n^{(d)}{}'(V_{pm})}{f_n^{(d)}(V_{pm})}. \end{aligned} \tag{A.9}$$

Hence in view of (A.7), we get

$$\begin{aligned} \frac{d^2}{d\theta^2} f_{\mathcal{V}}(\mathcal{V}|\theta)\Big|_{\theta=0} &= P(0) \sum_{k=1}^{N_s}\sum_{d=1}^{D} E[S_{dk}^2] \frac{f_n^{(d)}{}''(V_{dk})}{f_n^{(d)}(V_{dk})} + \\ P(0) \sum_{k=1}^{N_s}\sum_{d=1}^{D} & \overset{p\neq d}{\sum_{p=1}^{D}} \mathcal{R}_{dp} \frac{f_n^{(d)}{}'(V_{dk})}{f_n^{(d)}(V_{dk})} \frac{f'(V_{pk})}{f(V_{pk})}, \end{aligned} \tag{A.10}$$

which, upon substitution in eq. (A.8), gives back the LO detection statistic in eq. (3.34).

Appendix B

Thermo-Refractive Noise in non-QWL Coatings

The formula proposed by Bragisky and co-workers for the effective coating thermo-refractive coefficient in the case of periodic QWL coating, is extended in this Appendix to the more general case of periodic non-QWL coating, i.e. where the identical stacked doublets consist of layers of arbitrary thicknesses.

Following Braginsky et al. in [31], and assuming a TEM incidence and a $exp(\imath\omega t)$ dependence on time, I introduce the (dimensionless) transmission matrix relating the transverse components of the electric and magnetic field at the input and output faces of a low-high index doublet, viz.

$$\begin{bmatrix} E_{out} \\ Z_0 H_{out} \end{bmatrix} = \begin{bmatrix} \Theta_{11} & \Theta_{12} \\ \Theta_{21} & \Theta_{22} \end{bmatrix} \begin{bmatrix} E_{in} \\ Z_0 H_{in} \end{bmatrix}, \; i = M, M-1, \ldots, 1, \tag{B.1}$$

where [102]

$$\begin{gathered} \Theta_{11} = cos\delta_H cos\delta_L - (n_H/n_L) sin\delta_H sin\delta_L, \\ \Theta_{12} = -\imath(n_H^{-1} sin\delta_H cos\delta_L + n_L^{-1} sin\delta_L cos\delta_H), \\ \Theta_{21} = -\imath(n_H sin\delta_H cos\delta_L + n_L sin\delta_L cos\delta_H), \\ \Theta_{22} = cos\delta_H cos\delta_L - (n_H/n_L) sin\delta_H sin\delta_L, \end{gathered} \tag{B.2}$$

having defined

$$\delta_{L,H} = \frac{2\pi}{\lambda_0} n_{L,H} l_{L,H} \tag{B.3}$$

the phase thicknesses of the low/high index layers. To first order in the temperature fluctuations, one has

$$n_{L,H} = n_{L,H}^{(0)} + \beta_{L,H}^{(0)} \Delta T, \tag{B.4}$$

and[1]

$$\delta_{L,H} = \frac{2\pi}{\lambda_0} n_{L,H}^{(0)} l_{L,H}^{(0)} \left[1 + \frac{\beta_{L,H}^{(0)}}{n_{L,H}^{(0)}} \Delta T \right], \tag{B.5}$$

where $\beta_{L,H} = dn_{L,H}/dT$ are the thermo-refractive coefficients of the coating materials. In eqs. (B.4) and (B.5) the superfix (0) denotes the values at the reference temperature T_0.

The key idea behind Braginsky and co-workers for computing the coating effective thermo-refractive coefficient β_{eff}, is that the input admittance[2] Y of a highly reflective coating, which consists of a high large number of identical doublets, does not change sensibly upon the addition of a further doublet, so that

---

[1] In eq. (B.5) only the thermo-refractive noise component is taken into account, ignoring the thermo-elastic one, which would yield in $\delta_{L,H}$ the additional term $2\pi n_{L,H}^{(0)} l_{L,H}^{(0)} \alpha_{L,H} \Delta T$, where $\alpha_{L,H}/\lambda_0$ is the linear expansion coefficient, defined in eq. (5.16).

[2] This must not be confused with the elastic Young's modulus introduced in Chapter 5.

$$\frac{Z_0 H_{in}}{E_{in}} = \frac{Z_0 H_{out}}{E_{out}} = Z_0 Y = \overline{Y}. \tag{B.6}$$

This is strictly the case, obviously, only for coatings with infinite number of doublets. However, for transmittance as low as planned for AdLIGO, the (normalized) input admittance computed using eqs. (B.6) and (B.1) matches the exact one to more than five decimal digits, which is enough for our present purpose[3]. Using eqs. (B.4) and (B.5) in eq. (B.2), one obtains

$$\Theta_{ij} = \Theta_{ij}^{(0)} + \Delta\Theta_{ij},\ i,j = 1,2. \tag{B.7}$$

Expanding $\overline{Y}$ to first order in ΔT,

$$\overline{Y} = \overline{Y}^{(0)} + \Delta\overline{Y}, \tag{B.8}$$

and using eqs. (B.7) in (B.6) and (B.1), one readily obtains

$$\Theta_{12}^{(0)}(\overline{Y}^{(0)})^2 + (\Theta_{11}^{(0)} - \Theta_{22}^{(0)})\overline{Y}^{(0)} + \Theta_{21}^{(0)} = 0, \tag{B.9}$$

and

$$\Delta\overline{Y} = \frac{\Delta\Theta_{21} + \overline{Y}^{(0)}(\Delta\Theta_{22} - \Delta\Theta_{11}) - (\overline{Y}^{(0)})^2\Delta\Theta_{12}}{\Theta_{11}^{(0)} - \Theta_{22}^{(0)} + 2\overline{Y}^{(0)}\Theta_{12}^{(0)}}. \tag{B.10}$$

Equation (B.9) has two roots, but the only one satisfying the physical requirement of vanishing in the limit where $z_L = z_H \to 1/4$ is

$$\overline{Y}^{(0)} = \frac{-(\Theta_{11}^{(0)} - \Theta_{22}^{(0)}) + \sqrt{(\Theta_{11}^{(0)} - \Theta_{22}^{(0)})^2 + 4\Theta_{12}^{(0)}\Theta_{21}^{(0)}}}{2\Theta_{12}^{(0)}}. \tag{B.11}$$

Neglecting optical losses, both $\overline{Y}^{(0)}$ and $\Delta\overline{Y}$ are purely imaginary, viz.

$$\overline{Y}^{(0)} = \imath\overline{B}^{(0)},\ \Delta\overline{Y} = \imath\Delta\overline{B}. \tag{B.12}$$

The coating reflection coeffcient is accordingly given, to first order in ΔT, by

$$\mathcal{R} = \frac{1-\overline{Y}}{1+\overline{Y}} = \frac{1-\imath\overline{B}^{(0)} - \imath\Delta\overline{B}}{1+\imath\overline{B}^{(0)} + \imath\Delta\overline{B}} = \frac{1-\imath\overline{B}^{(0)}}{1+\imath\overline{B}^{(0)}}\left(1 - \imath\frac{2\Delta\overline{B}}{1+(\overline{B}^{(0)})^2}\right). \tag{B.13}$$

---

[3] In principle, one could use the exact, though unhandy, expression of the input admittance to derive the exact expression of the β_{eff} coefficient for layers of arbitrary thicknesses.

The first factor on the r.h.s. of eq. (B.13) is the coating reflection coefficient in the absence of thermal fluctuations. The factor in brackets accounts for the thermo-refractive effect, which can be described as an equivalent displacement, Δx^{TR}, of the (coated) mirror front-face, by comparing eq. (B.13) with the reflection-coefficient transport equation, viz.

$$\mathcal{R}(\Delta x) = \mathcal{R}(0) \exp\left(\imath \frac{4\pi}{\lambda_0} \Delta x\right). \tag{B.14}$$

Hence, we obtain

$$\Delta x^{TR} = -\frac{\lambda_0}{2\pi} \frac{\Delta \overline{B}}{1 + (\overline{B}^{(0)})^2}, \tag{B.15}$$

from which the generalization of eq. (5.22), given in eq. (5.23), is easily derived.

List of Figures

1.1 A plane circular ring of test particles under the action of a plane monochromatic GW with angular frequency $\omega = 2\pi/T$ 24

1.2 The bare-bones of an interferometric GW antenna. 25

1.3 Main contributions to a typical noise curve of an IFO 30

2.1 PSD corrupted by spectral lines. 35

2.2 Example of weak glitch occurring at LLO. 36

2.3 Example of loud glitch occurring at LLO. 37

2.4 PDF of the glitch noise characterized by (2.10) using $\sigma_G = 1$ and SG glitches, fitted with the model in (2.14). Effect of the glitch rate λ on its shape. . . . 44

2.5 PDF of the glitch noise characterized by (2.10) using $\sigma_G = 1$ and SG glitches, fitted with the model in (2.14). Effect of the maximum glitch SNR, $SNR^{(g)}_{max}$ on its shape. 44

3.1 g_{LO} function obtained through eq. (3.8) for the PDFs in Figure 2.4. Effect of the glitch rate λ on its shape. 50

3.2 g_{LO} function obtained through eq. (3.8) for the PDFs in Figure 2.4. Effect of the maximum glitch SNR, $SNR^{(g)}_{max}$, on its shape. 51

4.1 Empirical distributions of the center frequency and the time duration of events, detected by the Q-pipeline [34] during one week of LIGO S5 data. . . 69

4.2 Sky maps of detection probability at false alarm level of 10^{-2}. Data corrupted by Gaussian noise. Left: Gaussian-noise version of generalized likelihood ratio, GLRT$_G$. Right: Gaussian-noise version of generalized cross-correlation detector, LCC eq. (3.39). Linearly (+)-polarized GWB, $\delta_h = 20$. 70

4.3 Sky maps of detection probability at false alarm level of 10^{-2}. Data corrupted by Gaussian noise. Left: Gaussian-noise version of generalized likelihood ratio, GLRT$_G$. Right: Gaussian-noise version of generalized cross-correlation detector, LCC eq. (3.39). Linearly (×)-polarized GWB, $\delta_h = 20$. 70

4.4 Sky maps of detection probability at false alarm level of 10^{-2}. Data corrupted by non-Gaussian noise, with $\lambda = 0.5s^{-1}$, $SNR^{(g)}_{max} = 100$. Left: Gaussian-noise version of generalized likelihood ratio, GLRT$_G$. Right: Gaussian-noise version of generalized cross-correlation detector, LCC eq. (3.39). Linearly (+)-polarized GWB, $\delta_h = 20$. 71

4.5 Sky maps of detection probability at false alarm level of 10^{-2}. Data corrupted by non-Gaussian noise, with $\lambda = 0.5s^{-1}$, $SNR^{(g)}_{max} = 100$. Left: Gaussian-noise version of generalized likelihood ratio, GLRT$_G$. Right: Gaussian-noise version of generalized cross-correlation detector, LCC eq. (3.39). Linearly (×-polarized GWB, $\delta_h = 20$. 71

4.6 Sky maps of detection probability at false alarm level of 10^{-2}. Data corrupted by non-Gaussian noise, with $\lambda = 0.5s^{-1}$, $SNR^{(g)}_{max} = 100$. Left: generalized likelihood ratio GLRT eq. (3.33). Right: generalized cross-correlation detector, GCC eq. (3.38). Linearly (+)-polarized GWB, $\delta_h = 20$. 72

4.7 Sky maps of detection probability at false alarm level of 10^{-2}. Data corrupted by non-Gaussian noise, with $\lambda = 0.5s^{-1}$, $SNR^{(g)}_{max} = 100$. Left: generalized likelihood ratio GLRT eq. (3.33). Right: generalized cross-correlation detector, GCC eq. (3.38). Linearly (×)-polarized GWB, $\delta_h = 20$. 72

4.8 ROCs of the GLRT eq. (3.33) and GCC, eq. (3.38) in non Gaussian noise with $\lambda = 0.5s^{-1}$, $SNR^{(g)}_{max} = 10^2$ (red markers). ROCs of the Gaussian-noise versions GLRT$_G$, and LCC are also shown for comparison, both in (the same) non-Gaussian noise (black markers) and in Gaussian noise (blue markers). Linearly (+)-polarized GWB with $\delta_h = 20$ emitted by a source at ($\vartheta = 2.28$ rad, $\varphi = 1.99$ rad). 73

4.9 ROCs of the GLRT eq. (3.33) and GCC, eq. (3.38) in non Gaussian noise with $\lambda = 0.5s^{-1}$, $SNR^{(g)}_{max} = 10^2$ (red markers). ROCs of the Gaussian-noise versions GLRT$_G$, and LCC are also shown for comparison, both in (the same) non-Gaussian noise (black markers) and in Gaussian noise (blue markers). Linearly (×)-polarized GWB with $\delta_h = 20$ emitted by a source at ($\vartheta = 2.28$ rad, $\varphi = 0.94$ rad). 74

4.10 Sky maps of coefficients $p^{dd'}$, $d \neq d'$ in GLRT (left) and $\mathcal{R}_{dp}$ in GCC (right) corresponding to cross-correlation terms. First row: LHO-LLO; second row: LHO-Virgo; third row: LLO-Virgo. 77

4.11 ROC of GLRT detector, eq. (3.33), for different values of the glitch rate, at fixed $SNR^{(g)}_{max} = 10^2$ (left), and for different values of $SNR^{(g)}_{max}$ at fixed λ=0.5 s-1 (right). Linearly (+)-polarized GWB with $\delta_h = 20$ emitted by a source at ($\vartheta = 2.28$ rad, $\varphi = 1.99$ rad). 78

4.12 ROC of GCC detector, eq. (3.38), for different values of the glitch rate, at fixed $SNR^{(g)}_{max} = 10^2$ (left), and for different values of $SNR^{(g)}_{max}$ at fixed $\lambda = 0.5s^{-1}$ (right). Linearly (+)-polarized GWB with $\delta_h = 20$ emitted by a source at ($\vartheta = 2.28$ rad, $\varphi = 1.99$ rad). 78

4.13 ROC of GLRT detector, eq. (3.33), for different values of the intrinsic SNR of the GWB, $\delta_h = 20$. Non-Gaussian noise with $\lambda = 0.5s^{-1}$ $SNR^{(g)}_{max} = 10^2$ (left). Linearly (+)-polarized GWB emitted by a source at ($\vartheta = 2.28$ rad, $\varphi = 1.99$ rad). 79

4.14 ROC of GCC detector, eq. (3.38), for different values of the intrinsic SNR of the GWB, $\delta_h = 20$. Non-Gaussian noise with $\lambda = 0.5s^{-1}$ $SNR^{(g)}_{max} = 10^2$ (left). Linearly (+)-polarized GWB emitted by a source at ($\vartheta = 2.28$ rad, $\varphi = 1.99$ rad). 79

4.15 Sky map of detection probability at false alarm level of 10^{-2} of the robust version of GCC detector, GCC$_R$, based on the HL non-linearity. Data corrupted by non-Gaussian noise, with $\lambda = 0.5s^{-1}$, $SNR^{(g)}_{max} = 10^2$. Linearly (+)-polarized GWB, $\delta_h = 20$. 80

4.16 Sky map of detection probability at false alarm level of 10^{-2} of the nonparametric version of GCC detector, GCC$_{NP}$, based on the signum non-linearity. Data corrupted by non-Gaussian noise, with $\lambda = 0.5s^{-1}$, $SNR^{(g)}_{max} = 10^2$. Linearly (+)-polarized GWB, $\delta_h = 20$. 80

4.17 ROCs of GCC detector, eq. (3.38), vs its robust, GCC$_R$, and non-parametric, GCC$_{NP}$, versions. Non Gaussian noise with $\lambda = 0.5s^{-1}$, $SNR^{(g)}_{max} = 10^2$. Linearly (+)-polarized GWB with $\delta_h = 20$ emitted by a source at ($\vartheta = 2.28$ rad, $\varphi = 1.99$ rad). 81

4.18 Power Spectral Density of the noises at the three LIGO IFOs for the analyzed set of data: the two IFOs at Hanford site (H1, H2), and the one at Livingston site (L1). 81

4.19 ROCs in real S5 data (left) and simulated colored Gaussian noise (right). (+)-polarized SG GWB, $\delta_h = 20$, emitted from a source at ($\vartheta = 2.28$ rad, $\varphi = 1.99$ rad). 82

4.20 ROCs in real S5 data (left) and simulated colored Gaussian noise (right). (+)-polarized SG GWB, $\delta_h = 30$, emitted from a source at ($\vartheta = 2.28$ rad, $\varphi = 1.99$ rad). 82

4.21 ROCs in real S5 data. Weak ($SNR^{(g)}_{max} = 30$) glitches added: $\lambda = 0.2s^{-1}$ (left) and $\lambda = 1s^{-1}$ (right). Linearly (+)-polarized SG GWB, $\delta_h = 30$, emitted from a source at ($\vartheta = 2.28$ rad, $\varphi = 1.99$ rad). 82

4.22 ROCs in real S5 data. Loud ($SNR^{(g)}_{max} = 300$) glitches added: $\lambda = 0.2s^{-1}$ (left) and $\lambda = 1s^{-1}$ (right). Linearly (+)-polarized SG GWB, $\delta_h = 30$, emitted from a source at ($\vartheta = 2.28$ rad, $\varphi = 1.99$ rad). 83

4.23 ROCs of the unmodified (no subscript) vs modified (subscript HL) RIDGE statistics in LIGO S5 data. Linearly (+)-polarized SG GWB, $\delta_h = 30$, emitted from a source at (ϑ=2.28 rad, $\varphi = 1.99$ rad). 83

4.24 ROCs of the RIDGE statistics in real S5 data. Weak glitches added. Linearly (+)-polarized SG GWB, $\delta_h = 30$, emitted from a source at (ϑ=2.28 rad, φ=1.99 rad). 84

4.25 RIDGE statistics vs GCC in real S5 data. No Glitches and weak glitches ($SNR^{(g)}_{max} = 30$, $\lambda = 1s^{-1}$). Linearly (+)-polarized SG GWB, $\delta_h = 30$, emitted from a source at (ϑ=2.28 rad, φ=1.99 rad). 84

5.1 Projected noise floor of Advanced LIGO [97]. Brownian noise is limiting in the most sensitive frequency band. 86

6.1 Simplified optical scheme of a Michelson-Morley interferometer for GW detection. 96

6.2 General multilayer dielectric slab structure. 98

6.3 Power reflectivity spectrum for the QWL design satisfying ETM requirement in single-wavelength operation. 101

6.4 The structure of the reference quarter-wavelength TNI coating. 102

6.5 Coating loss angle reduction factor as a function of the number of doublets N_D. The corresponding values of the ration z_H/z_L are shown at the top of the plot. The QWL and the optimized coatings are indicated. 102

6.6 Structure of the optimized TNI coating. 103

6.7 Measured spectral density of the cavity length noise for the QWL design along with the shot noise (dashed line) and Brownian noise (solid line). The two vertical lines identify the analysis region, where the fit was done to extract the loss angle. 104
6.8 Plot of the measured spectra in the analysis region after the Savitzky-Golay smoothing filter was applied. 104
6.9 Square root of coating noise PSD versus the number of doublets. Left: Brownian noise only. Right: Brownian and thermo-optic noise. 105
6.10 Schematic representation of the ETM reference dichroic design. The ITM reference design consists only of the bottom stack. Parameters of both designs are in Table 6.3. 105
6.11 Power reflectivity spectrum of ETM reference dichroic design. A close-up around the second operation wavelength is shown in the inset. 106
6.12 Power reflectivity spectrum of ITM reference dichroic design. A close-up around the second operation wavelength is shown in the inset. 107
6.13 Iso-reflectance (0.95 @532nm) and iso-transmittance (5.5 ppm @1064nm) curves in (ξ_L, ξ_H)-plane for 19 doublets, corresponding to the preferred values. The two intersections are acceptable operating points. 108
6.14 Level map of ϕ_{coat} for the dichroic design in the (ξ_L, ξ_H)-plane for 19 doublets. Dark colour implies low value of ϕ_{coat}. 109
6.15 Iso-reflectance (0.95 at 532 nm) and iso-transmittance (5.5 ppm at 1064 nm) curves in $(\xi_L^{first}, \xi_H^{last})$-plane of the dichroic design for 19 doublets. 110
6.16 Amplitude of the total electric field on top of the ETM coating as function of ξ_L^{first}. ξ_H^{last} is accordingly identified by the equation of the tangent line at the intersection point of the two curves in Figure 6.15. 111
6.17 Power reflectivity spectrum of dichroic ETM optimized design. A close-up around the second operation wavelength is shown in the inset. 111
6.18 Iso-reflectance (0.99 at 532 nm) and iso-transmittance (14000 ppm at 1064 nm) curves in (ξ_L, ξ_H)-plane of the dichroic design for 9 doublets. 113
6.19 Iso-reflectance (0.99 at 532 nm) and iso-transmittance (14000 ppm at 1064 nm) curves in $(\xi_L^{first}, \xi_H^{last})$-plane of the dichroic design for 9 doublets. 114
6.20 Amplitude of the total electric field on top of the ITM coating as function of ξ_L^{first}. ξ_H^{last} is accordingly identified by the equation of the tangent line at the intersection point of the two curves in Figure 6.19. 114
6.21 Power reflectivity spectrum of dichroic ITM optimized design. A close-up around the second operation wavelength is shown in the inset. 115

List of Tables

6.1 AdLIGO Requirements on test masses optical properties. Source: AdLIGO wiki. 97

6.2 Refraction index, loss angle and Young modulus of candidate materials for coatings. 97

6.3 Parameters of ETM and ITM reference dichroic designs. 106

6.4 Minimal Brownian noise points in (ξ_L, ξ_H)-plane for different number of doublets for the ETM design. 108

6.5 Parameters of final dichroic optimized design for the ETM coating. 109

6.6 Reflectivities of ETM optimized dichroic design at the two operation wavelengths and other potentially useful wavelengths. 110

6.7 Minimal Brownian noise points in (ξ_L, ξ_H)-plane for different number of doublets for the ITM design. 112

6.8 Parameters of final dichroic optimized design for the ITM coating. 112

6.9 Reflectivities of ITM optimized dichroic design at the two operation wavelengths and other potentially useful wavelengths. 112